Fall 2013

# Design, development and characterization of a novel neutron and X-ray combined computed tomography system

Vaibhav Sinha



Department: Mining and Nuclear Engineering

# DESIGN, DEVELOPMENT AND CHARACTERIZATION OF A NOVEL NEUTRON AND X-RAY COMBINED COMPUTED TOMOGRAPHY SYSTEM

by

VAIBHAV SINHA

A DISSERTATION

Presented to the Faculty of the Graduate School of the

MISSOURI UNIVERSITY OF SCIENCE AND TECHNOLOGY

In Partial Fulfillment of the Requirements for the Degree

DOCTOR OF PHILOSOPHY

in

NUCLEAR ENGINEERING

2013

Approved
Hyoung Koo-Lee, Advisor (Chairman)
Xin Liu
Carlos H. Castano
Ayodeji Alajo
Muthanna Al-Dahhan

## ABSTRACT

Visualizing the three dimensional structure of objects (e.g. nuclear fuel, nuclear materials, explosives and bio materials) and phenomena (e.g. particle tracking) can be very important in nondestructive testing applications. Computed tomography systems are indispensable tools for these types of applications because they provide a versatile non-destructive technique for analysis. A novel neutron and X-ray combined computed tomography (NXCT) system has been designed and developed at the Missouri University of Science & Technology. The neutron and X-ray combined computed tomography system holds much promise for non-destructive material detection and analysis where multiple materials having similar atomic number and differing thermal cross section or vice versa may be present within an object, exclusive neutron or X-ray analysis may exhibit shortcomings in distinguishing interfaces. However, fusing neutron image and X-ray image offers the strengths of both and may provide a superior method of analysis. In addition, a feasible design of a sample positioning system which allows the user to remotely and automatically manipulate the objects makes the NXCT system viable for commercial applications. Moreover, characterization of the newly developed digital imaging system is imperative to the performance evaluation, as well as for describing the associated parameters. The performance of a combined neutron/X-ray digital imaging system was evaluated in terms of modulation transfer function (MTF), noise power spectrum (NPS) and detective quantum efficiency (DQE). This dissertation is a complete overview of the design of the NXCT system, operation, algorithms, performance evaluation and results.

## ACKNOWLEDGMENTS

I am greatly thankful to my PhD advisor Dr. Lee who provided his wisdom and knowledge to train and guide me to become a succesful professional in the field of nuclear engineering and radiation imaging. I highly appreciate Dr. Lee's guidance and kindness while I was working on the design and development of the unique combined neutron/X-ray imaging facility at Missouri S&T. I am thankful to Dr. Lee and Dr. Kumar for financial assistance during the PhD research at Missouri S&T. I am highly thankful to Dr. Castano and Dr. Liu to help me on different matters on several occasions. I also would like to express sincere thanks to Dr. Al-Dahhan to support my ideas and Dr. Alajo for sharing his valuable academics and research experiences. I am grateful to Dr. Mueller for providing his generous support to acquire calibration phantoms and collimator components to ensure proper operation of the NXCT system. I am thankful to my advisor and Dr. Usman for providing me an opportunity to come to the Missouri University of Science & Technology. I am thankful to MSTR staff; Bill Bonzer, Craig Reisner and Raymond Kendrick for assistance with the experiments at MSTR. I am thankful to Jeffery Divis, Michael Crabtree, Michael Acton, Edwin Grant, Aashish Avachat, Chris Swisher, Joshua Fagnant and Steven Anderson. I greatly appreciate the help of Mr. Brian White, Ms. Rhonda Colon and Dr. Achim Czasch, and Mr. Mark Jewell for optimization of the NXCT components. I cannot thank my wife Anjali enough for supporting me fully on every little step. I am highly thankful for her moral support and encouragement to pursue my research and academics with high motivation. I am thankful to my father Late Dr. Navin Kumar Sinha for his spiritual support and mother Mrs. Anita Sinha and family members for their support and endurance while I was working on my PhD.

# TABLE OF CONTENTS

**Page**

# LIST OF ILLUSTRATIONS

**Figure** **Page**

# LIST OF TABLES

**Table** **Page**

# NOMENCLATURE

| Symbol | Description |
|---|---|
| NXCT | Neutron and X-ray Combined Computed Tomography |
| MSTR | Missouri University of Science & Technology Nuclear Reactor |
| Ee | Energy of Electron |
| h | Planck's Constant |
| ν | Frequency |
| p | Momentum |
| c | Speed of Light |
| mo | Initial Mass |
| kV | Kilo Volt |
| mA | Milli Ampere |
| s | Second |
| Gd | Gadolinium |
| Dy | Dysprosium |
| L/D | Length to Diameter Ratio |
| CFD | Constant Fraction Discriminator |
| TDC | Time to Digital Converter |
| FAMP | Frequency Amplifier |
| CCD | Charged Couple Device |
| I | Final Intensity |
| $I_0$ | Initial Intensity |
| μ/ρ | Linear Attenuation Coefficient |
| ρ | Density |
| t | Thickness or Length of the Medium |
| n | Number Density |
| σ | Microscopic Cross-Section |
| Σ | Macroscopic Cross-Section |
| lp/mm | Line Pairs per Millimeter |

| | |
|---|---|
| MCP | Micro Channel Plate |
| MCNP | Monte Carlo N-Particle Code |
| ASTM | American Society for Testing and Materials |
| IQI | Image Quality Indicator |
| MTF | Modulation Transfer Function |
| NPS | Noise Power Spectrum |
| DQE | Detective Quantum Efficiency |

# 1. INTRODUCTION

## 1.1. BACKGROUND

Radiation imaging has been the most successful non-invasive method to obtain structural and compositional information of an object [1-8]. In the year 1895, the discovery of X-rays by German physicist Wilhelm Roentgen provided an extremely valuable tool to the benefit of mankind. The widespread use of X-rays can be found in medical, industry and research. The discovery of neutrons by Sir James Chadwick in 1932 and demonstration of neutron radiography in later years of 1930's led to the development of neutron imaging technique which is complementary to X-rays. Furthermore, invention of the computed tomography by Sir Godfrey Hounsfield provided new horizon to the field of imaging. Since then, many useful applications of computed tomography can be found. Recent techniques also involve combining two different - imaging modalities and providing fusion data for detailed information.

**1.1.1. Theory of Radiation Imaging.** The concept of radiation imaging can simply be explained by the radiation attenuation law also known as Beer Lambert's law. In a radiation imaging system, a beam originating from the radiation source impinges on an object and leaves partially or fully attenuated to the imaging detector which then recorded by the detector to form an image. The attenuation of beam can be further explained by interaction of the radiation with the matter. In below lines a more detailed description is provided.

**1.1.2. Interaction of Neutron with Matter.** The physical universe can be quantified into two components energy and matter. Most of the physical processes including radiation imaging involve interaction and exchange between the matter and energy.

Neutrons are neutral particles and interact only with the nucleus of an atom; this allows neutrons to have greater penetration capabilities than X-rays. There are mainly three types of radiation sources such as the neutron generator, nuclear reactor and neutron emitting radionuclides (e.g. Cf-252) to obtain a neutron beam for neutron imaging. In the neutron imaging experiments, majority of the neutron beam (80-90%) pass through from an imaging object without any interaction [9]. The interaction of the neutron and X-ray beam with an imaging object depends on the cross-sectional properties of the object materials. Depending upon the cross-sectional properties of object materials neutrons can be absorbed, scattered or both during interaction with the materials [10].Furthermore, light atomic number materials have higher cross-section for neutrons results in high contrast images. Oppositely, high atomic number material have higher cross-section for X-ray results in high contrast images (see Fig. 1.1). The neutron macroscopic cross-section ($\boldsymbol{\Sigma}$) for thermal and cold energies follows 1/v rule where v is the neutron velocity. Neutrons interact with material depending on the cross-sectional properties of the material and the characteristic neutron flux spectrum. The neutron interactions with materials can be absorbtion, scattering or both. This complementary nature of neutron and X-ray interaction with materials make them a comprehensive probing tool for nondestructive testing research and extracting complete information from the imaging object.

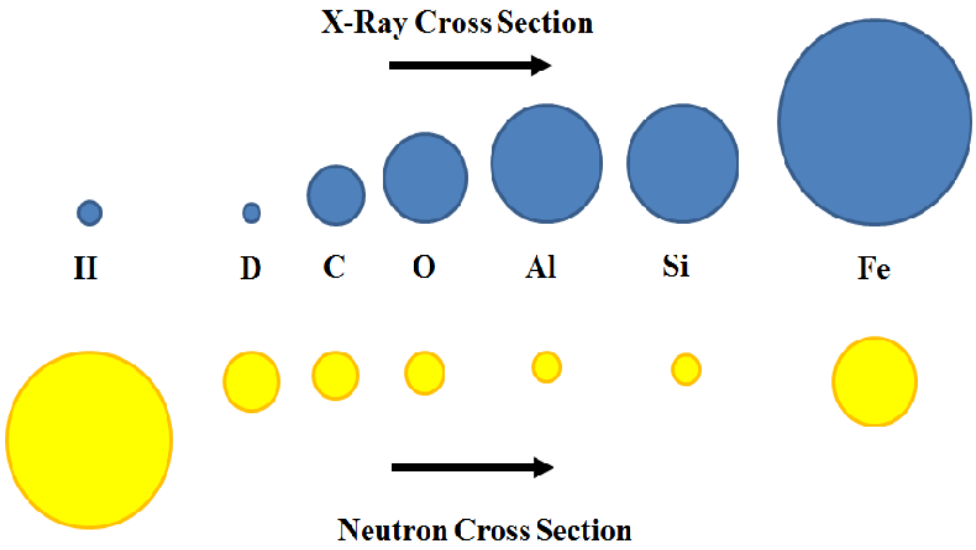


Figure 1.1. Comparison of X-ray and Neutron Cross-section with Materials

Neutrons, unlike X-rays, do not interact with the electrostatic charge of the electrons (see Fig.1.2) [4]. Instead, neutrons interact with the atomic nucleus, (see Fig.1.2) and therefore neutrons have the ability to differentiate isotopes of the same element. Neutrons are neutral sub-atomic particles; having no charge allows them to sustain interactions with electrons. Neutrons interact only with the nuclei in the path, a small fraction of the total volume of an atom. This allows neutrons to have greater penetration ability. X-rays on the other hand, are charged particles or electromagnetic radiation. X-rays interact with electrons and these interactions with electrons causes X-rays to have less penetration capacity. In short, the characteristics of neutron and X-ray interactions with materials are quite different and allow them to extract complimentary structural and compositional information from the object of interest.

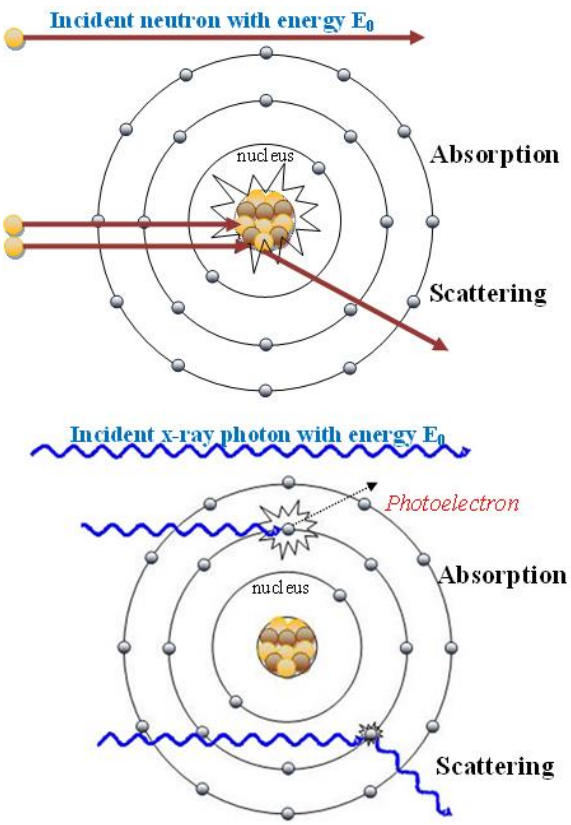


Figure 1.2. Interaction of (a) Neutron and (b) X-ray with an Atom

**1.1.3. Interaction of Photons with Matter.** The interaction of photons with matter can be explained by below headings.

**1.1.3.1. Photoelectric absorption.** In photoelectric effect, photons interact with a material and get completely absorbed in the matter, and liberate an orbital electron (see Fig.1.3). In other words, the photoelectric effect takes place between a photon and a bound atomic electron. The emitted orbital electron (the photoelectron) is ejected with a kinetic energy equivalent to the initial x-ray ray energy minus the binding energy of the electron. The kinetic energy of the electron can be described by:

$$E_e = h\nu - BE \quad (1)$$

Where, $h\nu$ = photon energy

$h$ = 6.626 x $10^{-34}$ J.s (Planck's Constant)

$\nu$ = Frequency of X-ray

$BE$ = binding energy

Photoelectric absorption is the dominant process for X-ray energies of 50keV. It is also dominant for atoms of high atomic numbers. It is shown (see Fig.1.4) that when the total electron kinetic energy is equal to the incident X-ray energy, the differential distribution of electron kinetic energy for a series of photoelectric absorption events will be a simple delta function. [11, 12]

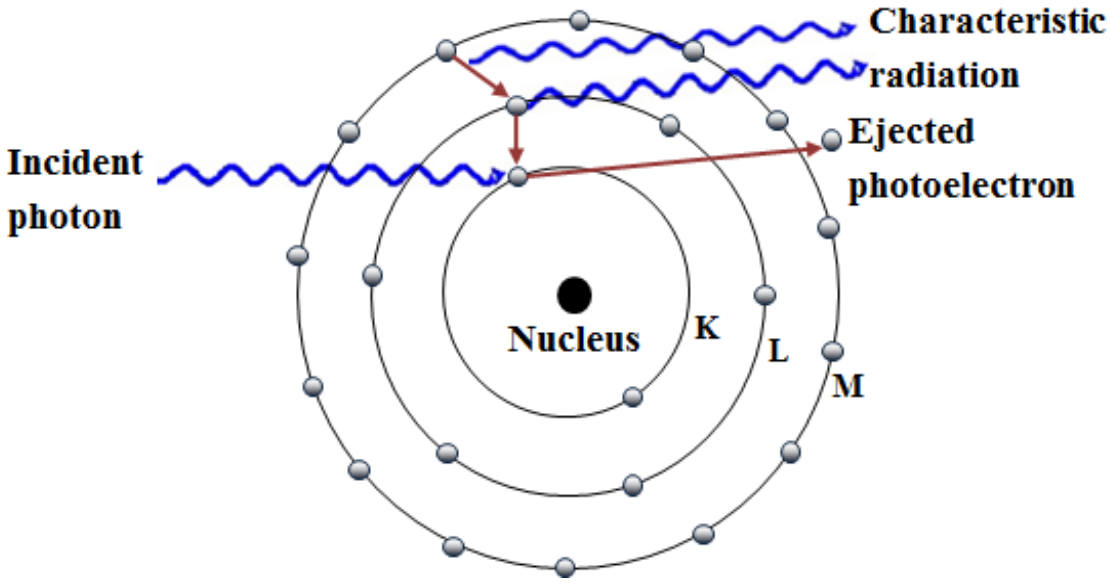


Figure 1.3. Schematic of Photoelectric Absorption

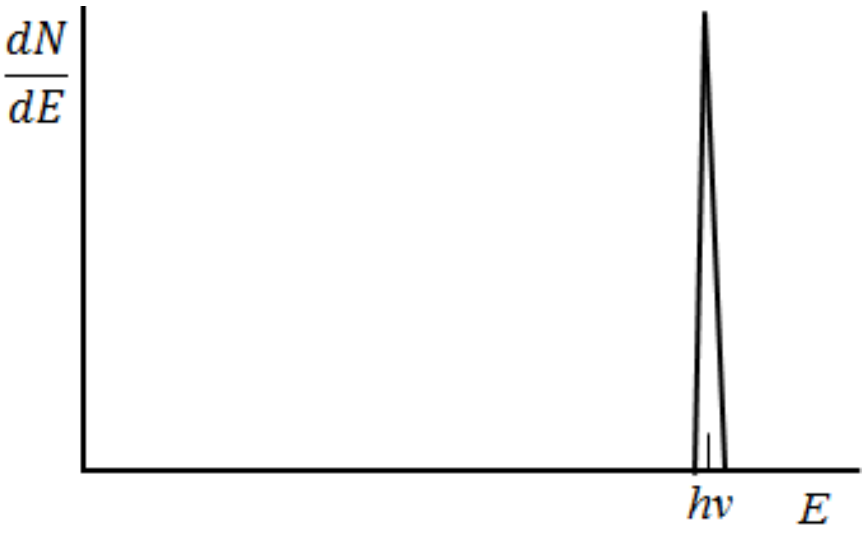


Figure 1.4. Single Peak at a Total Electron Energy Corresponding to the Energy of the Incident X-rays

**1.1.3.2. Compton scattering.** In Compton Sacttering a high-energy photon interacts with a target, which has loosely bound electrons on its outer shell. After the interaction, the photon changes direction and its energy is reduced to an amount that is given off to the electron (see Fig. 1.5, 1.6). Compton scattering occurs between the energy ranges of 100keV to 10MeV. In this process, X-rays rays impinge on the detector, but impart some of its energy to an electron(s). The remaining energy is then converted into a new, lower energy, scattered X-ray. If the incident X-ray has a frequency, ν and is scattered through an angle θ, the kinetic energy of the electron is given by [5]:

$$Ee = h\nu - h\nu' \quad (2)$$

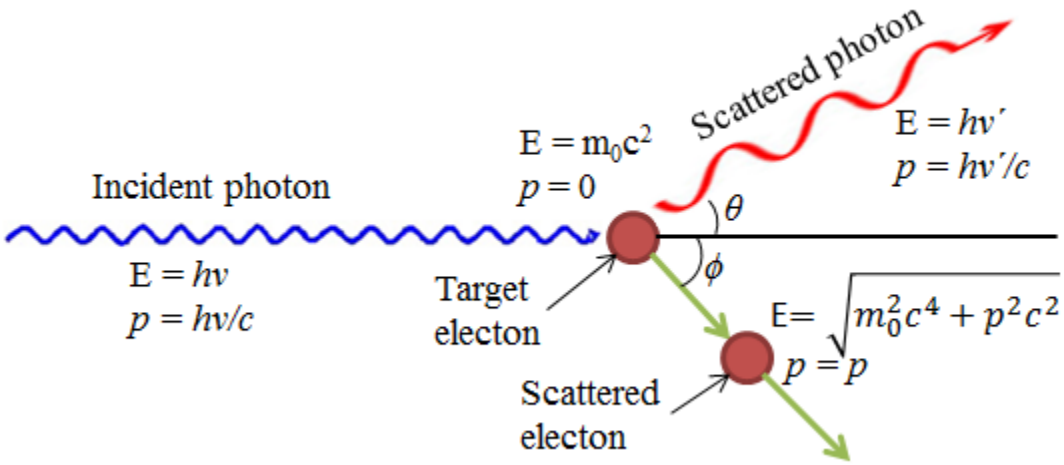


Figure 1.5. Schematic of Compton Scattering

By the principle of conservation of momentum, the energy of the scattered photon as a function of scattering angle, $\theta$ is given by:

$$h\nu' = \frac{h\nu}{1+(1-\cos\theta)\frac{h\nu}{c^2 m_0}} \tag{3}$$

Where $m_0$ is the rest mass of an electron. Thus the kinetic energy transferred to the electron is:

$$Ee = h\nu - h\nu' = h\nu\frac{(1-\cos\theta)\frac{h\nu}{c^2 m_0}}{1+(1-\cos\theta)\frac{h\nu}{c^2 m_0}} \tag{4}$$

Between the energy range of 0.5 MeV and 2.5MeV; Compton scattering is the dominant Process, whereby photons transfer their energy to matter. The physical form of the medium through which is the X-rays are passing is not very important. It is the electron density, which is related to the bulk density of the medium, which is the important factor. In normal circumstances, all scattering angles will occur in the detector.

Therefore, a continuum of energies can be transferred to the electron, ranging from zero up to the maximum value, i.e. when θ = π. (see Fig. 1.6) [11]

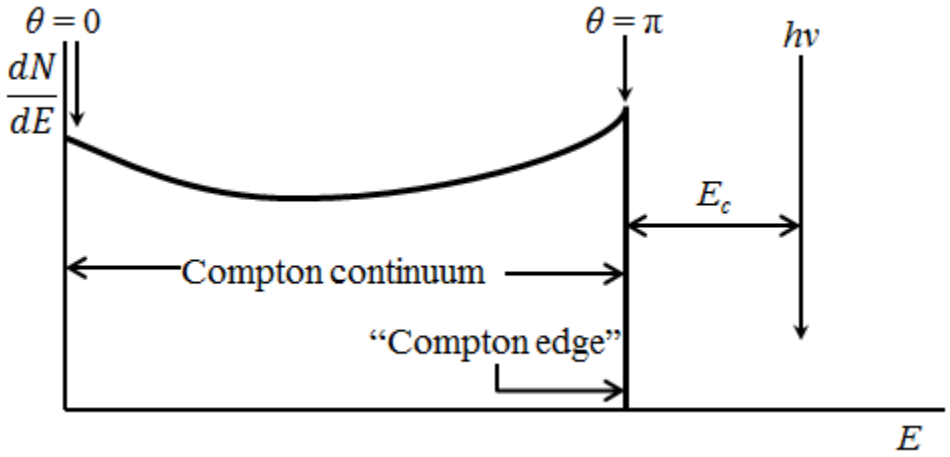


Figure 1.6. The Electron Energy Distribution for Compton Continuum

**1.1.3.3. Pair production.** Pair production takes place with high-energy X-rays where energies greater than 1.02MeV. In this process, the X-ray photon spontaneously transforms into an electron and positron (see Fig. 1.7, 1.8) when it is in the vicinity of the Coulomb force of the nucleus. The excess energy of the rest mass of the electron and positron is transferred into the kinetic energy of the two particles and the recoil of the local nucleus. Typically, both the electron and positron travel very short distances before losing their kinetic energy to the absorbing medium. Thus a spike occurs at an energy corresponding to the initial energy of the X-ray minus the rest mass of the two particles:

$$E_{pair} = h\nu - 2m_0c^2 \quad (5)$$

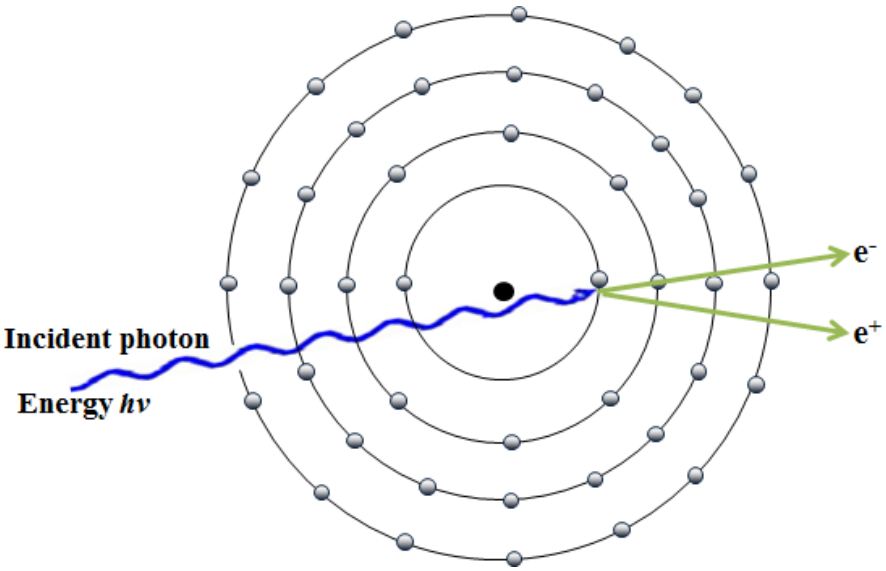


Figure 1.7. Schematic of Pair Production

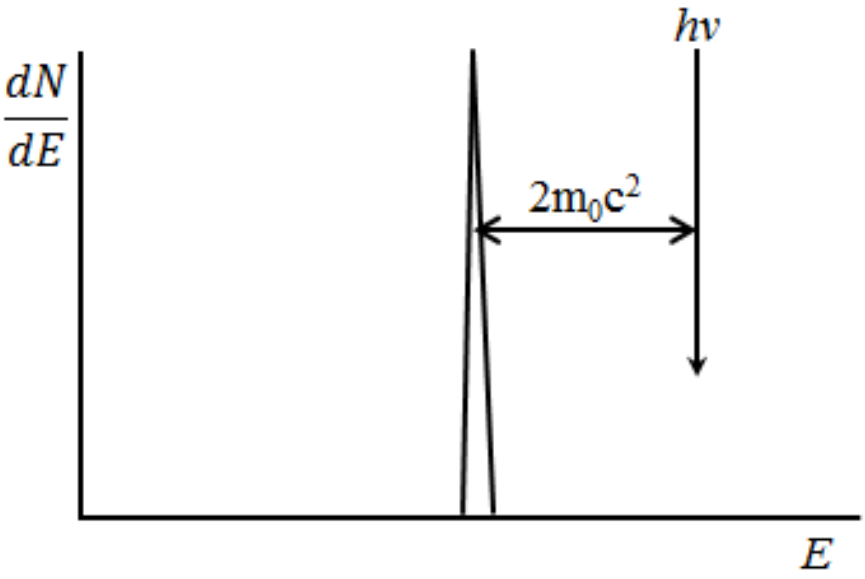


Figure 1.8. Plot of Charged Particle KE by the Incident X-ray Energy

## 1.2. OVERVIEW OF COMMONLY EMPLOYED RADIATION SOURCES

**1.2.1. X-ray Source.** X-rays are generated in high voltage electron tube by utilizing energies from free electrons and converting them into photons. To provide constant high voltage and precise controlled currents to the X-ray tube different types of X-ray generators can be employed. The complete description of different X-ray generators and their operating principle can be found elsewhere [5]. To generate X-rays (see Fig. 1.9), a high voltage power source is connected across cathode and anode to accelerate the electrons [see Appendix A4]. Electrons from the cathode collide with the anode material or target (e.g. tungsten, molybdenum and copper) and generate X-ray photons from Bremsstrahlung interaction. The X-ray generation efficiency is only 1% in this case and rest of the energy is released as a heat.

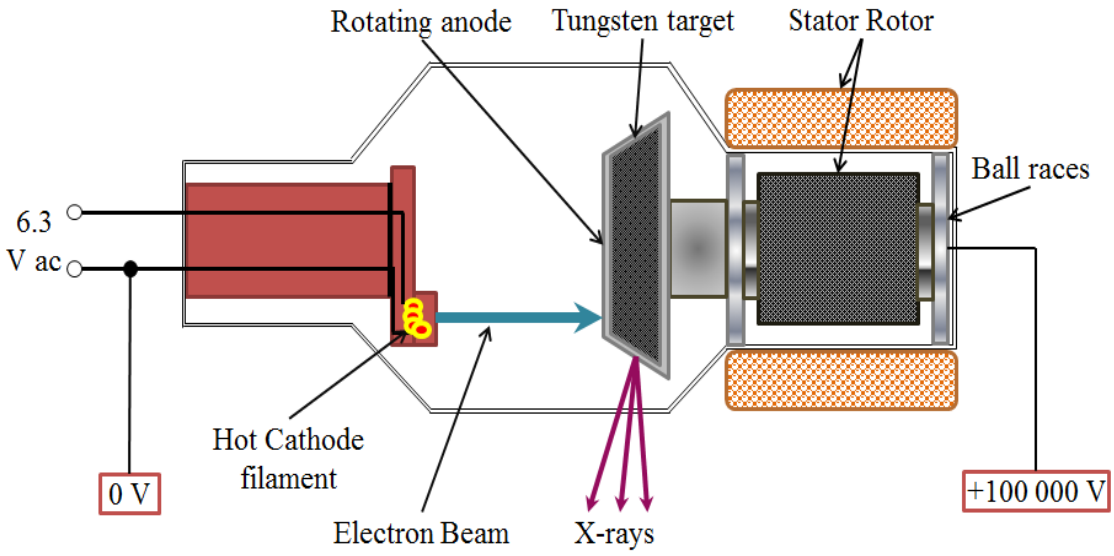


Figure 1.9. Description of X-ray Generation

It is important to mention that different target material results in distinct spectrums. The X-ray energy spectrum and exposure can be controlled by using three quantities; energy (kV), tube current (mA) and time (s). The X-ray tube comes in different configurations depending on the application. The Coolidge tube (improvised version of crooks tube), rotating anode tube and microfocus X-ray tube (solid anode and metal-jet anode) are commonly used tubes in today's radiography applications. [5]. The main design of an X-ray tube depends on three factors: high X-ray beam output (for short exposure, motion blurring and cine), focal spot (penumbra blurring and spatial resolution) and heat generation (to avoid melting or thermal deformation) [5].

**1.2.2. Neutron Sources.** The neutron sources can be classified in three main categories given below:

- Large devices: Nuclear fission reactors, spallation at particle accelerators and nuclear fusion systems comes in this category.
- Small Devices: Radioisotopes such as californium-252 undergoing spontaneous fission with emission of neutrons can be used but such source will continuously emit the neutron and will be limited by its half-life. Furthermore, neutron can be produced by bombarding alpha particles on low atomic weight isotopes of lithium, beryllium, carbon and oxygen. Photoneutron sources and sealed neutron generator can also be included in small devices category.

- Moderately Sized Devices: Plasma focus neutron source, light ion accelerators with hydrogen, deuterium and tritium ion sources and high energy photoneutron system comes under this category.
- Depending upon the sources and their operation, the neutron spectrum can be evaluated and can be optimized for the desired neutron imaging applications. It is also important to note that higher neutron flux and precisely collimated neutron beam will result in high contrast images with less image acquisition time.

## 1.3. CLASSIFICATION OF COMMONLY USED IMAGING DETECTORS

The classification of the imaging detectors can be simplified by the mechanism of image formation in below lines:

- Imaging Plate: The electronic excitation in crystal can be used to form the image.
- Scintillator plus Semiconductor: Using the light excitation and then recording of electrical signal by detector array can be used to generate an image.
- Semiconductor Detector: Photons gets converted to electron-hole pairs to detect the X-rays and help to form the image.
- Scintillator: The light excitation produced in scintillator can be used to record an image with a readout circuit. Depending upon X-ray or neutron imaging application a scintillator can be chosen.
- Image Intensifier: By increasing the light intensity using micro channel plates and then image can be captured using a low cost camera or another readout method.

- Charged Couple devices (CCD): The CCD devices uses electron charges to produce an image. For neutron imaging, a scintillator or boron doped micro-channel plate with mirror and optical camera readout system can be used.
- Film: Standard radiographic film is a plastic sheet coated with a layer of emulsion. This emulsion is made of Silver Iodobromide [5]. The X-ray photon strikes with emulsion and deposits energy into it. In short, excitation and blackening of the film help to produce image. For neutron imaging, converter foils made of Gd, Dy or high neutron absorbing material can be used with the film.

# 2. RADIATION IMAGING PHYSICS AND BEAM DIAGNOSTICS

## 2.1. PHYSICS OF X-RAY IMAGING

The X-ray attenuation depends on the material properties of an imaging object. The Beer-Lambert's Law characterizes the intensity of un-collided photons after passing through a medium [13]. The Beer-Lambert's Law can be mathematically defined as:

$$I = I_0 \exp\left[-\left(\frac{\mu}{\rho}\right)\rho t\right] \tag{6}$$

According to Beer-Lambert's Law, the final intensity ($I$) at the imaging detector can be related to the initial intensity ($I_0$) of the X-rays with attenuation coefficient ($\mu/\rho$), density ($\rho$), and the thickness or length of the medium ($t$).

For multiple attenuating materials the Beer-Lambert Law can be expanded to include attenuations from the multiple materials. The expanded form is as below:

$$I = \int_0^{Emax} I_0(E) \exp\left[-\sum_{j=1}^{n}\left(\frac{\mu(E)}{\rho}\right)_j \rho_j t_j\right] dE \tag{7}$$

Where, there are $n$ number of attenuating materials in the path of photons, and attenuation is integrated over the X-ray energy spectrum [13, 14].

## 2.2. PHYSICS OF NEUTRON IMAGING

Neutrons are electrically neutron particles and interact with the nuclei of atom. The neutron macroscopic cross-section ($\Sigma$) for thermal and cold energies follows 1/v rule where v is the neutron velocity. Neutrons interact with material depending on the cross-sectional properties of the material and the characteristic neutron flux spectrum. The neutron interactions with materials can be absorbtion, scattering or both. The material

properties which are responsible for the interactions are absorption cross-section, number density, and the thickness of the material. [13-15]

The interactions of neutrons or neutron imaging physics can be mathematically defined by following equation: [9]

$$\mathrm{I(t)} = \mathrm{I_0}\,\exp(-\mathrm{n}\,\sigma\,\mathrm{t}) \tag{8}$$

Equation (4) shows the relationship of the final intensity $I(t)$ to initial intensity$\mathrm{I_0}$, with the material properties; number density ($n$), microscopic cross-section ($\sigma$), and the thickness ($t$). The product ($n\sigma$) is called the macroscopic cross-section($\Sigma$). In an imaging object multiple attenuating mediums (elements or isotopes) can be present then total cross-section can calculated in the form of the following equation (13):

$$\mathrm{I(t)} = \mathrm{I_0}\,\exp(-\Sigma_{\mathrm{total}}\,\mathrm{t}) \tag{9}$$

Where, $\Sigma_{\mathrm{total}}$ is the total macroscopic cross-section given by:

$$\Sigma_{\mathrm{total}} = \sum_{\mathrm{j}} \mathrm{n_j}\sigma_{\mathrm{j}} = \sum_{\mathrm{j}} \Sigma_{\mathrm{j}} \tag{10}$$

## 2.3. CHARACTERIZATION OF NEUTRON AND X-RAY BEAM

To characterize the neutron and X-ray beam, simulations, analytical calculations and experimental methods were used [16-19]. A commercially available X-ray source with performance tested focal spots was used in this research and a SpeckCalc program was used to simulate the X-ray flux spectrum. To verify the X-ray beam diagnostic trends, a fine machined phantom was imaged at different beam currents (see Fig. 2.1).

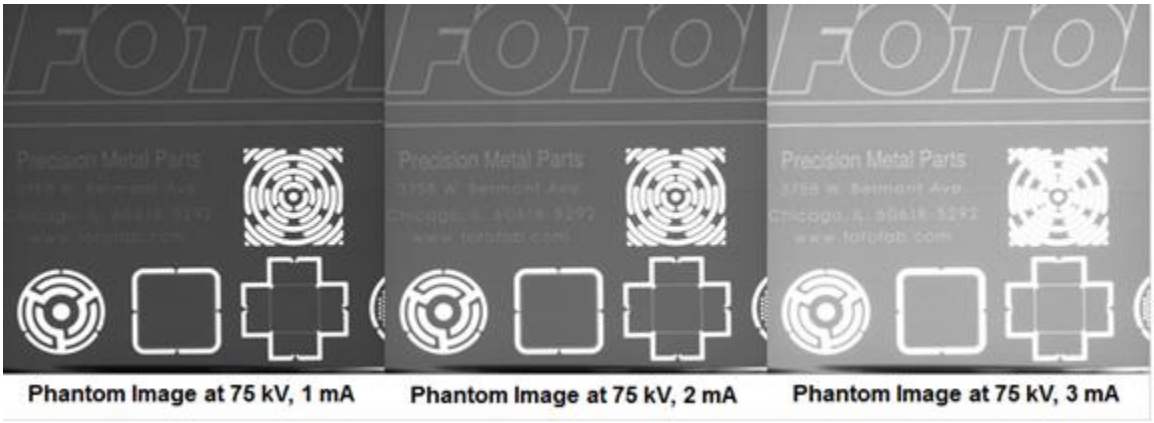


Figure 2.1. Phantom Image at Different X-ray Beam Currents

For neutron beam diagnostics, MCNP simulations, analytical calculations and experiments were used to characterize the neutron beam. The neutron flux mapping experiments were performed to quantify the flux at the beam port and near the neutron imaging detector. The average neutron flux at the beam port (see Fig. 2.2, 2.3) and at the detector (see Fig. 2.4, 2.5) found to be 1.08E8 and 4.0E7 neutrons per centimeter square per second, respectively. The L/D ratio for neutron imaging module was calculated based on existing configuration of neutron beam path, aperture diameter and distance of the neutron image sensor from the aperture. The L/D ratio found to be 45.39 and with the modified collimator aperture the ratio becomes 148. The value of L/D ratio $\geq$10 is acceptable for useful resolution neutron imaging [20] and higher L/D ratio will contribute to a sharper image. The next criterion [21], factor of merit described by Kobayashi, also requires a higher value of L/D for a sharper image. In this research, both criterions were considered and used to optimize the neutron beam diagnostics as well as the imaging geometry.

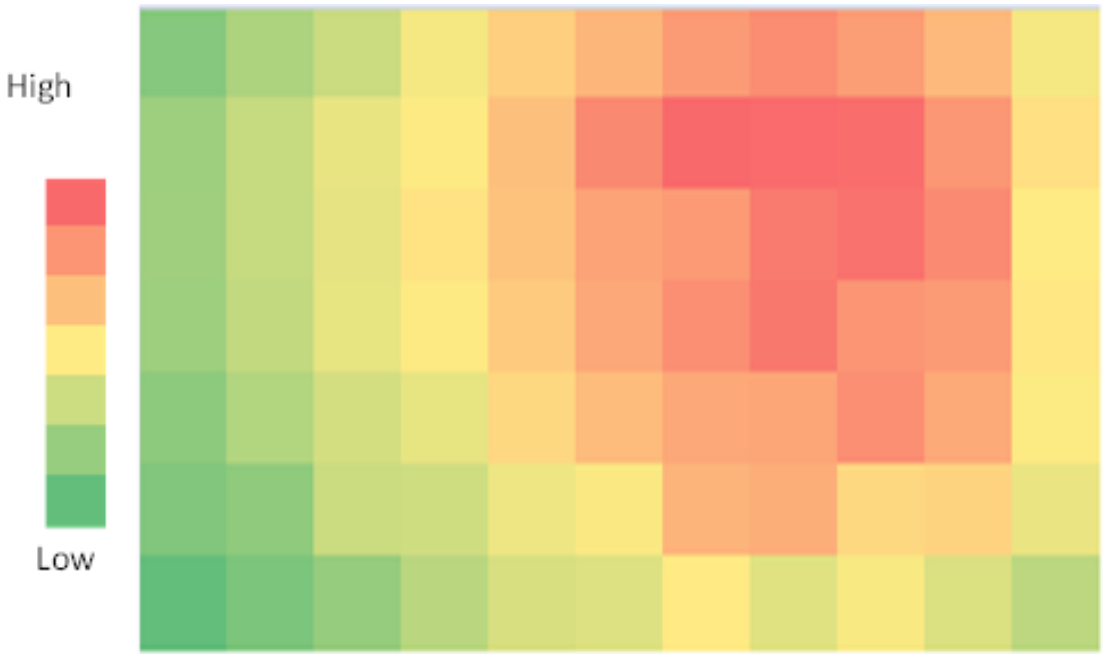


Figure 2.2. Neutron Flux Intensity at Beam port

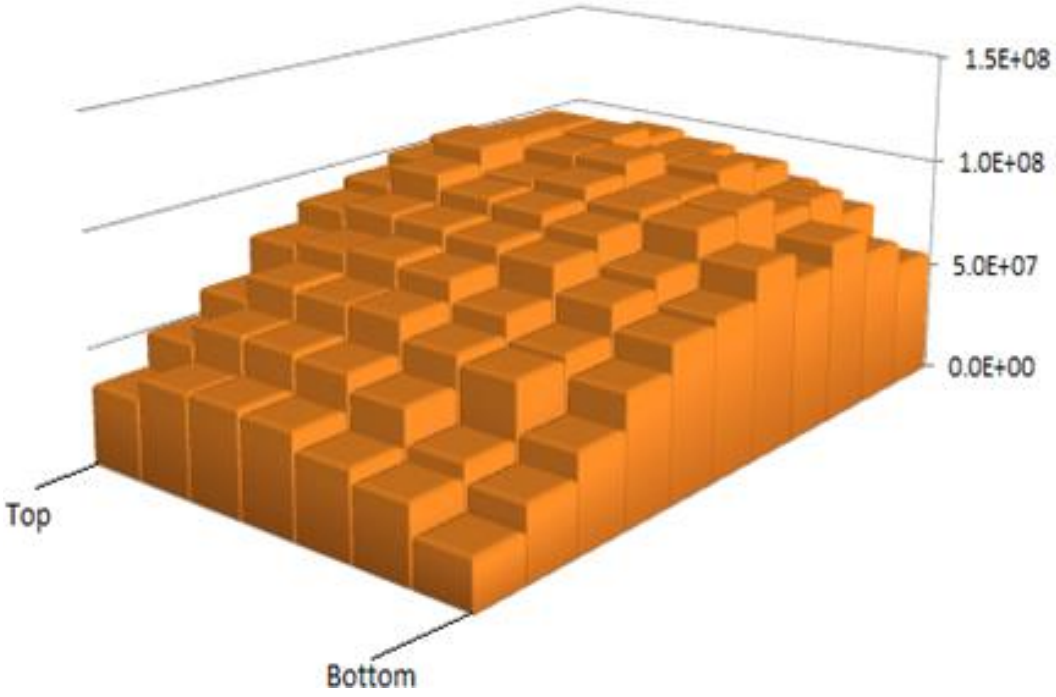


Figure 2.3. Neutron Flux Profile at Beam Port


Figure 2.4. Neutron Flux Intensity at the Neutron Image Detector

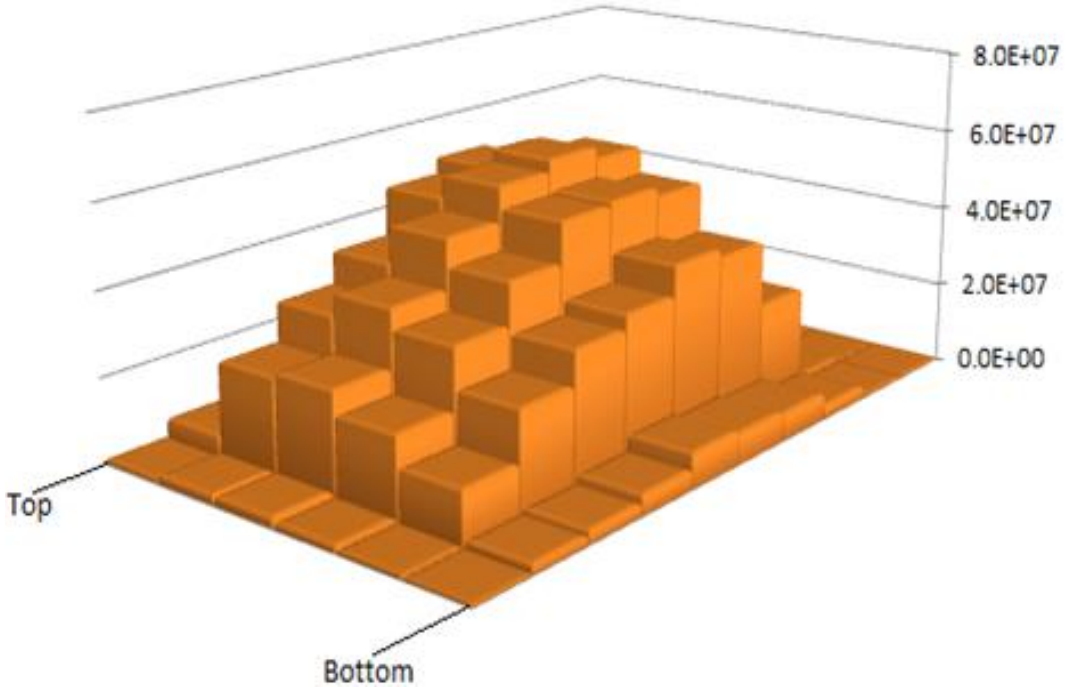


Figure 2.5. Neutron Flux Profile at the Neutron Image Detector

Furthermore, the Cadmium ratio of the neutron beam was also calculated. The MSTR neutron beam with existing collimator arrangement produces a Cadmium ratio of 9.82 which is the indication of an acceptable quality of thermal neutron beam for neutron imaging applications. However, to increase the Cadmium ratio at the beam port a simple pin-hole collimator made of borated polyethylene with beam filters was designed and fabricated. The micro-channel plate (MCP) based neutron detector utilizes a thermal neutron beam for an image formation and fast neutrons are considered to be degrading the image quality. The thickness of a sapphire crystal was optimized to decrease the fast neutron content in thermal neutron beam using the published literature [22-24]. Applying Stamatelatos et al. [23] approach to optimize the thickness of the sapphire crystal, a 6 inch thick sapphire crystal is adequate to maximize slow neutron transmission with minimizing the fast neutron content in a thermal neutron beam without affecting the thermal neutron flux content. A hemex grade single crystal sapphire was fabricated with a thickness of 6 inch and c-axis of this crystal was kept parallel to the incident neutron beam. To increase the L/D ratio and reduce the scatter neutron content, the existing aperture diameter was reduced from 1.75 x 2.75 square inch to Φ1 inch. A borated polyethylene block 1.70 x 2.70 x 8 cubic inch with a centrally drilled hole of 1 inch diameter was fabricated (see Fig. 2.6). This borated polyethylene collimator was fabricated in such a manner that it can hold a sapphire crystal of Φ1 inch diameter. The thickness of borated polyethylene collimator was optimized to completely attenuate the scattered neutron beam and facilitating transmission of thermal neutron beam from the sapphire crystal for high resolution neutron imaging. In an experiment, the sapphire crystal proved to significantly decrease the fast neutron flux at the detector by over 82%

± 2.76% which subsequently increases the quality of the neutron images (see Fig. 2.7). In addition, a bismuth filter with an optimized thickness of 4 inch was also fabricated to reduce the gamma content of the neutron beam but it was not used in the final construction to avoid alpha particle contamination due to the polonium 210 production by the neutron irradiation of bismuth 210. Instead of bismuth filter, a sapphire filter with a stack of lead sheets was used to decrease the fast neutron and gamma content of the neutron beam.

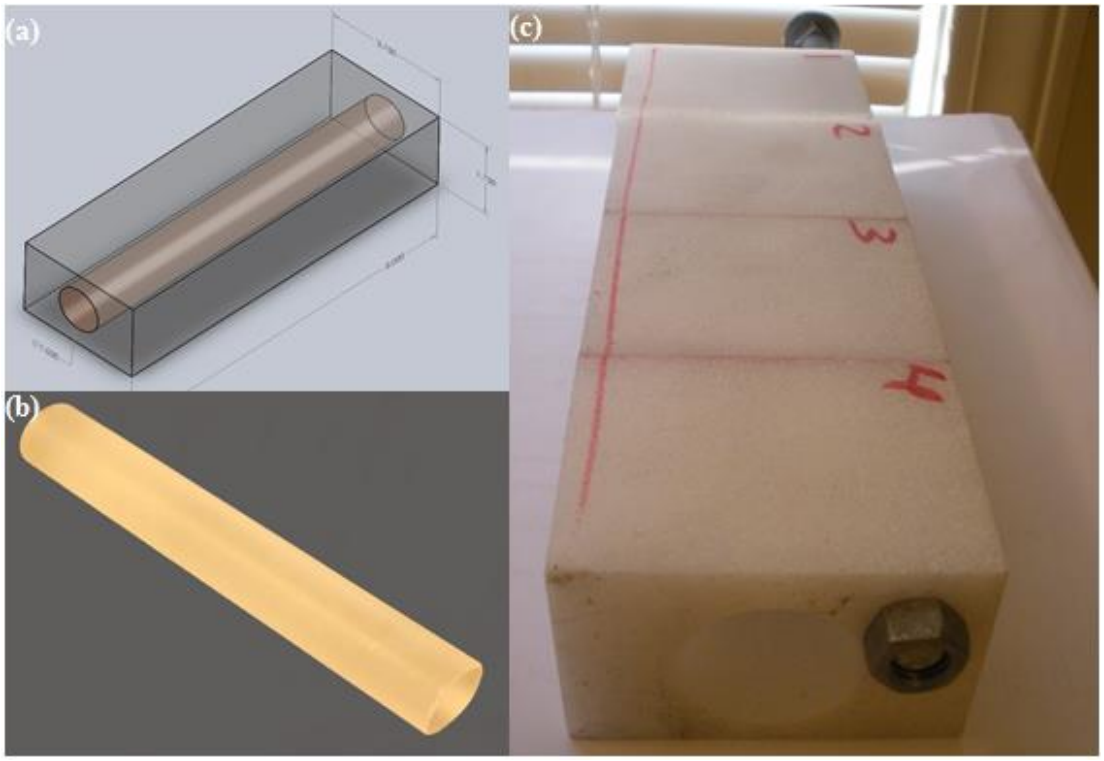


Figure 2.6. 3D Model of the Collimator with a Sapphire Crystal (a), Photograph of the Sapphire Crystal (b), Photograph of the Collimator with the Sapphire Crystal (c)

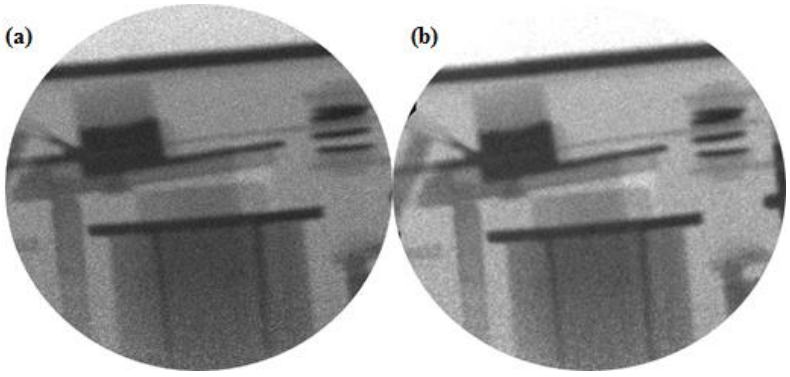


Figure 2.7. Neutron Image of a Power Relay without using the Collimator (a), Neutron Image of a Power Relay with the Collimator (b)

Moreover, ASTM Image Quality Indicators (IQI), a set of beam purity indicator (BPI) and sensitivity indicator (SI), was used to visually inspect the image quality of the neutron imaging module [23-28]. It is important to mention that ASTM IQI indicators are limited to film imaging and are not accepted as the image quality standards for digital neutron imaging. Therefore, MTF, NPS and DQE calculations were used to evaluate the performance of the developed digital neutron imaging system (see Section 4). Still, SI and BPI indicators can be used for the visual inspection of the neutron images and can provide a qualitative estimation for the image consistency and spatial resolution of the imaging module. The Sensitivity Indicator is used to determine the relative quality of the neutron radiographic image. The SI is a step wedge phantom with predetermined different thicknesses of methylmethacrylate and aluminum strips [26, 27]. In addition, four holes with different diameters (127 µm, 254 µm, 508 µm and 254 µm) are present on this phantom to check the resolution of the image. The neutron image of SI shows different contrasts for all nine steps (see Fig. 2.8). This demonstrates that developed neutron imaging module is well optimized in terms of neutron beam diagnostics, and

resulting image quality from the neutron imaging detector. The present set-up can be used to perform high resolution neutron radiography and tomography operations. Furthermore, the BPI was also used for the visual inspection of neutron radiographic images. The BPI can be used for quantitative determination of image quality. BPI is made of a polytetrafluoroethylene block with two each of boron nitride disks, lead disks and cadmium wires. It can be interpreted from the visual inspection of BPI neutron image (see Fig. 2.9) that both cadmium wires exhibits similar contrast as well as sharpness. This confirms consistency with the calculated L/D values and resulting sharpness. Further, the MTF calculation from Cadmium edge phantom is also in good agreement with calculated L/D ratio and BPI visual inspection which verifies the sharpness trend for neutron imaging module. The darker contrast of lead disk compared to polytetrafluoroethylene block indicates that higher pair production content which will result in a darker image. It can be concluded from above visual inspection of ASTM IQI's that present neutron beam and detection geometry is well optimized for imaging operations [25-28].

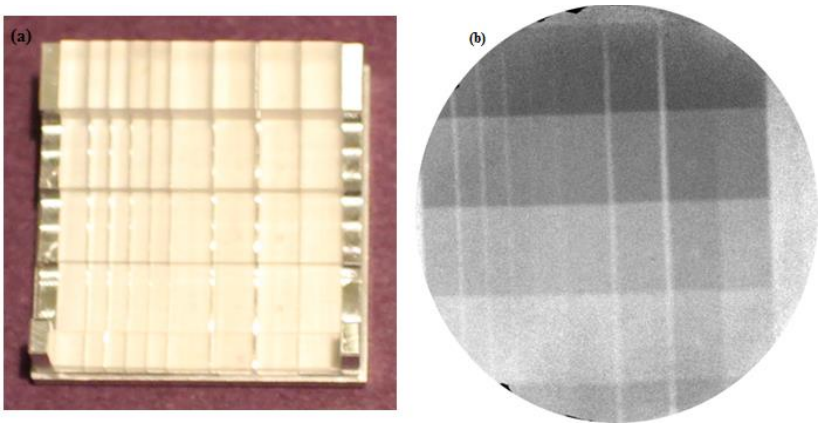


Figure 2.8. Photograph of Sensitivity Indicator (a), Neutron Image of Sensitivity Indicator (b)

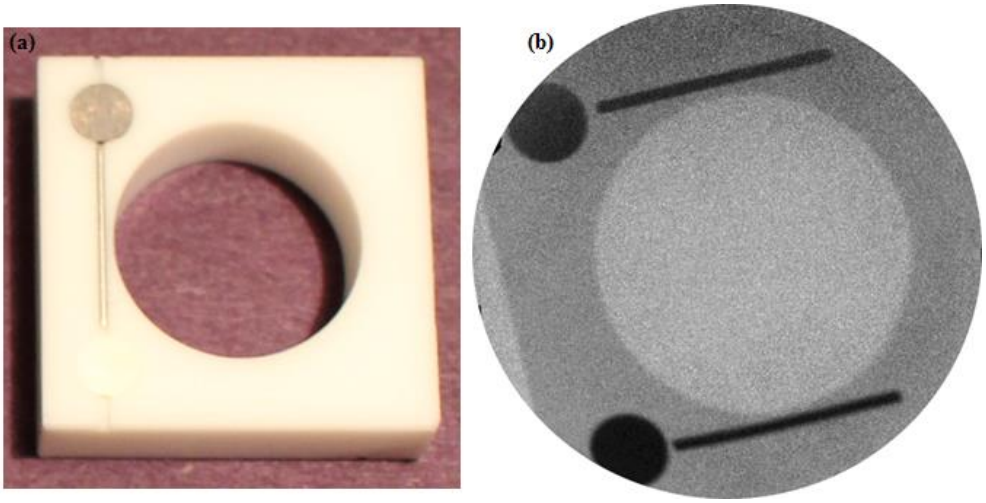


Figure 2.9. Photograph of Beam Purity Indicator (a), Neutron Image of Beam Purity Indicator (b)

## 2.4. DISCUSSION OF TOMOGRAPHY AND APPLIED ALGORITHMS

The three dimensional reconstruction of an imaging object can be performed by taking projection data at different angles. Depending on the beam geometry, the projection data can be of two types:

- Parallel beam projection
- Cone beam projection

The schematic of parallel beam and conical beam geometries are show below (see Fig. 2.10).

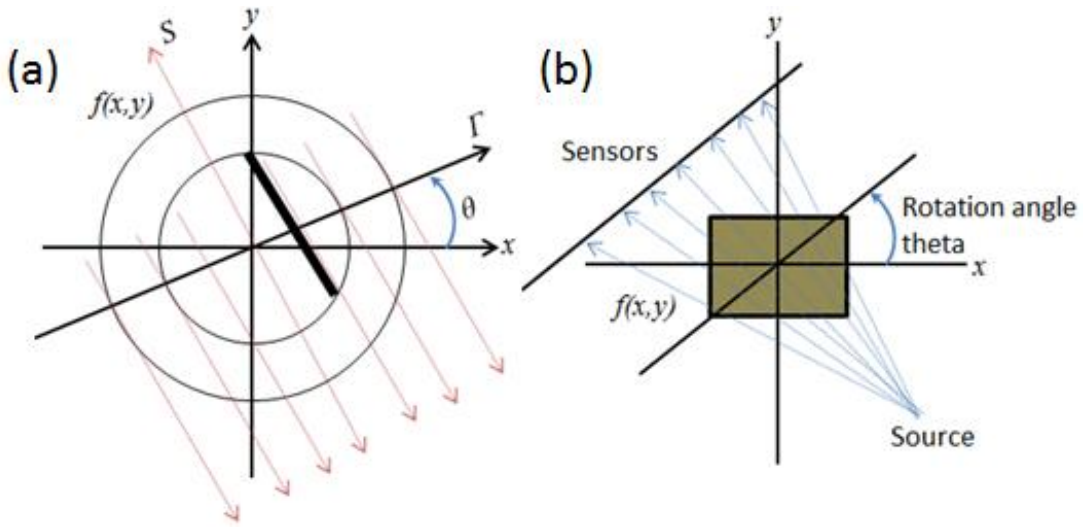


Figure 2.10. Schematic of (a) Parallel Beam Geometry (b) Conical Beam Geometry

In NXCT system operation and three dimensional image reconstructions, parallel beam projection for neutron beam and conical beam projection for X-rays was used.

The parallel beam projection data denoted by $p(r,\theta)$ is Radon transform of the two dimensional neutron attenuation coefficient $f(x,y)$ of the imaging object which can be shown by:

$$p(r,\theta) = R(f(x,y)) \tag{11}$$

Where $x = r\,cos\theta - s\,sin\theta$, $y = r\,sin\theta + s\,cos\theta$, and *r-s* represents the rotated co-ordinate system in counterclockwise direction by angle $\theta$. The stacking of all projection $p(r,\theta)$ for an imaging object is known as the sinogram. The inverse radon transform of the projection data $p(r,\theta)$ provides reconstruction of the sinogram. There are different algorithms available for the reconstruction of the projection data. The commonly employed reconstruction algorithms are Filtered Back Projection (FBP), Convolution Back projection (CBP), wavelet based reconstruction algorithm, iterative

reconstruction techniques, statistical reconstruction techniques and combination of conventional and iterative techniques.

In this research, FBP algorithm has been used for three-dimensional reconstruction of the projection data. In filtered back projection technique, each projection is measured back along the same angle. The back projection for an unknown density line can be given by:

$$b_\theta(x,y) = \int p_\theta(r)\delta(x\cos\theta + y\sin\theta - r)dr \quad (12)$$

Where $b_\theta(x,y)$ represents the back-projected density. The Dirac delta function is denoted by $\delta((x\,cos\theta + y\,sin\theta - r))$ and has a value of one at $r = 0$. The stacking of back projected data over all the angles is called a laminogram and can be represented by the below equation:

$$f_b(x,y) = \int_0^\pi b_\theta(x,y)d\theta = \int_0^\pi \int_{-\infty}^{+\infty} p_\theta(r)\delta(x\cos\theta + y\sin\theta - r)drd\theta \quad (13)$$

The distorted image of an imaging object is represented by laminogram and need to be corrected. The impulse response of $\delta$ function can be written as:

$$h_b(r) = \int_0^\pi \int_{-\infty}^{\pi} \delta(r)\delta(r\cos(\theta - \phi) - r)drd\theta = \frac{1}{r} \quad (14)$$

By knowing impulse response and applying linear system theory the following relationship can be established as given below:

$$f_b(x,y) = f(x,y) * {}^{1}/_{r} \quad (15)$$

Where symbol $*$ represents convolution operation and ${}^{1}/_{r}$ denotes the blur in the actual image. The two dimensional transformation of above equation can be expressed as:

$$F_b(k,\theta) = F(k,\theta)\frac{1}{k} \quad (16)$$

Where *K* refers is the Fourier frequency. The blurring can be removed by FBP technique. In this scenario, the central slice theorem is employed for the computed tomography. The 2D Fourier transform of $f(x,y)$ is assumed to be $F(k_x, k_y)$. This can be expressed by the following equation:

$$\mathrm{F}(\mathrm{k_x}, \mathrm{k_y}) = \int_{-\infty}^{\theta}\int_{-\infty}^{\theta} \mathrm{f(x,y)exp}\{-2\pi\mathrm{j}(\mathrm{k_x x} + \mathrm{k_y y})\}\mathrm{dxdy} \qquad (17)$$

In above equation, $k_x$ and $k_y$ represents the orthogonal Fourier frequencies with units of radians per distance. $P_\theta(k)$ is one-dimensional Fourier transform of the projection $p_\theta(r)$ and can be shown by:

$$\mathrm{P_\theta(k)} = \int_{-\infty}^{\theta} \mathrm{p_\theta(r)exp(-2\pi jkr)dr} \qquad (18)$$

The $\theta$ can be varied from *0* to $\pi$ radians and can be stacked to get $P(k,\theta)$. According to central slice theorem

$$\mathrm{P(k,\theta)} = \mathrm{F}(\mathrm{k_x}, \mathrm{k_y})$$

$$\mathrm{k_x} = \mathrm{k\cos\theta}$$

$$\mathrm{k_y} = \mathrm{k\sin\theta}$$

$$\mathrm{k} = \sqrt{\mathrm{k_x^2} + \mathrm{k_y^2}}$$

In short, the 1d Fourier transform in r of the Radon transform of a function is equal to the 2D transform of that function.

From CST, equation can be written as

$$f_b(x,y) = \int_0^{\pi} b_\theta(x,y)d\theta$$

$$= \int_0^{\pi}\int_{-\infty}^{+\infty}\left[\int_{-\infty}^{\infty} F(k,\theta)exp(2\pi jkr)dk\right]\delta(x\,cos\theta + y\,sin\theta - r)drd\theta$$

Integration of above equation reduces to

$$\mathrm{f_b(x,y)} = \int_0^{\pi}\int_{-\infty}^{+\infty} \mathrm{F(k,\theta)exp\{2\pi jk(x\cos\theta + y\sin\theta)\}dkd\theta} \quad (19)$$

Comparison of above equation with 2D Fourier transform of the 1D Fourier transform of the projection data is

$$f(x,y) = \int_0^{2\pi}\int_{-\infty}^{+\infty} F(k,\theta)exp\{2\pi jk(x\,cos\theta + y\,sin\theta)\}kdkd\theta$$

$$= \int_0^{\pi}\int_{-\infty}^{+\infty} F(k,\theta)exp\{2\pi jk(x\,cos\theta + y\,sin\theta)\}|k|dkd\theta$$

$$\mathrm{f(x,y)} = \int_0^{\pi}\int_{-\infty}^{+\infty} \frac{\Im\{p_\theta(r)\}\bullet|k|}{|k|}\mathrm{exp\{2\pi jk(x\cos\theta + y\sin\theta)\}|k|dkd\theta} \quad (20)$$

Above equation is the FBP reconstruction technique. Similarly, another equation can be derived for conical beam geometry reconstruction [29, 30].

# 3. DESIGN AND DEVELOPMENT OF A NEUTRON/X-RAY COMBINED COMPUTED TOMOGRAPHY SYSTEM

## 3.1. INTRODUCTION

A new method for non-destructive analysis has been developed using a combined neutron/x-ray imaging system at the Missouri Science &Technology Reactor (MSTR). The interactions of neutrons and x-ray photons with matter produce differing characteristic information, resulting in distinctly different visual images. In order to obtain a more comprehensive picture of the structural and compositional data for a desired object, a prototype imaging system has been designed which utilizes neutron and x-ray imaging simultaneously without obstructing the beam geometry for each imaging mechanism. The current system is optimized for the imaging of small to medium sized objects of 0.5 mm to 50 mm. This new imaging capability in place at the MSTR promises great advances in the field of non-destructive testing, especially for nuclear engineering, nuclear medical science, and material science research. In an imaging object, a range of atomic number values and thermal cross sections may be present. Where multiple materials having similar atomic number and differing thermal cross section or vice versa may be present, exclusive neutron or x-ray analysis may exhibit shortcomings in distinguishing interfaces. However, fusing the neutron image and x-ray image into a combined image offers the strengths of both and may provide a superior method of analysis. In this section, a novel combined x-ray and neutron imaging system will be introduced for superior analysis of certain imaging objects. Design details of experimental set-up and examples of preliminary imaging tests from individual modality are detailed. The concept of NXCT can be useful for concealed material detection,

material characterization, investigation of complex geometries involving different atomic number materials and real time imaging for in-situ studies.

## 3.2. DESIGN AND PARAMETRIC DETAILS OF THE NXCT SYSTEM

Nondestructive testing using neutron or x-ray beams is an indispensable tool for obtaining structural and compositional data [1-3]. The neutron and x-ray imaging methods display different characteristics of the imaging object due to the different transmission characteristics of x-rays and neutrons inherent in each material. Presently, both neutron and x-ray imaging are widely employed in research and industry for non-destructive testing applications. Both neutron and x-ray imaging have certain characteristic strengths and limitations. When applied individually, neutron and x-ray imaging often fails to obtain a comprehensive analysis of the desired object. In the past, a comprehensive analysis was performed by using separate experimental set-up for neutron and x-ray imaging [6, 7, 31, 32]. Such a system can be extremely difficult to calibrate, and is prone to measurement inaccuracies. The separate experimental set up does not allow for instant evaluation of imaging objects, and different experimental conditions could significantly affect the overall imaging performance. As a solution, we propose to develop and demonstrate successful operation of a neutron/x-ray combined computed tomography (NXCT) system. This is the first approach to develop a neutron and x-ray combined computed tomography system.

The NXCT system design involves consideration of various factors which can be mainly divided into three categories that influence the performance of the overall system: operation, image quality, and data analysis. These factors can be further elaborated in sub

categories (see Fig. 3.1) and can be effectively utilized to develop the advanced radiation imaging systems. The spatial resolution, field of view, dynamic range, and acquisition time are the main design parameters considered in developing the NXCT system. Additionally, adequate sample positioning, and accommodation of beam geometries are crucial factors to devise the system. Furthermore, proper functioning of the overall system requires synchronization of system components and their software controls. Finally, algorithm techniques for instant image fusion, their characterization, and image post processing are highly desirable features. The combined neutron and x-ray imaging technology has potential applications in the evaluation of nuclear fuels, biomaterials, bioactive glasses, rock samples, automobile parts, and as well as particle flow tracking in complex geometries. The NXCT system could significantly improve the current nondestructive testing methods and provide for a solid foundation towards future research.

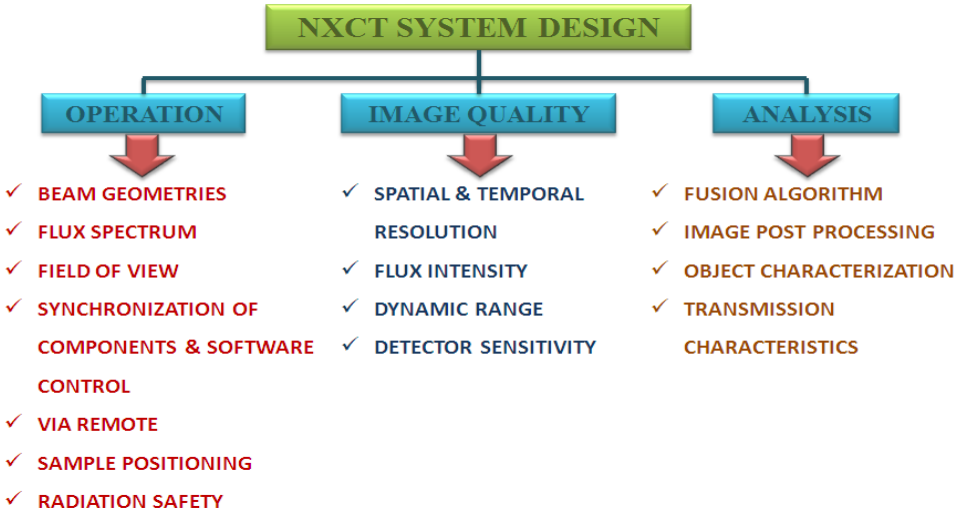


Figure 3.1. Overview of NXCT System Design and Associated Factors

### 3.3. DETAILS OF THE NXCT SYSTEM

The NXCT system was designed and developed (see Fig. 3.2) in the Missouri University of Science & Technology Reactor (MSTR). Audio/visual alarms in conjunction with the entrance door disconnect switch provide foolproof radiation safety for each experiment. The MSTR is a heterogeneous, pool-type research reactor. The reactor core is cooled by the natural convection of light water, moderated by water, and reflected by water and graphite. The reactor core is composed of approximately 20 fuel elements positioned in an aluminum grid plate. A stepped beam port (see Fig. 3.3) provides a beam of neutrons for irradiation experiments. The beam port protrudes through the pool wall and extends into the reactor pool near the core (see Fig. 3.4).

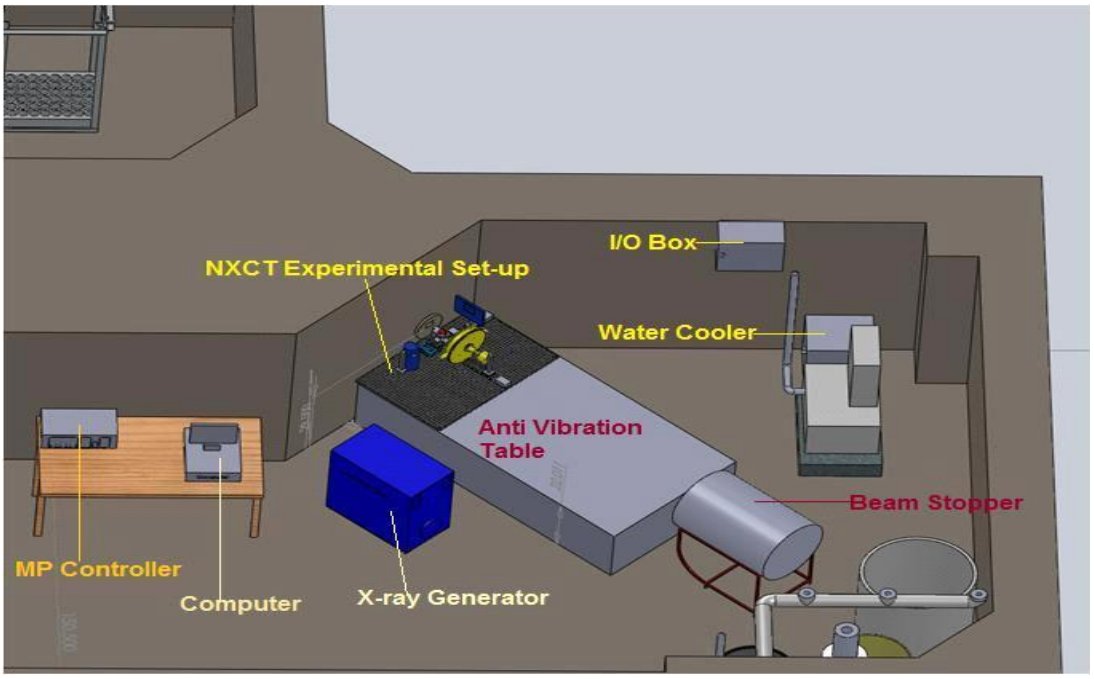


Figure 3.2. Isometric View of the NXCT Facility

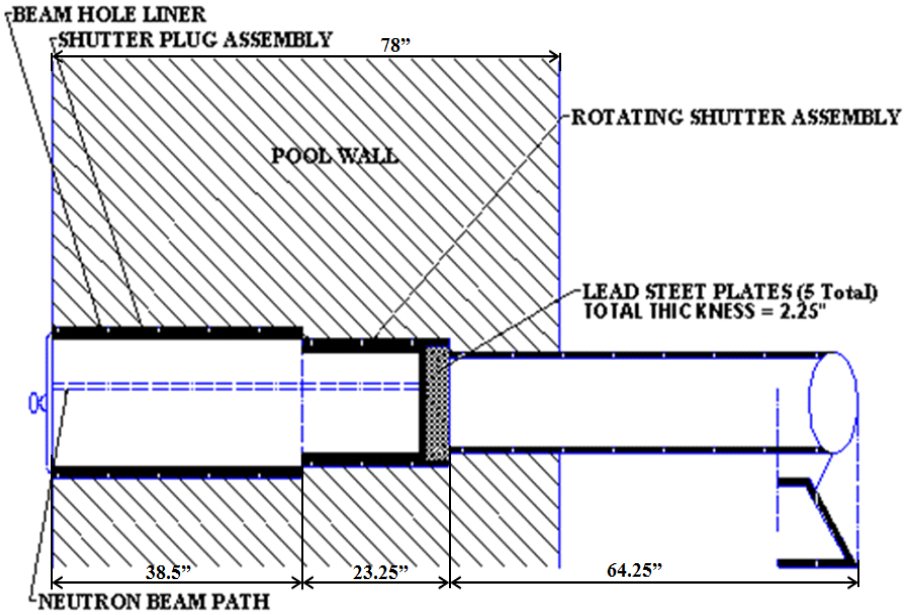


Figure 3.3. MSTR Neutron Beam Path and Beam Port, (b) Schematic of MSTR NXCT Facility

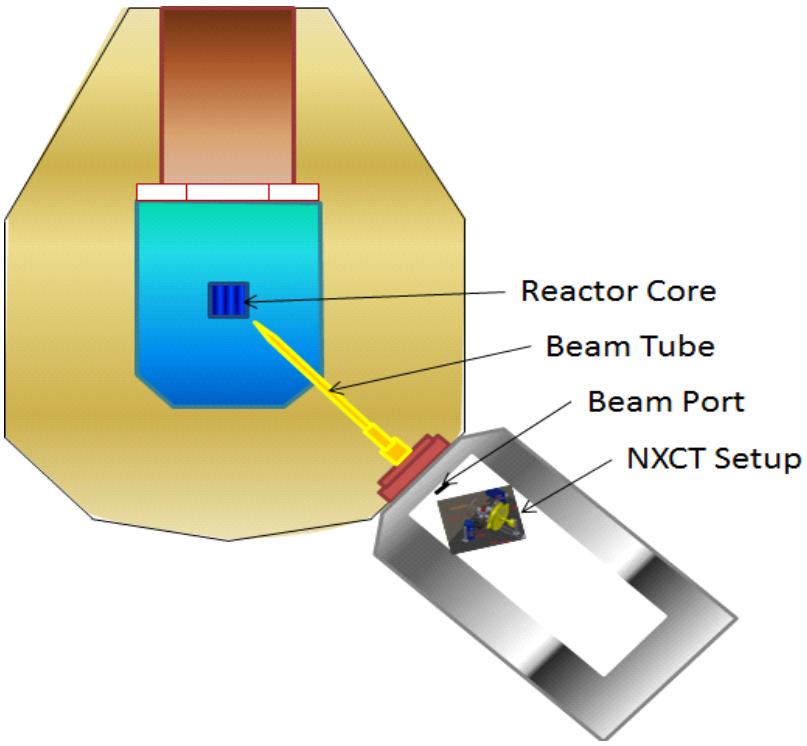


Figure 3.4. Aerial View of the MSTR & NXCT Facility

The open end of the aluminum beam tube terminates in the basement experimental area where the NXCT system is located. The beam tube is closed at the reactor end. A shutter assembly composed of two parts can be used to obtain a collimated beam of neutrons. It consists of a plug containing a beam guide having a cross-section of 70 x 44 $mm^2$ and a shutter which provides an extension to the beam guide in the "Open" position and a radiation shield in the "Closed" position. Both positions are remotely controlled from the control room where the open/closed indicator is displayed. At 200 kW, the neutron beam port produces an average flux value of 1.08E8 $n/cm^2$-s. The Cd ratio ($R_{cd}$) at beam port is 9.82 which is an acceptable value for a good quality neutron beam. The solid angle of the neutrons exiting the port is assumed to be small, because the Boral-lined neutron path provides a substantial degree of collimation. The neutron imaging sensor is a micro channel plate (MCP) based detector (Outer diameter: 33 mm, thickness: 0.8 mm, ~ L/D: 100: 1 and pore diameter: 8.5 µm) coupled to fast position sensing circuit with readout electronics (Equivalent pixel pitch: 33µm, rate capability: 1 MHz, multi-hit dead time: 10-20 ns, dynamic range: $10^7$, field of view: 25.4 mm and position resolution < 0.1 mm).

In x-ray imaging, a microprocessor controlled x-ray generator and tube (kV range: 20-225, mA range: 0-30, output rise time: 20 kV per second, focal spot: 0.4 x 1 $mm^2$) is present as an x-ray source. The x-ray sensor is a scintillator plus CMOS (complimentary symmetry metal oxide semiconductor) based sensor (Pixel pitch: 48 µm, dynamic range: 4000:1, frame rate: 2.7 FPS and field of view: 50 x 50 mm).

The design of the NXCT sample positioning system allows combined imaging operation with precise resolution and accuracy during imaging experiments (see Table

3.1) via remote operation (see Fig. 3.5). The sample positioning device provides positioning in the X, Y and Z direction, and includes precise rotational motion for tomography applications. In addition, the zoom and distance of both the neutron and x-ray sensors can be adjusted. The complete design of NXCT system includes various components and developed system is available at MSTR (see Fig. 3.6).

Table 3.1 Physical Characteristics of the NXCT Sample Positioning System

| **Physical Parameter** | **Linear Stage** | **Rotation Stage** | **X-Y Stage** | **Z-Axis Stage** |
|---|---|---|---|---|
| **Micro-step Size Resolution** | 0.49609 μm | 0.00023 degree worm gear ratio | 0.1905 μm | 0.40 mm |
| **Speed Resolution** | 0.00465 mm/s | 13.2 degree/s | Up to 29 mm/s | 1.0 mm/s (Small Load) 0.5 mm/s (Maximum Load) |
| **Accuracy** | +/-15 μm | +/-0.05 degree | +/-21 μm | 5% Step acc. |
| **Travel Distance** | 300 mm | 360 degree rotation | 101.6 mm | 50 mm |
| **Load Capacity** | 200 N-cm (Maximum Cantilever Load) | 20 kg | 10 kg | 15 kg |

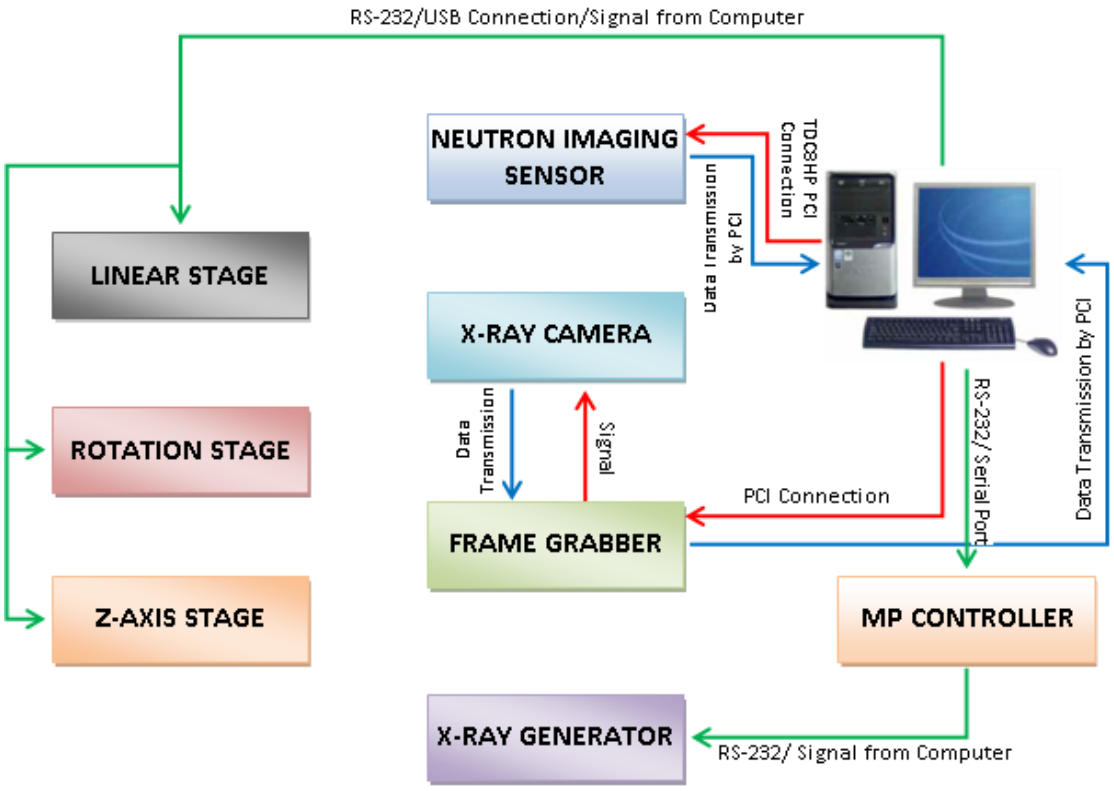


Figure 3.5. Schematic of Control Logic for NXCT System

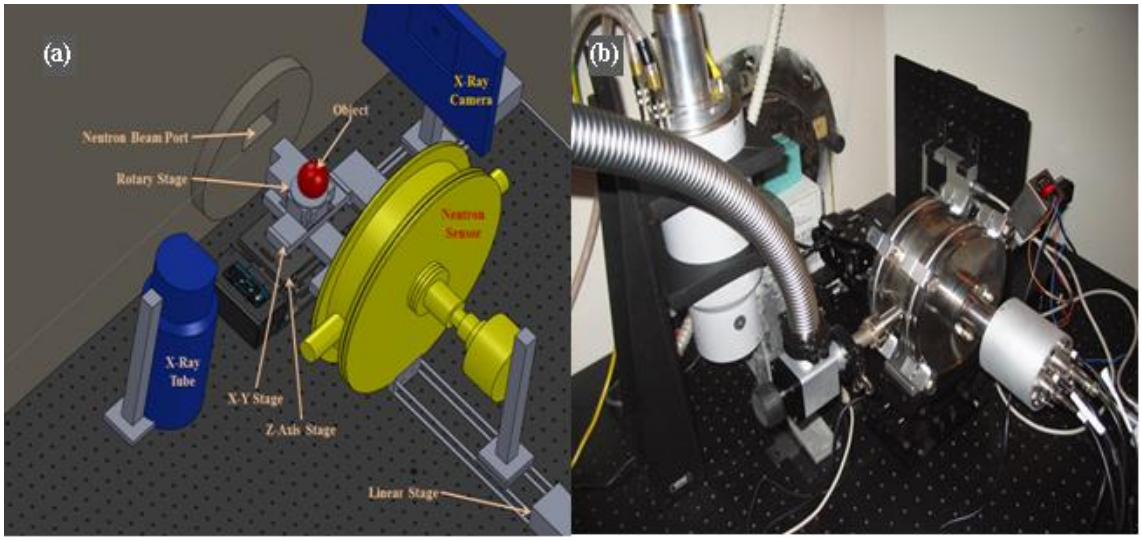


Figure 3.6. Design of NXCT System (a), Developed NXCT System (b)

Lastly, it is important to characterize the neutron and x-ray beam properties to analyze the interaction of neutrons and x-rays with the target materials. It is necessary to consider the differing geometries of the neutron and x-ray beams. The neutron and x-ray beams are assumed to have parallel and conical geometries respectively. The MCNP model and actual experiments were used to obtain the full power neutron flux spectrum (see Fig. 3.7) for the MSTR and used in this research to calculate flux values [16]. The thermal neutron contributes 39 % of the total flux at the core which is 2.94E12 n/cm$^2$-s (see Table 3.2). Similarly, photon flux spectrum at 1 m from the x-ray source was simulated (see Fig. 3.8) using SpekCalc software and used in this research to calculate flux values [33].

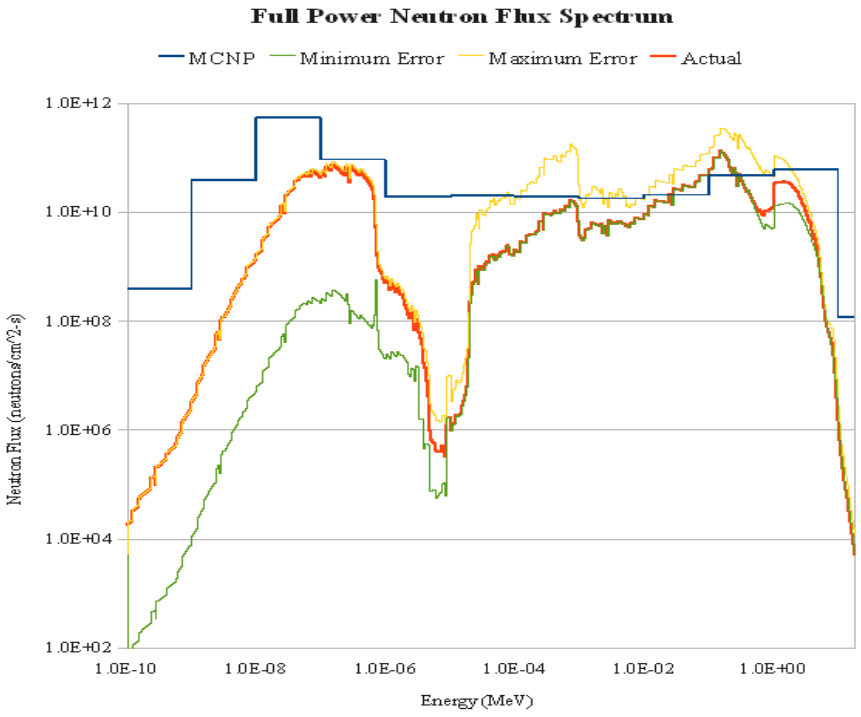


Figure 3.7. Full Power Neutron Flux Spectrum for the MSTR Characterizing Thermal, Intermediate and Fast Neutrons

Table 3.2 Thermal, Intermediate, and Fast Neutron Fluxes for Full Power

| Energy | Flux (neutrons/cm$^2$-s) | Flux Share of total |
|---|---|---|
| **Thermal** | 2.94E+12 ± 1.9E+10 | 38.99% |
| **Intermediate** | 1.86E+12 ± 3.7E+10 | 24.62% |
| **Fast** | 2.65E+12 ± 3.0E+3 | 35.15% |
| **Total** | 7.55E+12 ± 5.7E+10 | 100.00% |

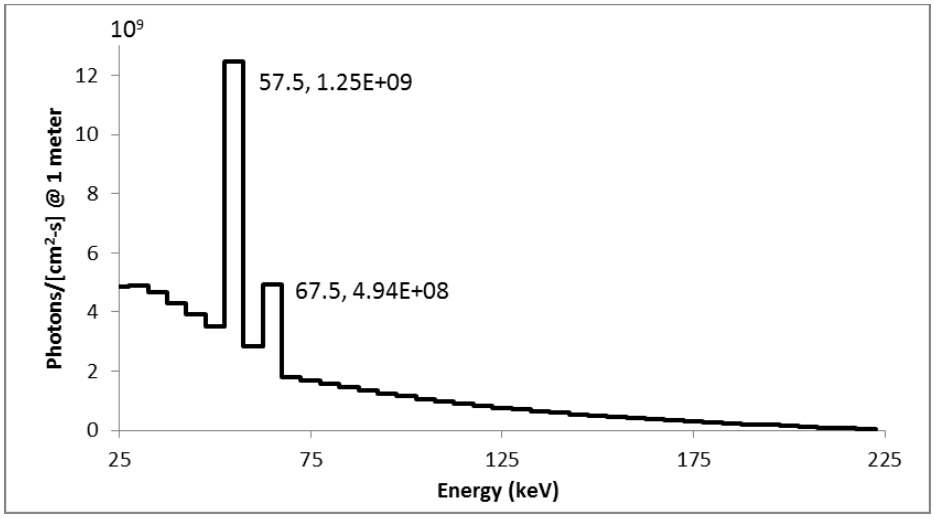


Figure 3.8. Photon Flux Spectrum of MSTR X-Ray Source

## 3.4. THE NEUTRON AND X-RAY SENSOR OPERATION

**3.4.1. The Neutron Sensor Description.** The neutron sensitive MCP detector was chosen with the delay line anode for the neutron imaging module of the NXCT system. The MCP detector with the delay line anode has advantages compared to the optical camera based system. In the MCP based delay line anode configuration, the imaging object can be placed directly next to the detector window compared to the optical camera based system where a mirror and a lens are needed to capture an image.

Replacement of the optical camera readout with the delay line anode helps to increase the sensitivity of the imaging system, because there is no signal loss as opposed to the case of image reflection by the mirror. Therefore the MCP based neutron imaging detector with the delay line anode is also better in terms of image acquisition time and overall ease of operation for tomography applications. For the stated reasons, the MCP based detector with the delay line anode was incorporated in the combined NXCT system design. The MCP based detector with the delay line anode includes several components (see Fig. 3.9): detector head, feed through with signal de-coupler, power supply, amplifier, constant fraction discriminator (CFD), and time-to-digital converter (TDC).The neutron sensitive MCP in the detector has a high neutron capture cross section and an optimal reaction product escape probability to create an electron avalanche pulse. The $^{10}B$ (n, α) $^{7}Li$ capture conversion process for thermal neutrons creates short range (3.5μm) alpha particles and lithium nuclei, which further creates free secondary electrons in adjacent MCP channels [34]. These electrons cascading in the channels can be amplified up to $10^6$ times into a detectable signal. In short, the MCP detector with the delay line anode applies an electron particle counting technique and each counted particle, with time and position information, aids to produce the digital image. The MCP neutron detector has a delay line anode readout which involves careful optimization of constant fraction discriminator, thresholds, frequency amplifiers and power supply voltages which will eventually contribute to the spatial resolution of the overall neutron imaging module.

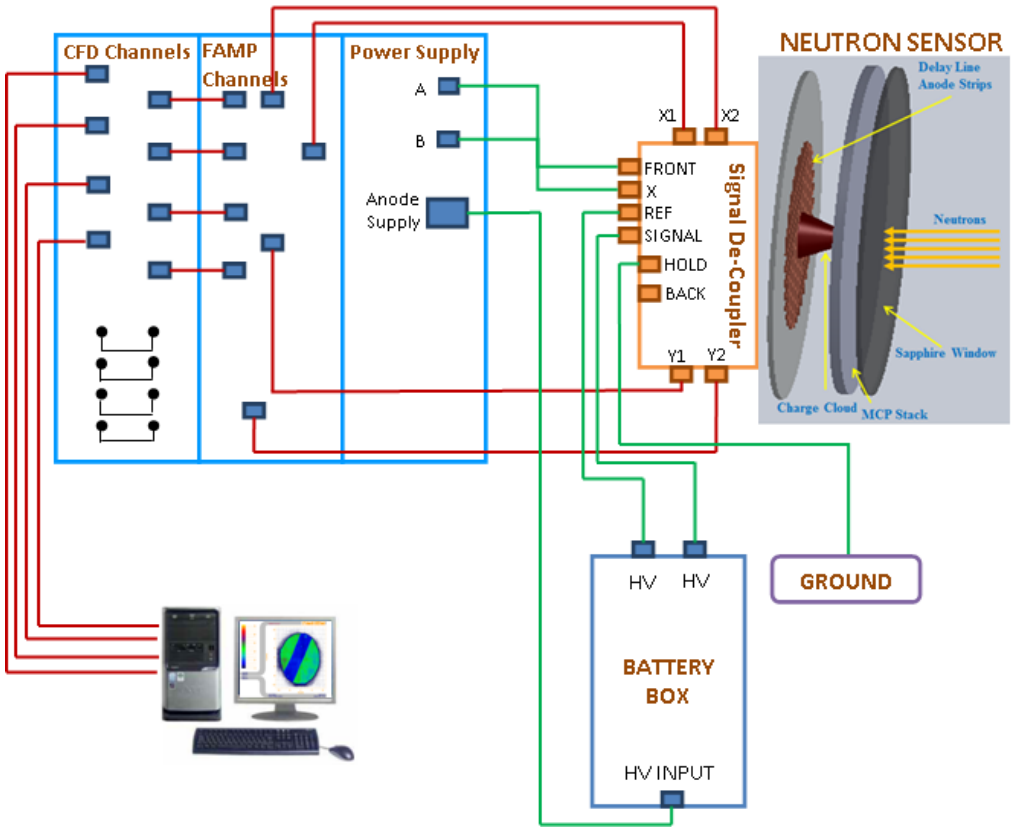


Figure 3.9. Neutron Image Sensor Description

**3.4.2. The X-Ray Sensor Description.** The scintillation screen plus CMOS detector was chosen for the x-ray imaging module of the combined NXCT system. The detector includes different components: a scintillation screen, photodiode array, sensor electronics, camera controller, and a frame grabber device. The detector has a gadolinium oxysulfide ($Gd_2O_2S$) scintillation screen on top of the photodiode array (see Fig. 3.10). The operation of the detector is similar to other scintillation detectors, where incident x-rays get converted to light and this light is detected by photodiodes which form a digital image.

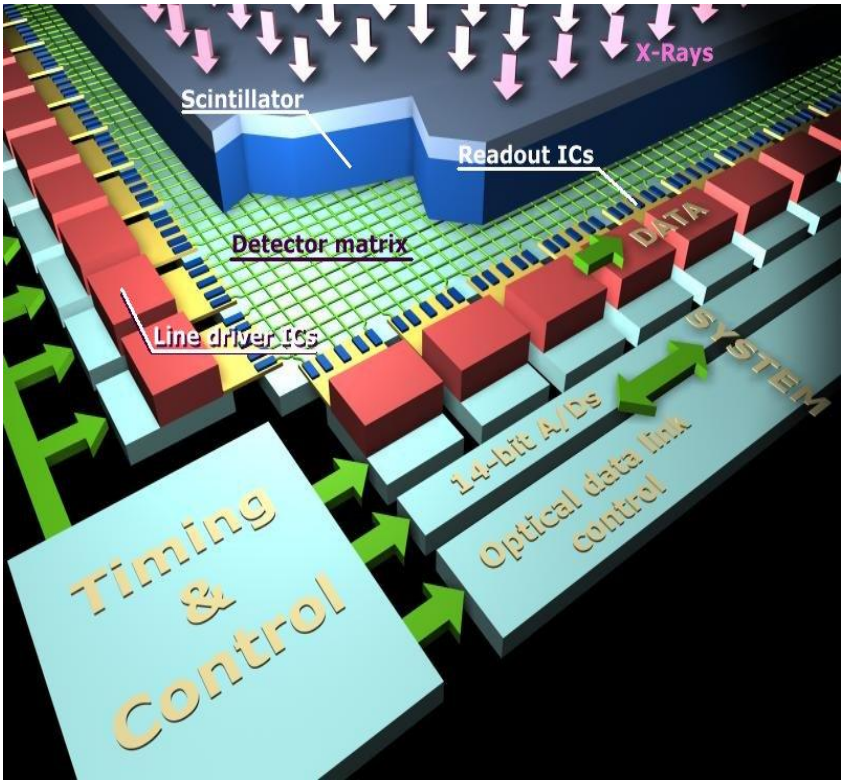


Figure 3.10. X-ray Image Sensor Description [35]

### 3.5. IMAGE SIMULATION & UTILITY OF THE NXCT SYSTEM

A set of simulation studies was performed to demonstrate the utility of the combined NXCT system. Imaging physics principles together with reasonable assumptions allowed for the simulation of the digital images and their fusion, in order to understand the process. In order to produce artificial neutron and x-ray images, for example, a combination of three cubes composed of Beryllium, Boron and Europium, each with thicknesses (2 cm) and dimensions (2 x 2 cm), was simulated using the MATLAB code. The attenuation calculations were based on the linear attenuation coefficient values [36] and thermal cross sectional values [37] of respective materials. The mono-energetic x-ray energy (50 keV) and thermal neutron energy (0.0253 eV) were

considered to simulate the x-ray and neutron interaction with the imaging object. Since the linear attenuation coefficient values for Beryllium (A=4) and Boron (A=5) are in the similar order of magnitude, it would be difficult to differentiate the materials using x-ray imaging (see Fig. 3.11). Similarly, Boron (A = 5) and Europium (A=63) have comparable thermal cross sectional values for the neutrons, making material identification from the neutron imaging difficult. However, the combination of neutron and x-ray image can identify all three materials in a fused image. The pixel based fusion algorithm was used to fuse the neutron and x-ray images. The descriptions of fusion algorithms for neutron and x-ray images are provided in other section of this paper.

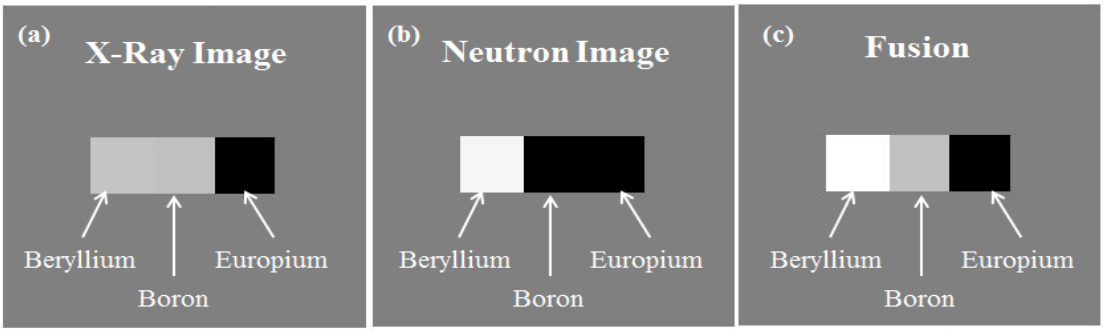


Figure 3.11. Computer Simulated (a) X-ray, (b) Neutron Image and (c) Fused Image of Different Materials

In the second phase of research, the preliminary imaging tests were performed to establish the proper functioning of the NXCT system. The imaging objects were selected based on their attenuation characteristics, size, and distribution of materials in the objects. In the testing of the neutron imaging module, the drilled cadmium strip was imaged (see

Fig. 3.12). Since the cadmium strip is an excellent neutron absorber, the image testing produced a high contrast image of the cadmium strip, which clearly shows the holes in the strip. Similarly, the x-ray imaging of a memory flash drive, rock sample, wooden pencil and borosilicate test tube was performed. The x-ray sensor (pixel pitch 48μm) was expected to identify miniscule details of the imaging object.

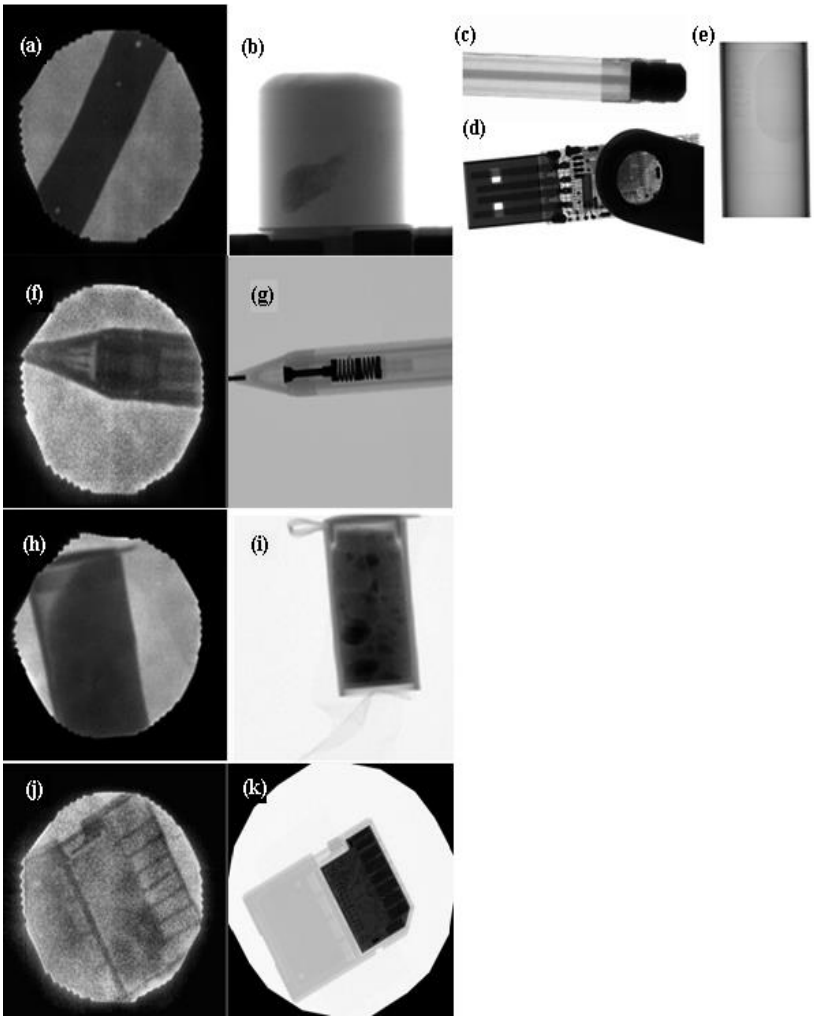


Figure 3.12. Preliminary Imaging Test from MSTR NXCT System. (a) Neutron Image of Cadmium Strip with Small Holes. X-Ray Image of, (b) Rock, (c) Wooden Pencil, (d) Memory Flash Drive, (e) Borosilicate Test tube. (f - k) Neutron, X-Ray Images of Identical Objects Utilizing MSTR NXCT Imaging System

The X-ray image of the flash drive clearly shows the circuits and associated parts. Furthermore, a gypsum rock sample was investigated to identify the water diffusion phenomenon in rocks; structural and compositional information is also visible and can be used to identify similar issues.

Once the initial simulation and preliminary testing was performed, the identical objects from the neutron and x-ray images were compared (see Fig. 3.12). In the mechanical pencil image, it is evident that the plastic parts are visible in the neutron image while the metal parts are visible in the x-ray image. The image of the plastic vial containing the borax (sodium borate) powder also confirms the distribution of boron material from neutron imaging and sodium material from the x-ray imaging by producing different contrast images. Similarly, the plastic parts for memory flash drive cards were traceable in the neutron image and the metal parts were traceable in the x-ray image. The neutron and x-ray images of the identical objects can be fused further with different algorithm approaches and can also be optimized to retain all possible structural and compositional information.

## 3.6. NDT APPLICATIONS

A series of phantoms was prepared based on structural, compositional, and attenuation characteristics to demonstrate the applications of the NXCT system. First, a screw driver, a perforated cadmium strip, and a nylon washer were mounted on a 1.25 cm thick lead sheet. The combined imaging was performed at 0.0253 eV for neutrons and 85 kV/1.5 mA for X-rays (see Fig. 3.13). The X-ray image was unable to completely image the screw driver, part of the cadmium strip and the nylon washer because the X-rays were

unable to penetrate the lead sheet. Conversely, in the neutron image, all of the above mentioned objects, except for the lead sheet, are clearly visible. Furthermore, to emulate the traditional approach for explosive detection, a plastic vial containing lead spheres and a punched thumb pin were constructed. The X-ray image of this vial clearly displayed the lead spheres as well as the metal part of the thumb pin, but did not clearly show the plastic parts of the vial or thumb-pin; however, the plastic parts within the neutron image were clearly visible. Neutron imaging has the ability to detect light atomic number materials, including typical explosive materials. One immediately obvious application would be during the scanning of airport baggage, especially lead-covered items that conceal plastic weapons or explosive materials.

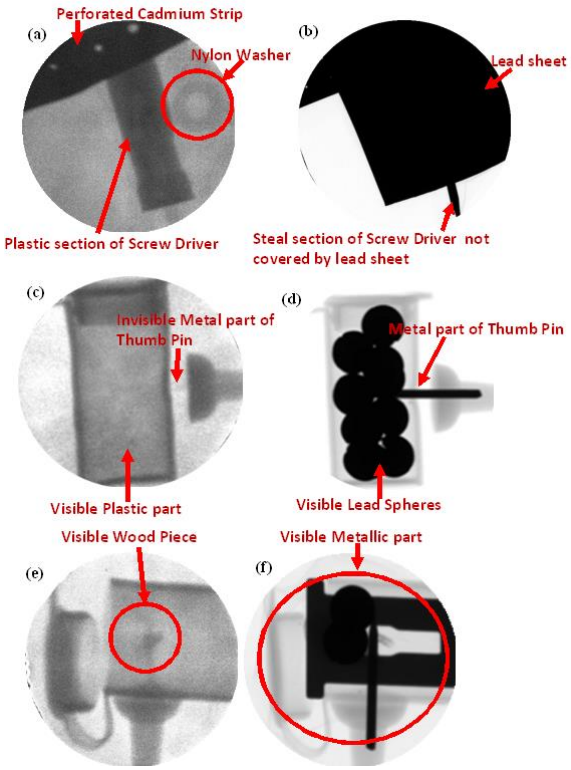


Figure 3.13. Neutron and X-ray Images of Different Constructed Phantoms

More importantly, low energy X-rays, and CZT-based multi-energy X-ray detectors [38-44] may not be a viable option for detecting plastics or explosives covered with a thick lead material. A combined NXCT system holds better prospects for security applications. NXCT imaging was done (see Fig. 3.14-3.19) using different objects, including artificial fishing bait, a plastic vial containing plastic strips and metal wire, a screw driver, and an organic mint tablet. The purpose of conducting combined imaging experiments using the above objects was to show the importance of the NXCT system in terms of material characterization. The interactions that neutrons and X-rays have with materials are characteristically unique, causing distinct image production. Images with poor contrast, due to severe or poor radiation attenuation, may be improved through the fusion of another imaging method (see Fig. 3.14, 3.15). For example, isotopes of the same element will be indiscernible using X-ray imaging because of the identical atomic number, but can be identified by neutron imaging because of the difference in nuclear cross section. Combining these two imaging techniques should provide enhanced structural and compositional information about certain imaged objects (see Fig. 3.14, 3.15). There is a pixel-based fusion algorithm that is used for artificial image fusion for grey scale images (see Fig. 3.14).

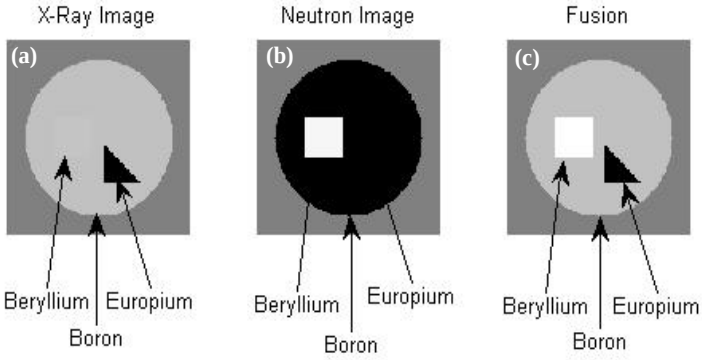


Figure 3.14. Computer Simulated (a) X-ray, (b) Neutron Image and (c) Fused Image of Different Materials

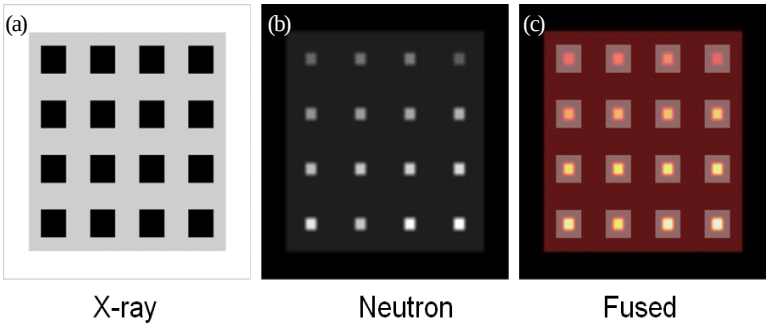


Figure 3.15. Computer Simulated Image Showing Different Borax Concentration from (a) X-ray, (b) Neutron and (c) a Fused Color Image Retains Complete Material Information

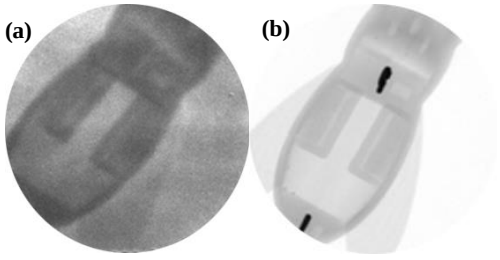


Figure 3.16. The Image of an Artificial Fishing Bait: (a) Neutron Image Shows the Plastic Parts with High Contrast, (b) X-ray Image Shows the Metallic Part with High Contrast

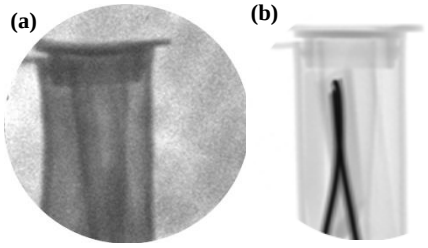


Figure 3.17. The Image of the Plastic Vial Containing Plastic Strips and a Metal Wire Confirms the Presence of Plastic Material from (a) Neutron Imaging and a Metal Wire from (b) X-ray Imaging by Producing Different Contrast Images

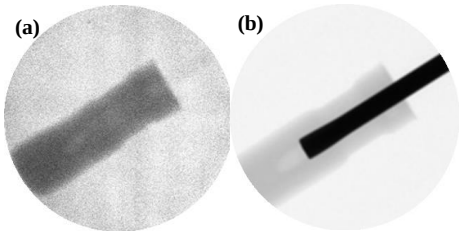


Figure 3.18. The Image of a Screw Driver: (a) The Neutron Image Clearly Shows the Plastic Section, (b) The X-ray Image Shows the Metallic Section

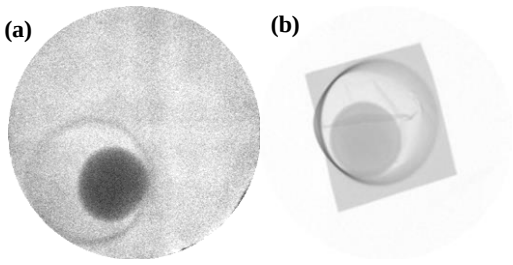


Figure 3.19. The Image of the Organic Mint Tablet in a Metallic Packaging Produces (a) a High Contrast Image of an Organic Tablet from Neutron Imaging and (b) a High Contrast Image of Metallic Packaging from X-ray Imaging

The NXCT system has research and development applications across a broad range of disciplines and is particularly useful in nuclear engineering and the field of non-

destructive analysis. Some of the most interesting research and development applications may include:

- Non-destructive testing of structural components such as those in airplane wings and advanced ceramic and refractory materials.
- Non-destructive evaluation of nuclear fuel materials.
- Particle tracking in complex flows such as in pebble bed nuclear reactors.
- Improved research and development approaches in the areas of biomaterial research, such as artificial bone materials, bioactive glass, and other biological engineering areas.

## 3.7. NEUTRON & X-RAY TOMOGRAPHY

In the second part of this research, tomography experiments were carried out using a NXCT system. The classical filtered back projection (FBP) algorithm was used for neutron tomography. The Feld Davis Kamp (FDK) algorithm was used for X-ray tomography. In the first set of tomography experiments, neutron and x-ray tomography was performed on a part of the power relay switch (see Fig. 3.20). The outer plastic structure of the power relay switch is visible in the neutron tomography image (see Fig. 3.21). Furthermore, a cross-sectional view of the power relay switch provides more information by showing the metal wires inside of it (see Fig. 3.21). Conversely, in the X-ray tomography, the metal structure is visible and the cross sectional view of relay switch shows the hollow structure of it. Certainly, images from neutron and X-ray tomography yield complete information of this object, which can be very crucial for inspection and quality control of similar items. Moreover, NXCT techniques can be effectively applied

for various nondestructive testing applications. To emulate a more traditional approach for concealed material detection, a phantom was constructed using a plastic vial containing lead spheres and water balls encased in polymer coating (see Fig. 3.22). The result from neutron and X-ray tomography clearly segregates low and high atomic number materials (see Fig. 3.23, 3.24). In the X-ray images, water balls were not visible but lead spheres were clearly visible (see Fig. 3.23, 3.24). It is observed that high atomic number materials can conceal low atomic number materials, e.g. explosives, drugs or other similar materials, from being detected. However, the NXCT system can be highly useful in concealed material detection and provide accurate description of the scanned objects (see Fig. 3.24).

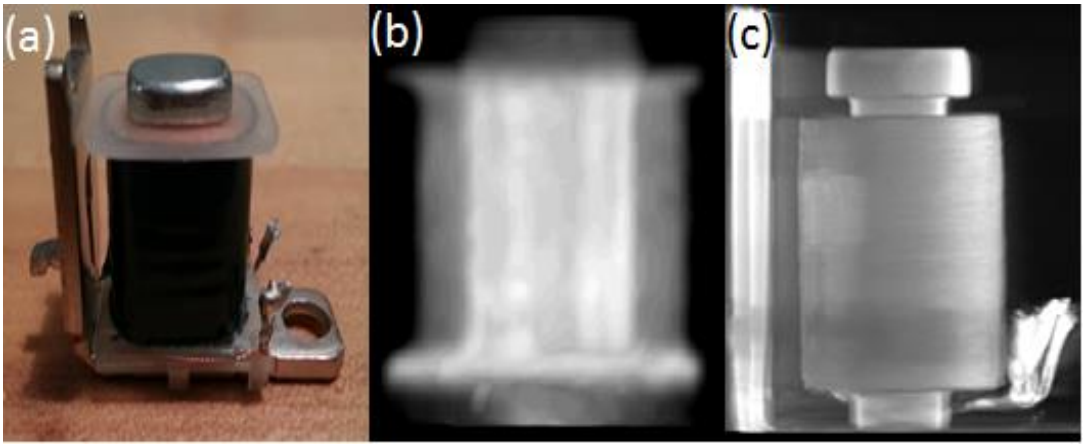


Figure 3.20. Photograph of a Part of a Power Relay Switch (a), 3D Reconstructed Neutron Image (b), 3D Reconstructed X-ray Image (c)

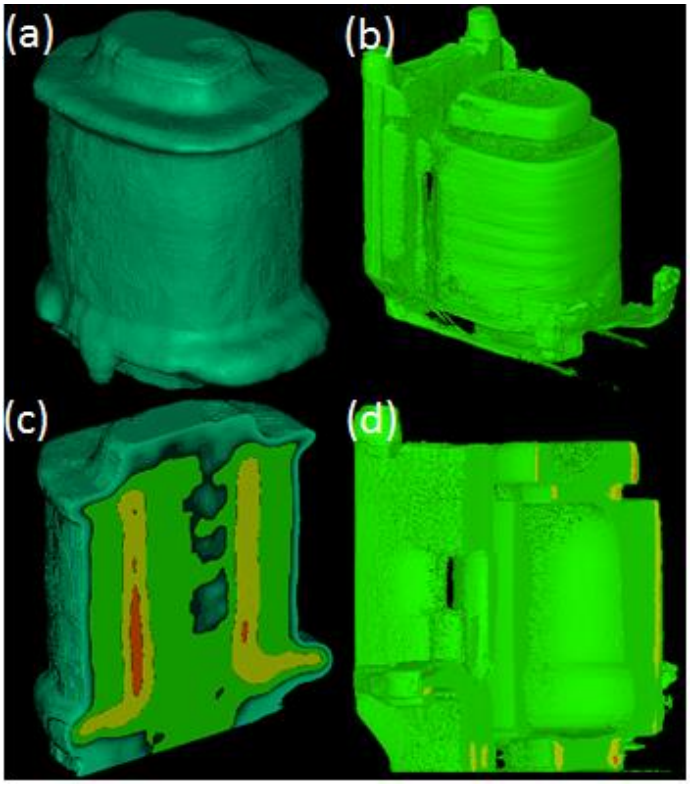


Figure 3.21. 3D Isometric Images with Volume Rendering, (a) Neutron Image of Part of a Power Relay Switch (b) X-ray Image of Part of Power Relay Switch (c) Cross-sectional Neutron Image of a Power Relay Switch, (d) Cross-sectional X-ray Image of a Power Relay Switch

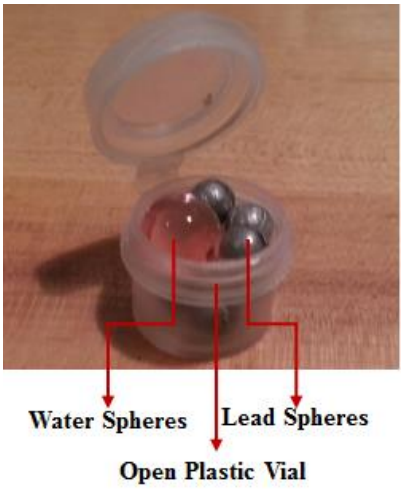


Figure 3.22. Photograph of Phantom Representing Low and High Atomic Number Materials

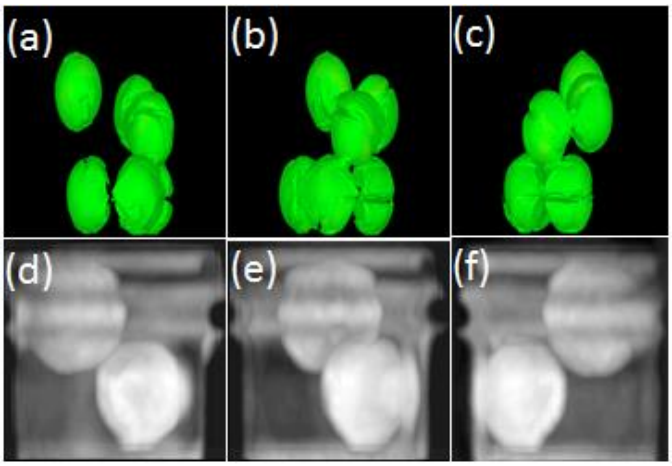


Figure 3.23. 3D Images of a Phantom at Different Angles, (a)-(c) 3D X-ray Images at 45, 90 and 180 Degrees, (d)-(f) 3D Neutron Images at 45, 90 and 180 Degrees

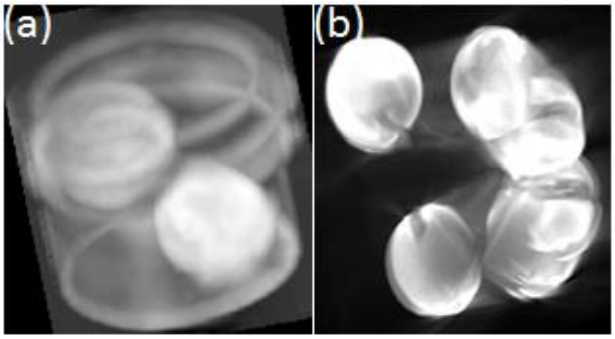


Figure 3.24. 3D Isometric View of Phantom (a) Neutron Image Showing plastic Vial and Water Balls, (b) X-ray Image Showing Only Lead Spheres

## 3.8. DISCUSSION

The NXCT system is useful for certain applications and will facilitate existing nondestructive testing methods. The newly built NXCT imaging system is optimal for the imaging of small to medium sized objects between 0.5 mm and 50 mm. Due to careful optimization and calibration of the imaging system, the sample positioning device's travel distances in the X, Y and Z directions does not obstruct the beam geometries, and also

optimizes the field of view for the both modalities. For future imaging requirements, the field of view may be increased. Furthermore, computed tomography and image fusion applications require faster algorithms to reconstruct the 3D data and to allow instant image fusion. It is also notable that the acquisition time should match for both neutron and x-ray sensors to allow for convenient NXCT operation. The high contrast imaging objects for neutrons and x-ray imaging will result in shorter image acquisition time which will eventually help to synchronize the frame rate for both sensors. Moreover, different detector technologies and readout circuits could result in different spatial and temporal resolution, sensitivity, dynamic range and image acquisition time. Neutron and x-ray sources could have different intensity values and geometrical features that will play a vital role in overall imaging process. It is important to note that the beam intensity, geometrical factors and readout circuits are all main contributing factors for image quality and overall synchronization of the NXCT system.

## 3.9. CONCLUSION

An imaging system incorporating both neutron and x-ray modality has been created for the non-destructive analysis of materials for research and academia purposes. The interactions that neutrons and x-rays have with materials are characteristically unique, causing distinct image production. Images with poor resolution due to severe or poor radiation attenuation may be improved by fusion with another imaging method. For example, isotopes of the same element will be indiscernible using x-ray imaging because of the identical atomic number, but can be identified by neutron imaging because of the difference in nuclear cross section. Combining these two imaging techniques should

provide for enhanced structural and compositional information of certain imaging object. The newly developed NXCT system could serve as a standardized tool for nondestructive evaluation of many applications.

# 4. PERFORMANCE EVALUATION OF A NEUTRON AND X-RAY COMBINED COMPUTED TOMOGRAPHY SYSTEM

## 4.1. INTRODUCTION

Neutron and X-ray imaging are widely employed imaging techniques [1- 44] in research, industry, and the medical field. Utilizing the advantages of both neutron and X-ray imaging techniques, which are complementary by nature, a novel combined neutron and X-ray (NXCT) imaging system has been developed at the Missouri University of Science and Technology Reactor (MSTR) [17] The capability of the new imaging system is based on image quality and the associated parameters i.e. contrast, noise and resolution [5]. Most of the developed methods such as Modulation Transfer Function, Noise Power Spectrum, and Detective Quantum Efficiency (MTF, NPS and DQE) are used to quantify the parameters and are accepted as the standard methods for imaging system performance evaluation. The MTF measurement evaluates the spatial resolution of the imaging system. It measures the ability of the imaging detector to characterize a radiation pattern whose intensity varies sinusoidally in a one dimensional plane for a corresponding distance. MTF can be calculated by the slit method, square wave method, sine wave method, sine wave response method, or the edge method [45-58]. The noise power spectrum (NPS) characterizes the image noise and the shape of the spectrum determines the frequency space where the noise power is concentrated. DQE is a measurement of the imaging system efficiency. In fact, DQE collectively evaluate the signal and noise performance of the imaging system. In short, DQE provides a collective description of the noise transfer characteristics of a detector which shows how the signal is degraded by passing through the imaging system and provides a measure that how well an imaging

system can detect minute detail in an image. The performance evaluation parameters are well established and are frequently applied in the quantification of an X-ray imaging system's performance [45-58].

However, the newly developed neutron and X-ray combined imaging system requires a uniform quantification procedure that can be easily implemented for the performance evaluation of current combined imaging systems. Physical and geometrical characteristics of radiation sources and imaging detectors play a substantial part in developing performance evaluation criterions. In neutron radiography [25-28], ASTM Image Quality Indicators (IQI) are common standards used to characterize the neutron image quality as well as the beam purity. However, the neutron imaging industry is constantly enhancing digital imaging techniques and needs a new set of standards which can be easily applied [59-63]. There are no ASTM standards available for digital neutron imaging. The use of new standards will help to quantify the performance of the combined imaging system. This will also help to optimize the image quality of the imaging system. The radiation sources and imaging detectors for neutron and X-ray imaging modules have different physical and geometrical characteristics. Furthermore, nuclear reactor neutron sources could have a fluctuating flux behavior at the beam port due to factors such as the thermal neutron population and similar behavior from other precursors at a certain time. This flux trends are not present in X-ray sources. Finally, the above mentioned factors are pertinent in the performance evaluation as well as optimization of the combined imaging system performance.

## 4.2. MATERIALS AND METHODS

The MTF value for the X-ray and neutron imaging module was obtained using the knife edge method. To obtain a perfect knife edge, an optically polished Tungsten edge phantom (see Fig. 4.1) was used for the X-ray imaging module and a highly polished Cadmium edge phantom was used for the neutron imaging module. There are well developed methods [35-47] available to calculate the pre-sampled MTF, NPS, and DQE. Similarly, to calculate the NPS of the X-ray imaging module, an image of a solid water phantom (see Fig. 4.1) was used to calculate the noise amplitude.

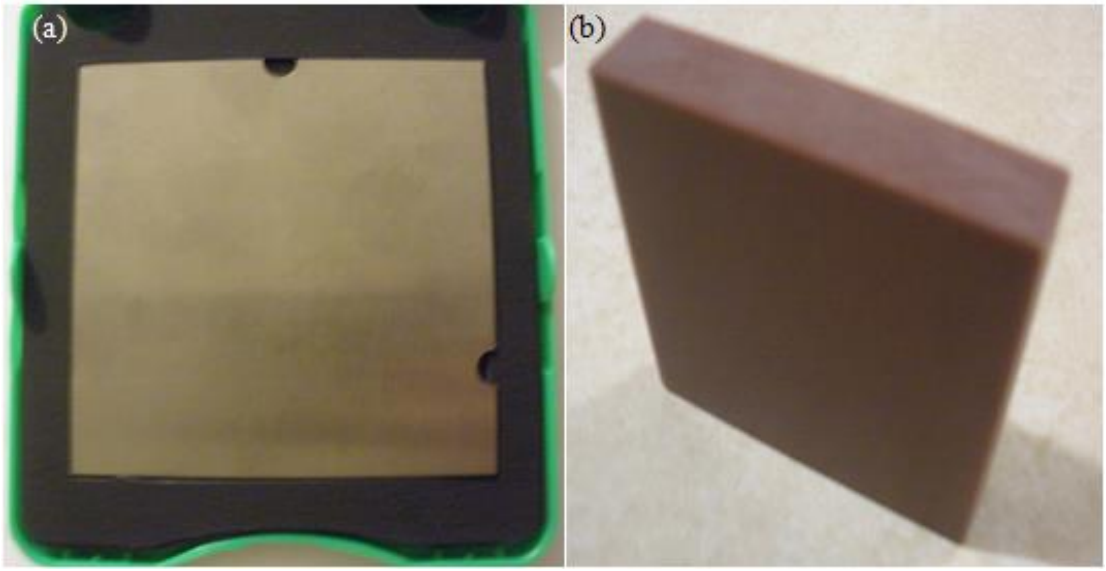


Figure 4.1. A Highly Polished (a) Tungsten Edge Phantom with Two Adjacent Polished Edges Inside a Protective Box and (b) a Solid Water Phantom

**4.2.1. Non-Linearity Correction of the MCP Neutron Imaging Detector.** The neutron detector readout requires a non-linearity correction. The delay line readout was calibrated using a pin-hole mask phantom. The images from pin hole mask were acquired using a UV pen ray lamp (Output power density: 4.5 $mW/cm^2$, wavelength: 253.7 nm) and then were later corrected using a non-linearity algorithm. In this experiment, a mask with a known hole-pattern (1mm center to center spacing) was mounted on the detector window and an image was taken. From this image, the noise and background were removed, leaving only the peaks from the pinhole mask. The algorithm analyzes the flat field corrected mask image and compares the actual peak location with their expected location. It then creates a correction table for the anode to correct for any non-linearity in the anode (see Fig. 4.2). In fact, the algorithm calculates the "center of mass" of the holes and corrects for any discrepancies. The algorithm was provided by Roentdek Handels Gmbh which provided the customized software named “COBOLD PC” for the operation of the MCP detector. The algorithm can be effectively incorporated in the dynamic link library of the software program and can be applied for active corrections during the image acquisition process. In order to verify the non-linearity corrections, UV and neutron imaging was performed on the corresponding phantoms and the results were compared. For the UV imaging, a fine machined phantom was exposed for a few minutes on the detector window and images were obtained (see Fig. 4.3). Similarly, to verify the corrections on neutron imaging, neutron images of a perforated cadmium strip were taken and analyzed for its non-linearity (see Fig. 4.4). It is evident from the non-linearity corrected images that the algorithm accurately corrected the non-linearity behavior of the delay line anode readout and improved the image linearity.

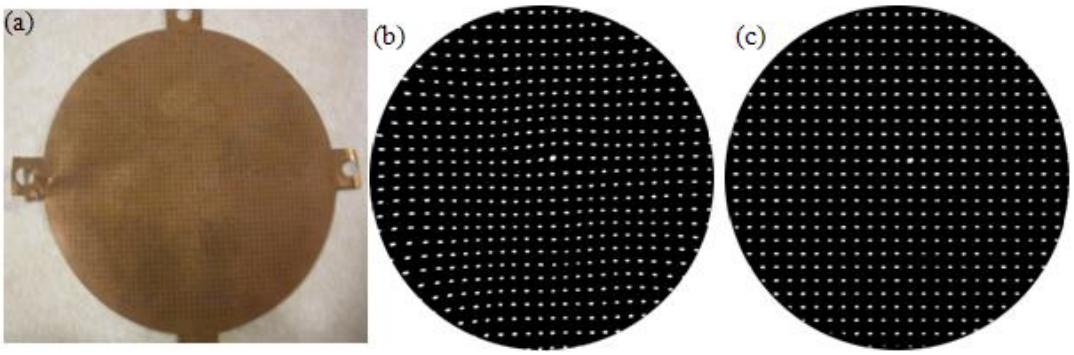


Figure 4.2. Photograph of the Pin-hole Mask (a), Non Linear Image of the Pin-hole Mask from UV Imaging (b), Non Linearity Corrected Image of the Pin-hole Mask (c)

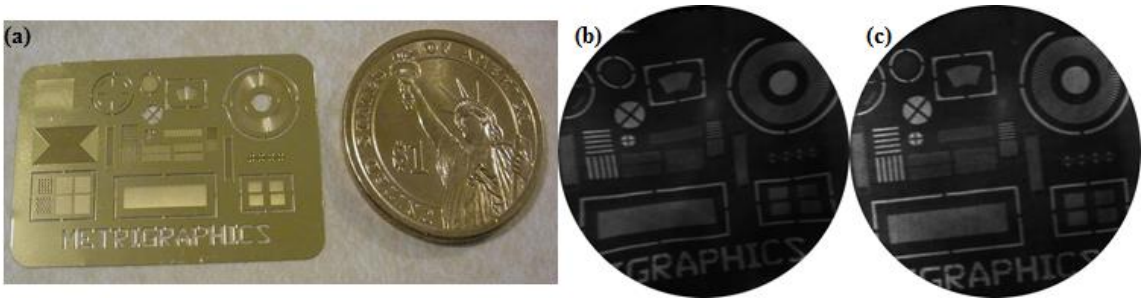


Figure 4.3. Photograph of the Electroformed Phantom and $1 Coin for Scale (a), Non Linear Image of the Electroformed Phantom from UV Imaging (b) and Non Linearity Corrected Image of the Electroformed Phantom (c)

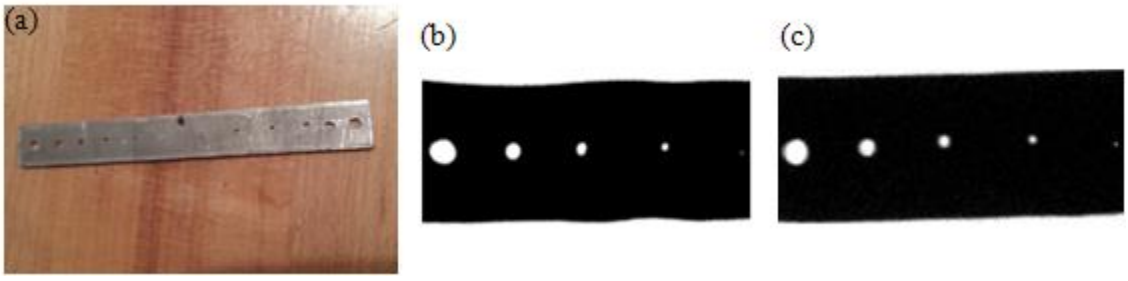


Figure 4.4. Neutron Image of Perforated Cadmium Strip with Smallest Visible Hole Size of 0.25 mm

**4.2.2. Flux Trend at the MCP Neutron Imaging Detector.** The second step was to verify the MCP detector response to the flux from the beam port. To do this the reactor was operated at full power (200 kW) and the images were acquired at different timing intervals between one and nine minutes while maintaining consistent detection geometry. The display counts were recorded and plotted against respective timings (see Fig. 4.5). It is clear from the plotted graph that "Total no. of Counts" Vs. "Time" shows a linear trend which indicates both a constant flux behavior from the beam port and a uniform response of the MCP detector. The $R^2$ value of 0.99 confirms the linear flux trend at the MCP neutron detector. A small fluctuation in the linearity accounts for the fluctuating thermal neutron population in the form of stochastic radiation trend at the beam port.

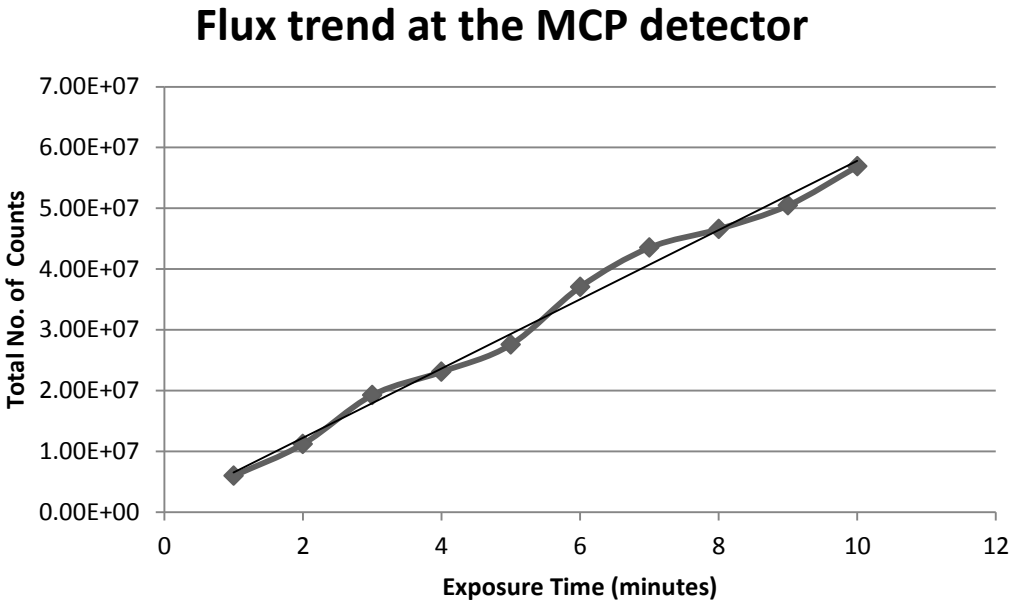


Figure 4.5. Plotted Graph of Total Number of Counts vs. Exposure Time

### 4.3. CALCULATION OF MTF, NPS AND DQE

The MTF, NPS and DQE of the neutron/X-ray imaging module were determined using a standard computation method described by previous research groups [45-57, 62-63]. The main steps to calculate the MTF, NPS and DQE are shown by the schematics (see Fig. 4.6, 4.7 and 4.8, respectively). Furthermore, the MTF was obtained using the edge method (see Fig. 4.9 and 4.10). To verify the MTF measurement (see Fig. 4.11), a resolution test pattern (Leeds test object of type 53, lead thickness of 0.05 mm, line pair from 0.5 – 10 lp/mm) was used. From X-ray image of test pattern, group 18 of resolution test pattern can be viewed. This corresponds to MTF resolution of 8.5 lp/mm at spatial frequency of 10%. The NPS was also calculated. The decreasing NPS trend which approaches a constant value at high frequencies can be seen from the graph (see Fig. 4.12, 4.13) which is confirmed in previous works [45-57, 64]. The results of the MTF and NPS were used to calculate the DQE of the X-ray imaging module. The photon flux spectrum was simulated by SpekCalc software (see Fig. 4.14) and the DQE equation [62] was normalized by considering power and exposure time for this particular experiment (Voltage: 75 kV, Current: 2 mA and Exposure time: 500 ms) for the corresponding beam geometry. The DQE value of 0.53 was obtained for the present experimental set-up which is in the range of 0.1-0.7 found for other X-ray imaging systems. Similarly, the MTF for neutron imaging module was also calculated using the edge method (see Fig. 4.10). The equation described by Lewandowski et al. was used to obtain the DQE (see Fig. 4.15, 4.16) [62, 63] of the neutron imaging module. The neutron flux mapping experiments were used to find the value of incident quantum for DQE computation of neutron imaging module. The NPS spectrum (see Fig. 4.7 and 4.13) of neutron imaging

module was also calculated by the same algorithm that was used to calculate the NPS of the X-ray imaging module. However, in this experiment, no phantom was used to obtain the noise image. In fact, in neutron imaging, there is no need to account for scattering caused by the patient and it is assumed that the scattered neutrons reaching the detector will be sufficient to contribute to the noise image. Therefore, only flat field images were used for calculating the noise power spectrum and plotted for corresponding spatial frequencies. The NPS curve (see Fig. 4.13) in the neutron imaging module shows the concentration of noise at different frequency intervals. It is clear from the graph (see Fig. 4.13) that NPS initially decreases at increasing spatial frequencies and then exhibits nearly a constant behavior at higher frequencies.

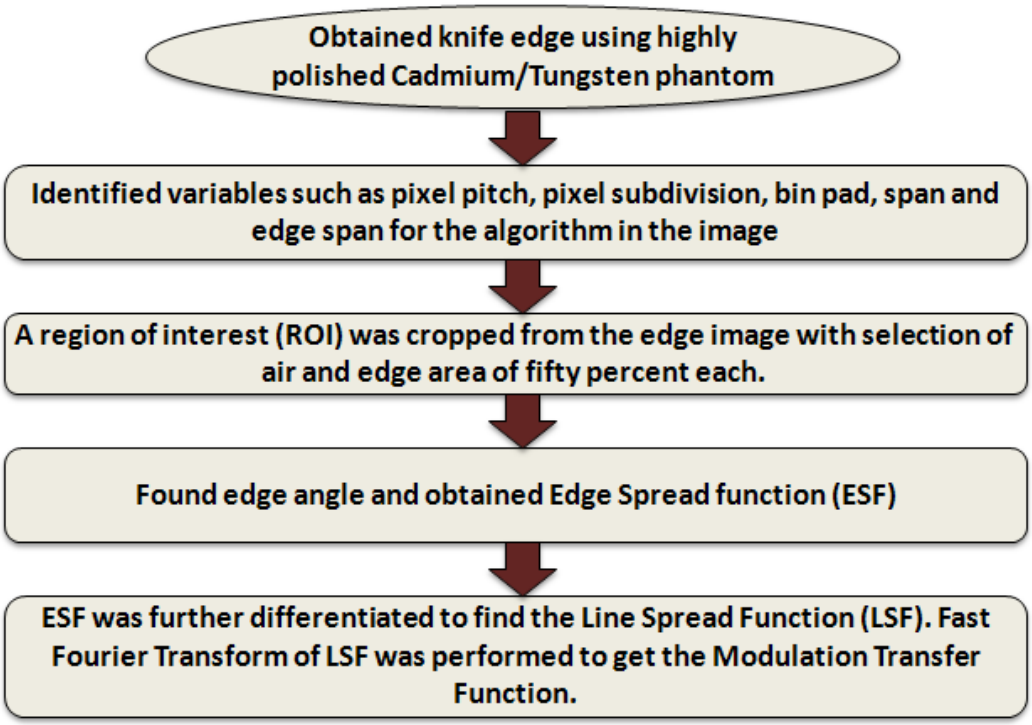


Figure 4.6. Method of Obtaining Modulation Transfer Function (MTF)

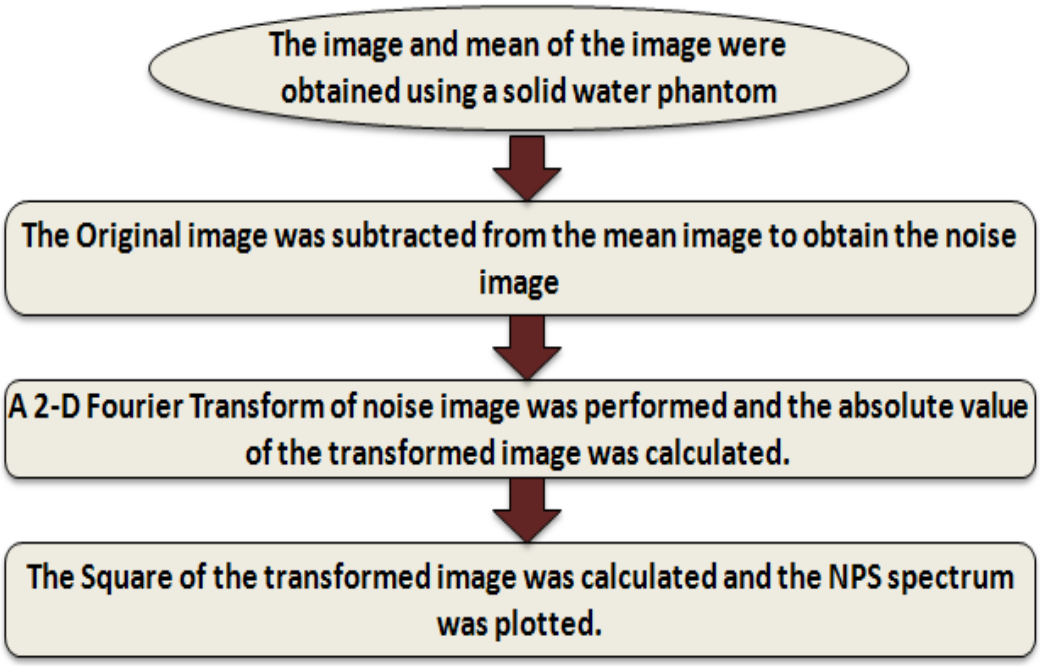


Figure 4.7. Method of Obtaining Noise Power Spectrum (NPS)

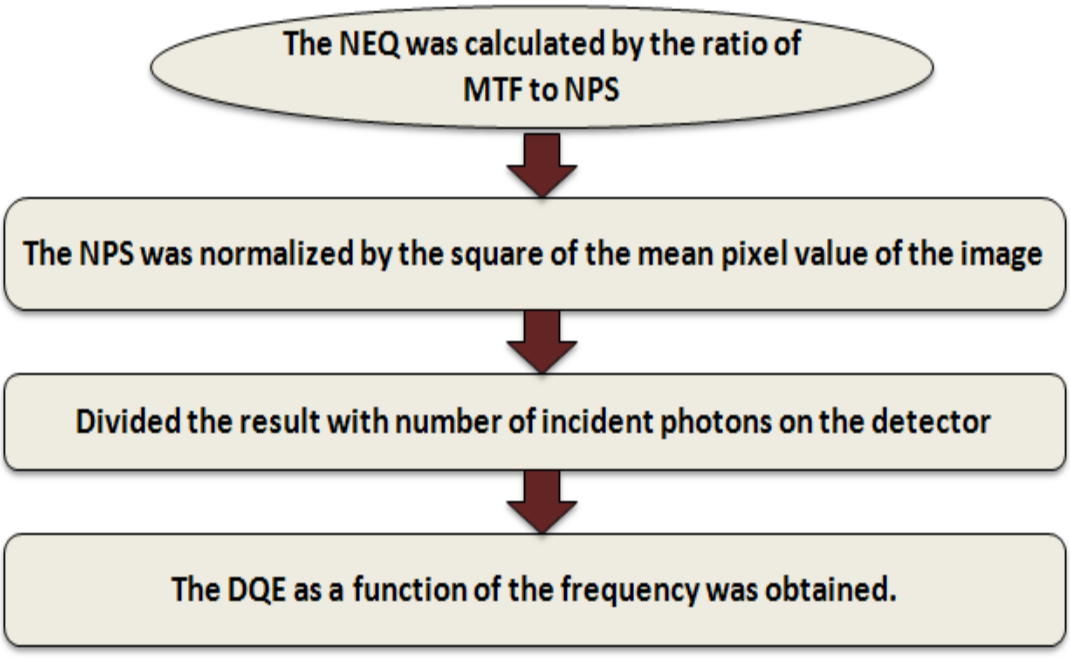


Figure 4.8. Method of Obtaining Detective Quantum Efficiency

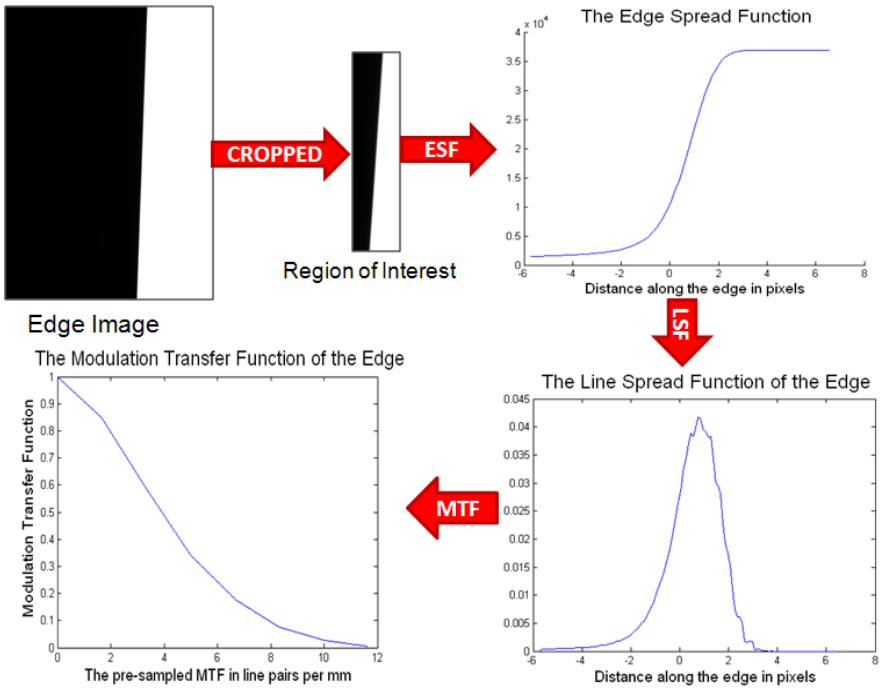


Figure 4.9. Measurement of Modulation Transfer Function for X-ray Imaging Module

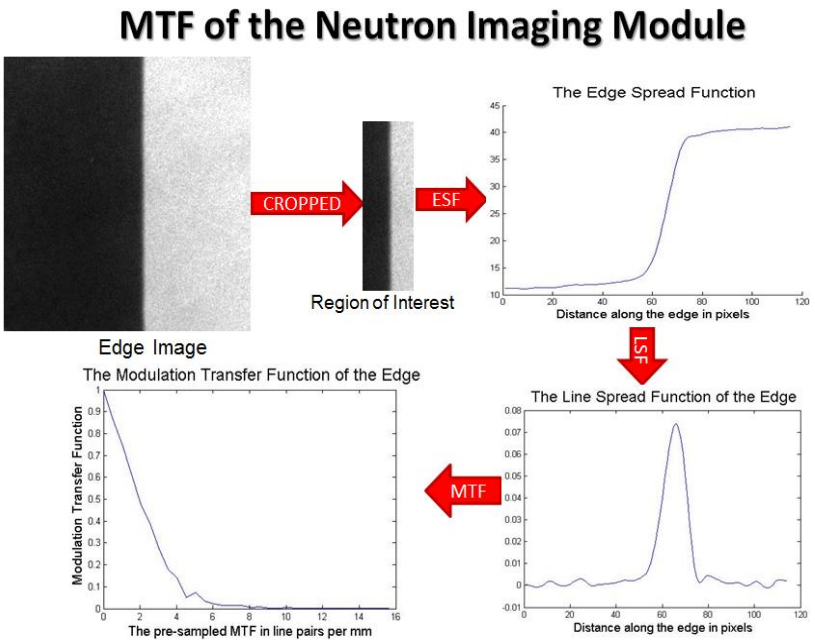


Figure 4.10. Measurement of Modulation Transfer Function for Neutron Imaging Module

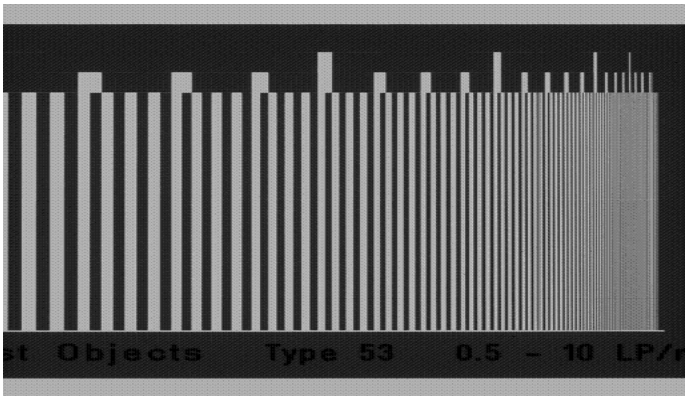


Figure 4.11. An X-ray Image of Resolution Test Pattern

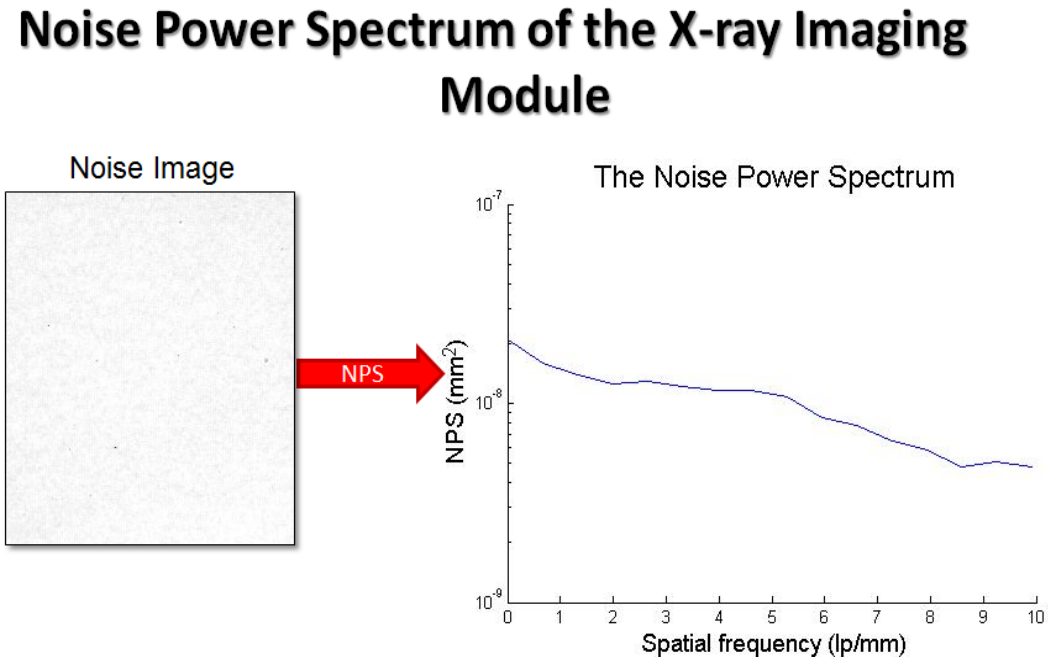


Figure 4.12. Noise Power Spectrum of the X-ray Imaging Module

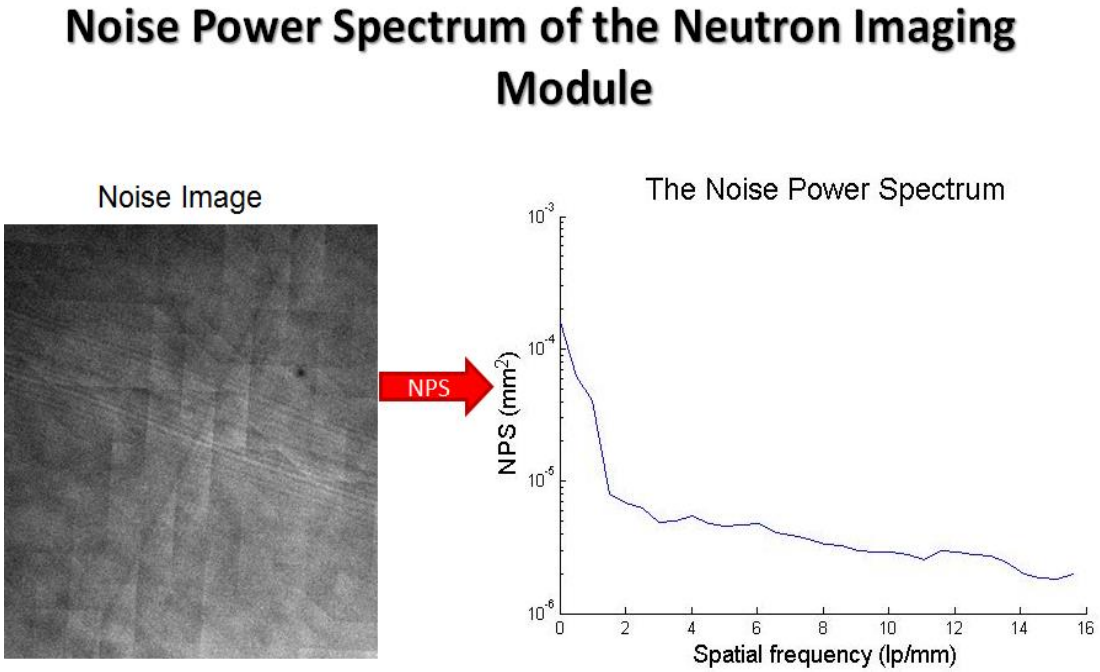


Figure 4.13. Noise Power Spectrum of the Neutron Imaging Module

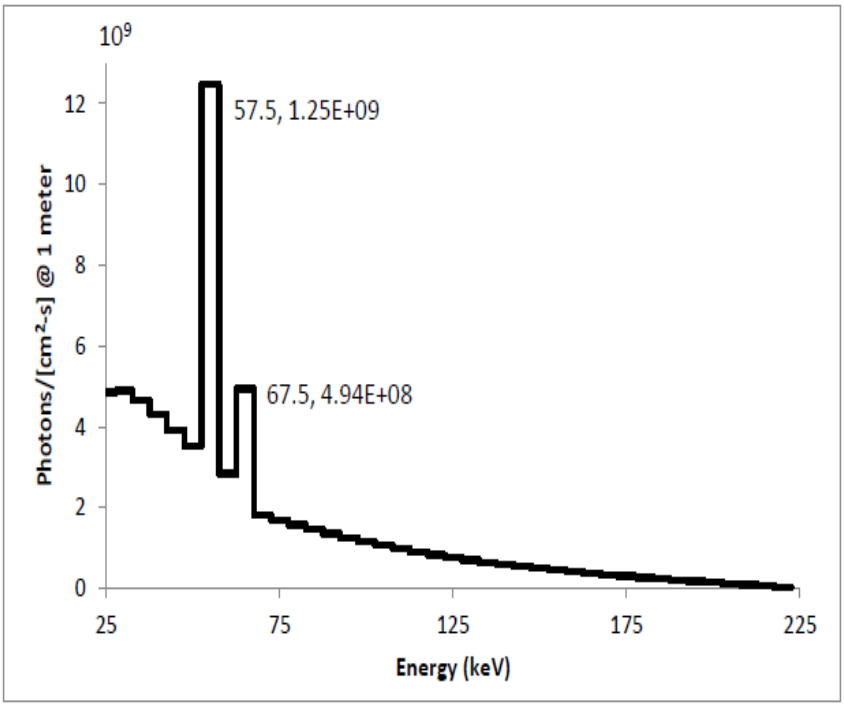


Figure 4.14. Full Photon Flux Spectrum of the X-ray Imaging Module

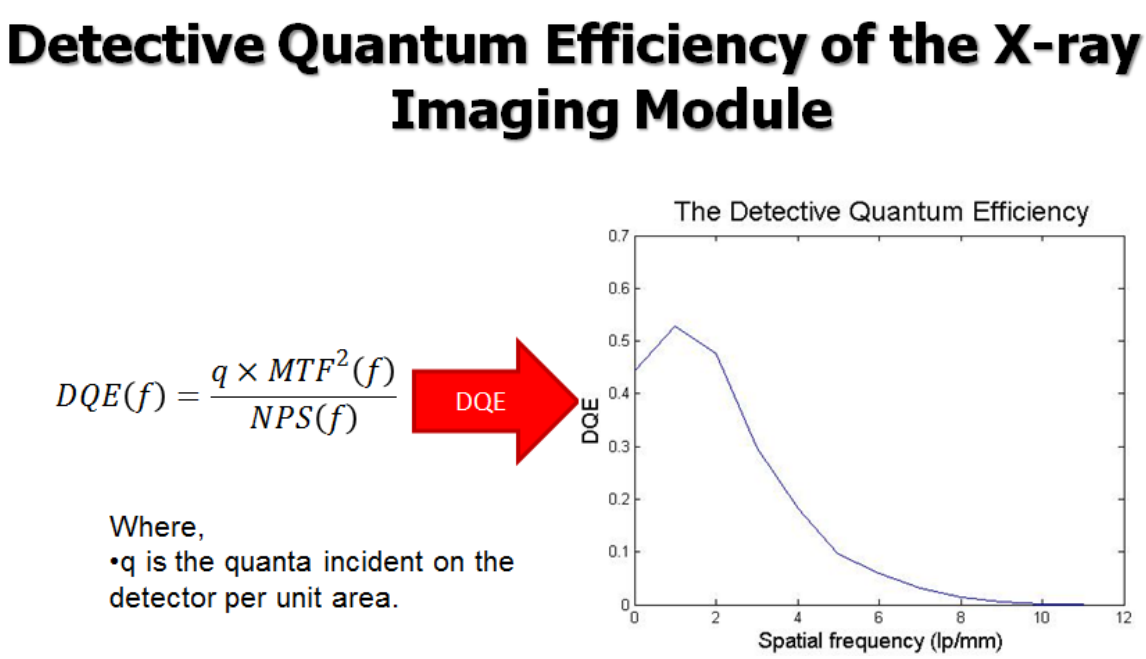


Figure 4.15. Detective Quantum Efficiency of the X-ray Imaging Module

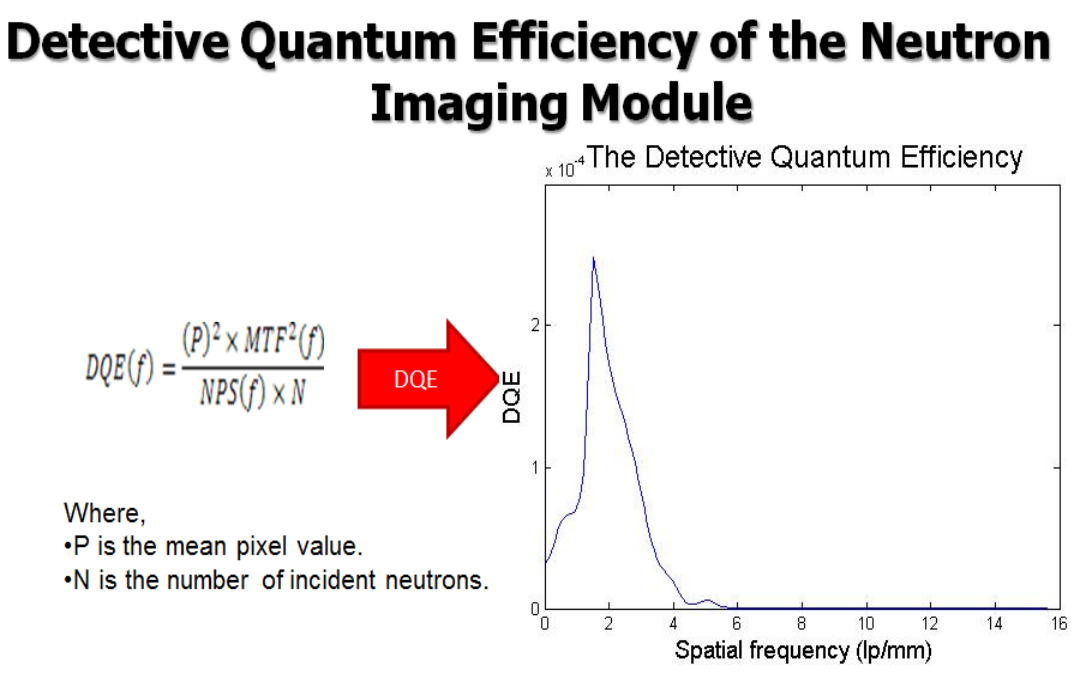


Figure 4.16. Detective Quantum Efficiency of Neutron Imaging Module

## 4.4. DISCUSSION AND CONCLUSION

The MTF, NPS, DQE methods and resolution test patterns can be used to evaluate the performance of any imaging system. In X-ray imaging module, the spatial frequency at 10% of the MTF was determined to be 8 lp/mm (found using the edge method), while the MTF value determined from the evaluation of the resolution test pattern is 8.5 lp/mm. This confirms the consistency in MTF measurements for X-ray imaging module. The MTF value between 8 and 8.5 lp/mm suggests that spatial resolution of X-ray imaging module is between 58.8 and 62.5 μm. The neutron imaging module, with the spatial frequency at 10% of the MTF was determined to be at least 4.3 lp/mm which corresponds to spatial resolution of 116.3 μm. The trends for the MTF, NPS and DQE were evaluated for the X-ray and neutron imaging module. The DQE of the X-ray imaging system is 0.53 which agrees with the trend of other X-ray imaging systems where DQE usually lies in the range of 0.1 to 0.7 [50-52]. Similarly, the DQE value of the neutron imaging module is $2.5 \times 10^{-4}$, which is in agreement with the value reported by Lewandowski et al. for neutron imaging system. Since, intensity of incident neutron quanta in neutron imaging module is considerably lower than that of a photon quanta of the X-ray imaging module. The lower DQE value of $2.5 \times 10^{-4}$ of the neutron imaging module can also be accounted for the following reasons: (1) the higher fast neutron content in the neutron beam resulted in stochastic noise at corresponding spatial frequencies, (2) lower and non-uniform neutron flux intensity at the neutron imaging detector, (3) considerable background noise and (4) signal loss due to the detector electronics.

The geometrical non-linearity correction of the delay line anode readout of the MCP neutron detector was also performed and shown by the corrected images. The NPS

trend for neutron imaging module was also completed. The smallest fabricated hole (250 μm) on the perforated cadmium strip is visible in neutron images (786 x 786 pixel). The calculation of MTF for neutron imaging module is gaining acceptance [59-63] to describe the image quality of the neutron imaging system but using DQE as a standard for neutron image quality measurement is a new approach. Moreover, using DQE as an image quality standard in neutron imaging helps to identify contribution of noise characteristics in better detail for evaluating the overall image quality.

A pure thermal neutron beam with uniform flux intensity and higher neutron flux ($\geq 10^9$ neutrons/cm$^2$-sec) will increase the system sensitivity and resulting resolution of the neutron imaging module. Based on the present results, physical parameters such as beam geometry and neutron flux of the experimental set-up should be further investigated. The MCP neutron detector has a delay line anode readout which involves careful optimization of constant fraction discriminator, thresholds, frequency amplifiers and power supply voltages which will eventually contribute to the spatial resolution of the overall neutron imaging module. A new basis for performance evaluation standards can be made from these findings which can be effectively applied toward performance evaluation of a new type of combined neutron and X-ray digital imaging system.

# 5. IMAGE FUSION & FEASIBILITY STUDIES ON EXPLOSIVE DETECTION AND HOMELAND SECURITY APPLICATIONS

## 5.1. INTRODUCTION

The successful creation and operation of a neutron and X-ray combined computed tomography (NXCT) system has been demonstrated in earlier sections. The NXCT system has numerous applications in the field of material characterization and object identification in materials with a mixture of atomic numbers represented. In this section, the feasibility studies have been performed for explosive detection and homeland security applications, particularly in concealed material detection and determination of the light atomic number materials. These materials cannot be detected using traditional X-ray imaging. The NXCT system has the capability to provide complete structural and compositional information due to the complementary nature of X-ray and neutron interactions with materials. The design of the NXCT system facilitates simultaneous and instantaneous imaging operation, promising enhanced detection capabilities of explosive materials, low atomic number materials and illicit materials for homeland security applications. In addition, a sample positioning system allowing the user to remotely and automatically manipulate the sample makes the system viable for commercial applications. Several explosives and weapon simulants have been imaged and the results are provided. The fusion algorithms which combine the data from the neutron and X-ray imaging produce superior images. This section is a compete overview of the NXCT system for feasibility studies of explosive detection and homeland security applications. In this section, feasibility studies on explosive detection, algorithm development for image fusion, and detection schemes are provided.

## 5.2. FEASIBILITY STUDIES ON EXPLOSIVE DETECTION

The use of X-rays for inspection of airport baggage, cargo containers and other similar uses are well established techniques. However, increased demand for terrorist threat reduction and the need for increased security requirements required new technologies for instant and thorough inspection for similar applications. The detection of special nuclear material, explosives, and thorough inspection of cargo containers are much researched [65-67]. Several research groups have contributed notable development to improve the current technology which is partially or completely utilized in real time applications. The use of high energy X-rays, backscatter X-rays and nuclear car wash are example of new technologies [40-44, 66]. Current detection technologies can be broadly classified into active and passive detection techniques which are detailed [65-67] (see Fig. 5.1) in the literature. However, these technologies are limited in scope and cannot provide complete information in certain cases. X-ray or neutron inspection of a shielded object alone may exhibit shortcomings in the accurate detection of concealed objects [40-42, 44].

However, using neutron and X-ray detection at the same time can be useful to overcome such situations. Utilizing the advantages of both neutron and X-ray imaging techniques, which can be made complementary, a novel combined neutron and X-ray (NXCT) imaging system has been developed at the Missouri University of Science and Technology Reactor (MSTR). The NXCT system can be useful in such scenarios to detect explosives, special nuclear material, and other illicit materials. The conceptual design (see Fig. 5.2) of the NXCT facilitates a realistic design to perform neutron and X-ray imaging at the same time. In addition, three dimensional reconstruction of imaging

data will ensure the accurate detection in complicated geometries. This is the first development of an NXCT imaging system, and it can be effectively applied in different configurations of image sensors and radiation sources. Fusion algorithms are an important component which combines comprehensive data of imaging objects and can be optimized for target homeland security applications.

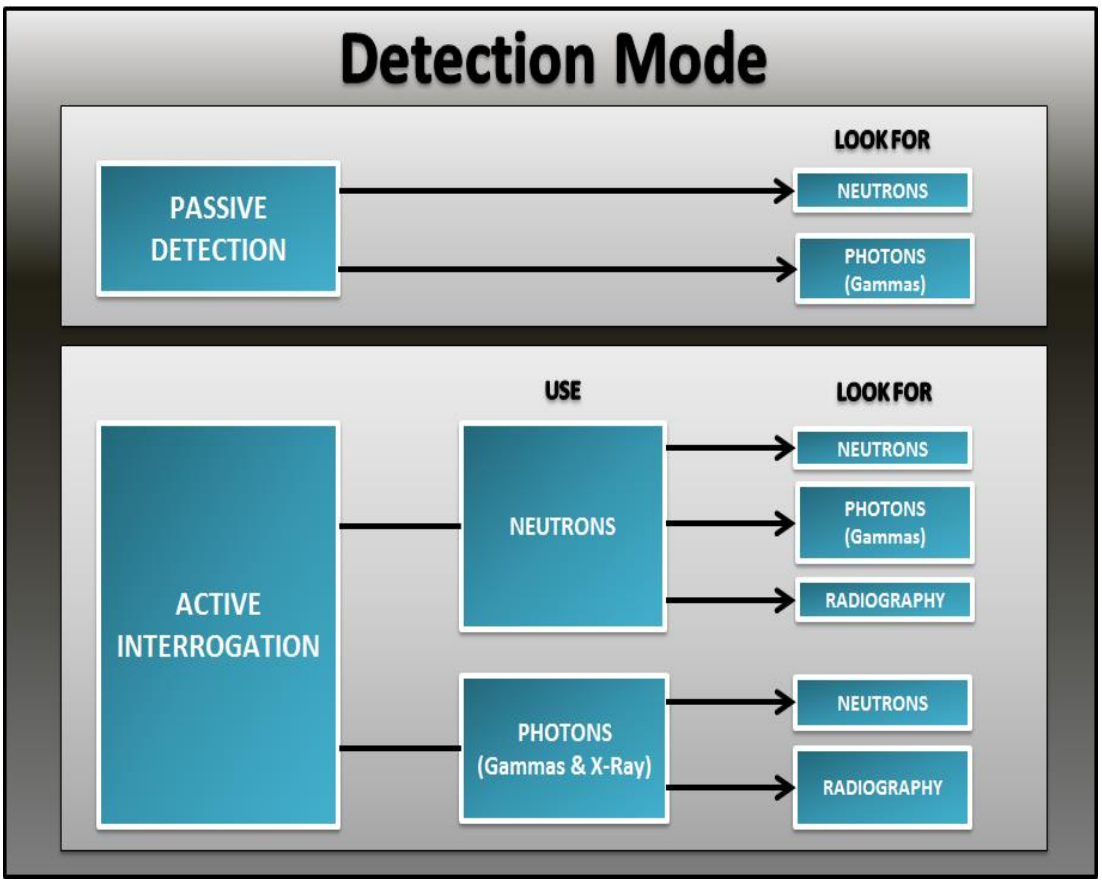


Figure 5.1. Schematic of Different Detection Schemes

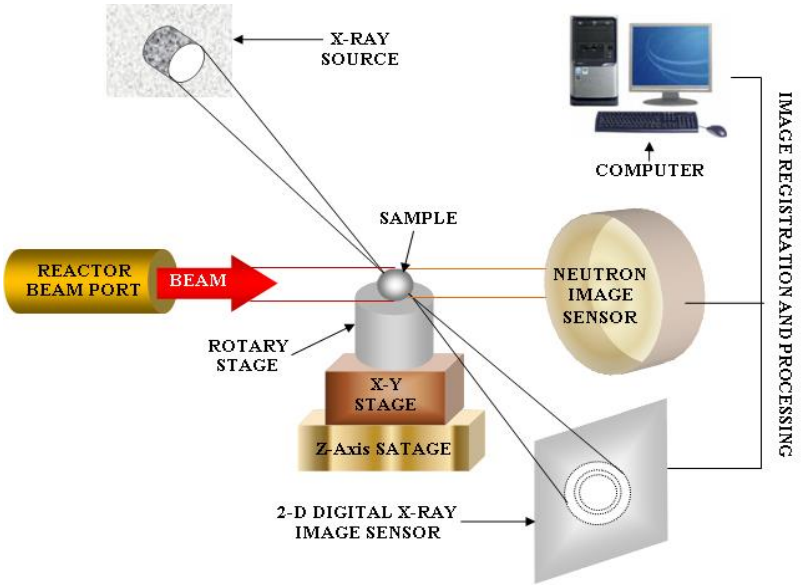


Figure 5.2. Conceptual Design of the NXCT System

A series of phantoms were prepared based on structural, compositional, and attenuation characteristics to demonstrate the utility of the NXCT system for the explosives, low atomic number material and concealed material detection. The NXCT imaging was performed for a power relay switch to show the detection of low and high atomic number materials in an imaging object using neutron and X-ray imaging, respectively (see Fig. 5.3). The purpose of conducting combined imaging experiment using the above object was to show the importance of the NXCT system in terms of material characterization. Further, explosive simulants of dynamite, nitrocellulose and TNT were selected. The combined imaging was performed at 0.0253 eV for neutrons and 85 kV/1.5 mA for X-rays (see Fig. 5.4). The X-ray image was unable to image the nitrocellulose. Similarly, X-ray imaging of dynamite and TNT also produced low contrast images. Conversely, in the neutron image, all of the above explosive simulants are clearly

visible and provides better contrast. Neutron imaging has the ability to detect low atomic number materials, including typical explosive materials. One immediately obvious application would be during the scanning of airport baggage and cargo containers, especially lead-covered items that conceal plastic weapons or explosive materials More importantly, low energy X-rays, and CZT-based multi-energy X-ray detectors [40-44] may not be a viable option for detecting plastics or explosives covered with a thick lead material. A combined NXCT system holds better prospects for security applications. The interactions that neutrons and X-rays have with materials are characteristically different, causing distinct image production in each case. Images with poor contrast, due to severe or poor radiation attenuation, may be improved and can be effectively detected through the fusion of another imaging method. For example, isotopes of the same element will be indiscernible using X-ray imaging because of the identical atomic number (same electron structure), but can be identified by neutron imaging because of difference in nuclear cross sections. Combining these two imaging techniques should provide enhanced structural and compositional information about certain imaged objects, and superior detection of concealed explosives and low atomic number materials.

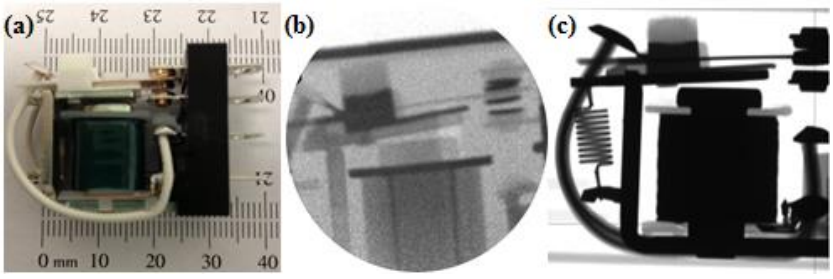


Figure 5.3. Photograph of a Power Relay (a), Neutron Image of a Power Relay (b), X-ray Image of a Power Relay (c)

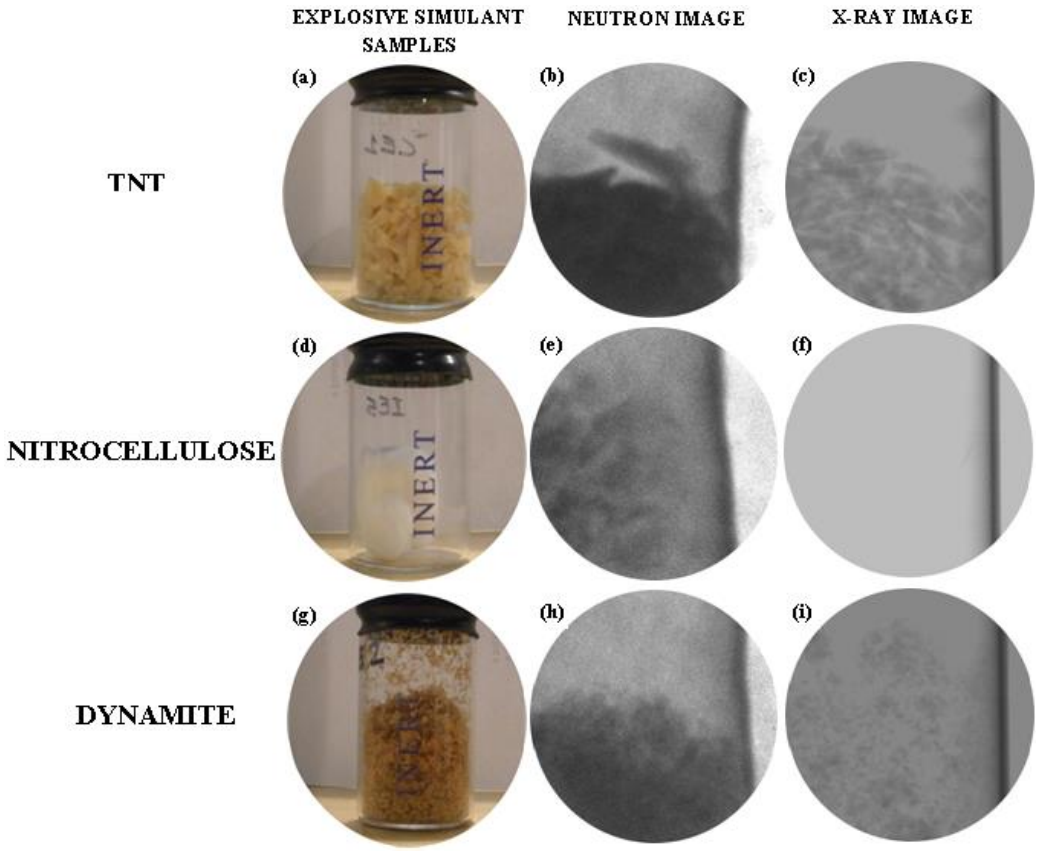


Figure 5.4. Neutron and X-ray Images of Explosive Simulants

## 5.3. DESCRIPTION OF IMAGE FUSION

In order to demonstrate the utility of fusion of X-ray and neutron imaging, a phantom was simulated with a mixture of atomic number materials represented (see Fig. 5.5). In order to simulate neutron and X-ray images, imaging physics together with reasonable assumptions were used. The simulated neutron and X-ray images were then fused [68, 69] together by multiplier fusion (see Fig. 5.6) and discrete wavelet based fusion (see Fig. 5.7) algorithms to extract the complete information. The details of the

fusion algorithms and their results are detailed (see Fig. 5.8-5.10). It is evident from the fused images that both algorithms are able to provide complete material information. However, fusion algorithm based on multiplier fusion provides better contrast than discrete wavelet based fusion algorithm (see Fig. 5.9, 5.10).

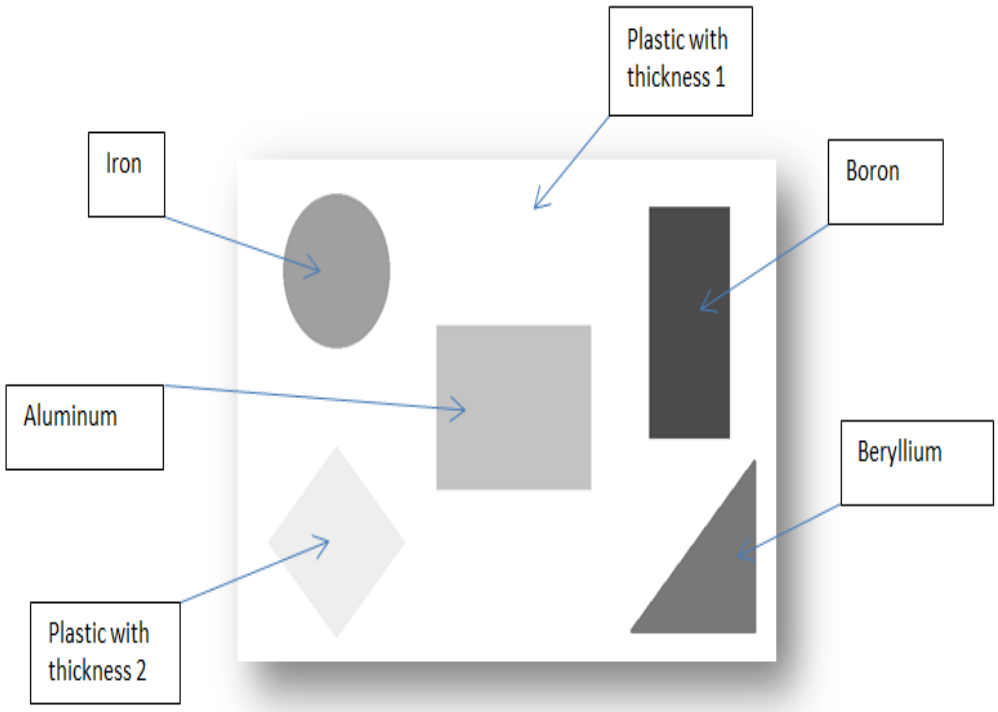


Figure 5.5. Simulated Phantom with Different Materials

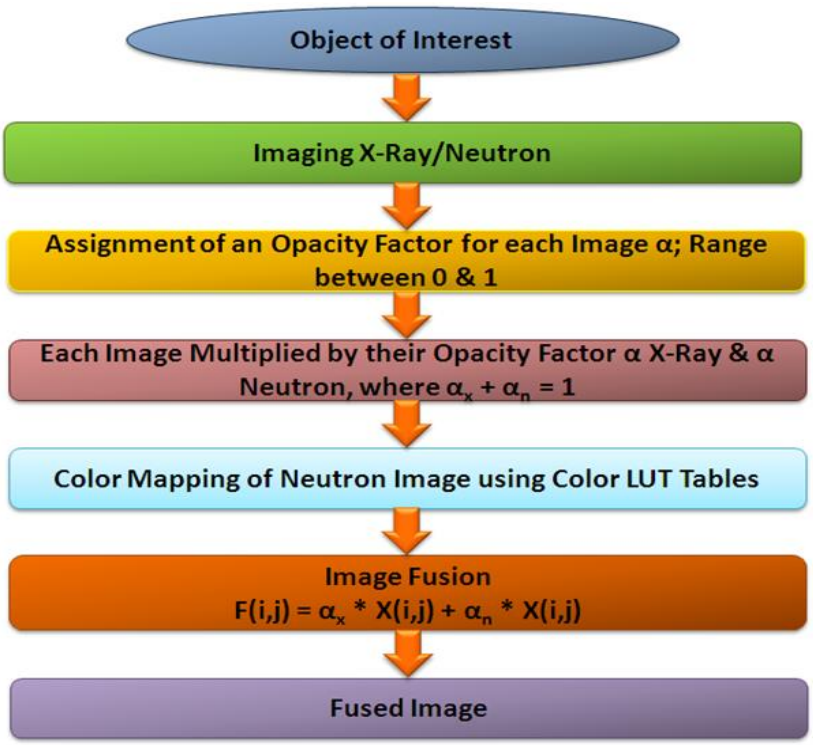


Figure 5.6. Multiplier Fusion Algorithm

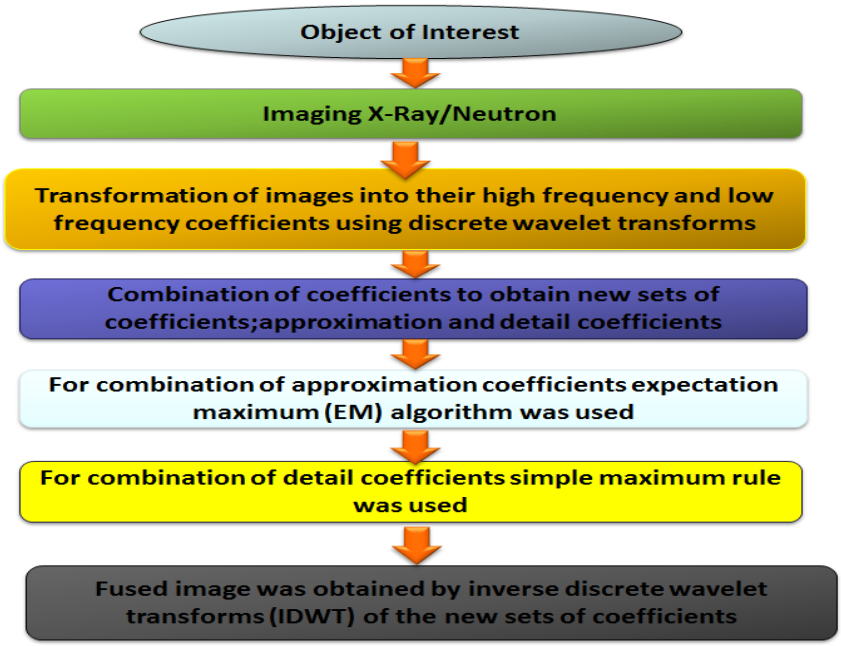


Figure 5.7. Wavelet Fusion Algorithm

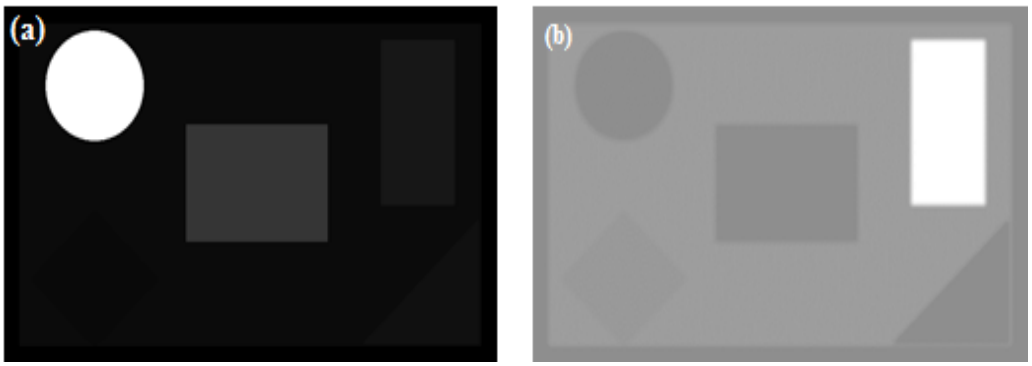


Figure 5.8. Simulated X-ray and Neutron Image

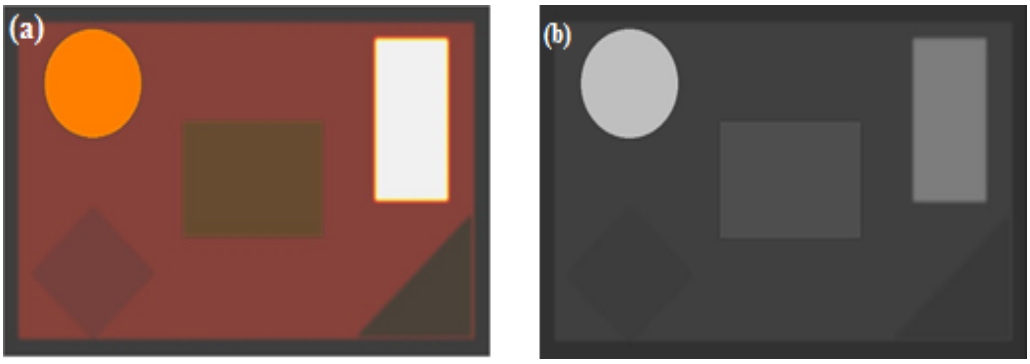


Figure 5.9. Image Fusion by Multiplier Algorithm and Discrete Wavelet Algorithm

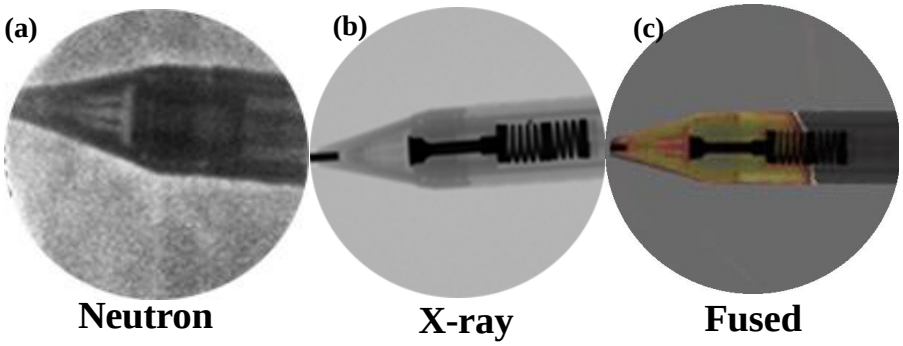


Figure 5.10. The Plastic Parts of a Mechanical Pencil Image are Visible in the Neutron Image while the Metal Parts are Visible in the X-ray Image. The Fused Neutron and X-ray Image of the Mechanical Pencil Retains both Structural Information

# 6. DISCUSSION AND CONCLUSION

The concept of combining neutron and X-ray imaging can be useful in terms of extracting complimentary information from objects of interest, but may exhibit shortfalls for certain applications (see Table. 6.1).

Table 6.1 Pros and Cons of a Neutron/X-Ray Combined Computed Tomography System

| Pros | Cons |
|---|---|
| A comprehensive image of a certain object is possible. | It might not be necessary for a few objects. |
| The concept of NXCT can be extremely useful for all energy ranges of a neutron/X-ray imaging system. | The current NXCT system is limited to a certain energy range (0.0253 eV for neutrons and 0-225 kV for X-rays). |
| Instant and combined neutron and X-ray imaging is possible. | Objects may become highly radioactive during the image acquisition process because of neutron activation. |
| Accuracy of calibration for objects compared to different sets of experimental conditions arising from separate experimental set-ups. | The simultaneous operation may produce a false image because of radioactive contamination. This radiation may influence/or cause change in the composition of object materials and could result in a false detection in the form of a noise. |

Presently, a thermal neutron beam and a poly-energetic X-ray spectrum, with corresponding matching detector technologies, have been utilized to build the NXCT system. The applied neutron and X-ray spectrum is suitable for current research and particularly for NDT applications. Nevertheless, a neutron generator and a different X-ray source with a high energy spectrum can be utilized to build another high energy

system for specific applications such as high volume cargo screening or similar research. In the current experimental scenario, a thermal neutron beam, originating from the MSTR core is used as the source. However, a neutron generator can also be employed for imaging applications. The lack of commercial availability of high resolution fast neutron imaging detectors is a constraint to such a system. For thermal neutron imaging, the neutron generator producing fast neutrons can be thermalized for MCP detectors. The modification can be applied by using borated polyethylene or another moderating medium and then by applying a fast neutron/gamma filter. The image formation is primarily based on the applied radiation sources and associated detector technologies.

During imaging operation, cross contamination of an object is also possible. For such cases, examining materials that depend on their cross section and linear attenuation coefficient for neutron and X-ray imaging, respectively, can be divided into a number of categories for the affinity of cross contamination and then could be examined in a certain pattern to avoid such contamination (i.e., X-ray imaging first and then neutron imaging). In the present scenario, the object could become radioactive due to cross contamination, but the surrounding medium would not because the optimized beam geometry (see Fig. 6.1) will not allow for any unwanted exposure of the surrounding medium. Presently, all imaging object activity is monitored through wall-mounted neutron/x-ray detectors and by hand-held counters. During imaging experiments, all activity monitoring was essential and was performed by authorized personal using hand-held counters.

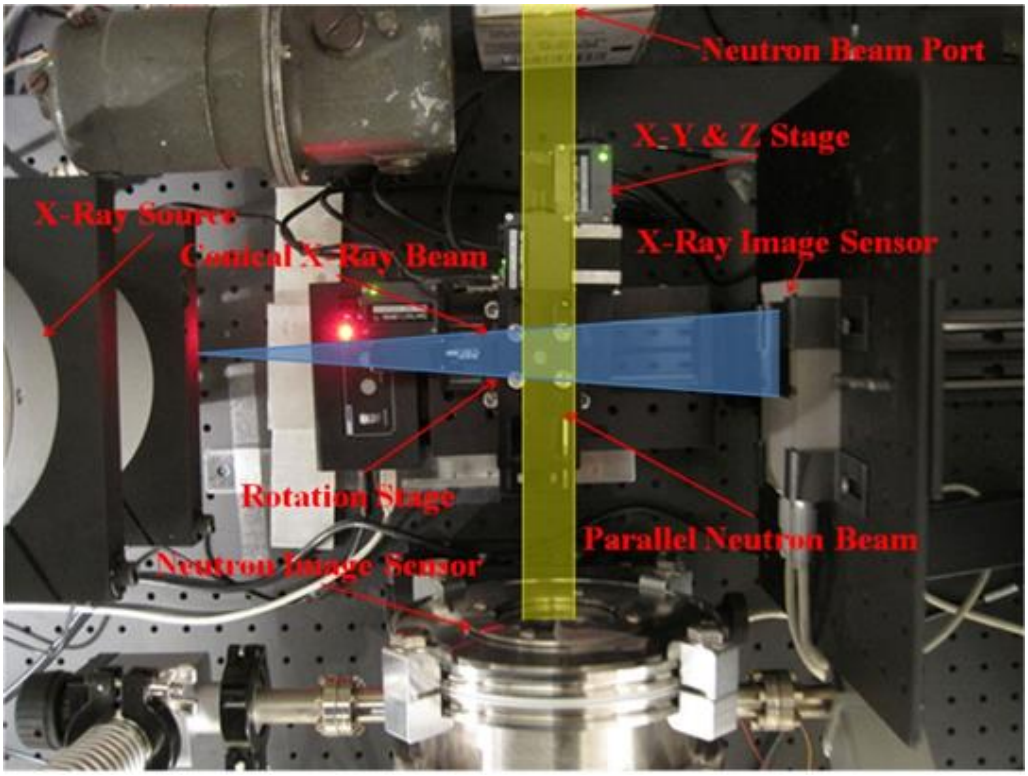


Figure 6.1. Top-View Photograph of the NXCT System Showing Orthogonal Arrangement of the Neutron and X-ray Imaging Module with a Sample Positioning System that Facilitates Object Rotation and Motion in X, Y or Z Direction for Corresponding Detectors

Due to careful optimization and calibration of the imaging system [18], the sample positioning device's travel distances in the X, Y, and Z directions does not obstruct the beam geometries, but the device also optimizes the field of view for both modalities (see Fig. 6.2).

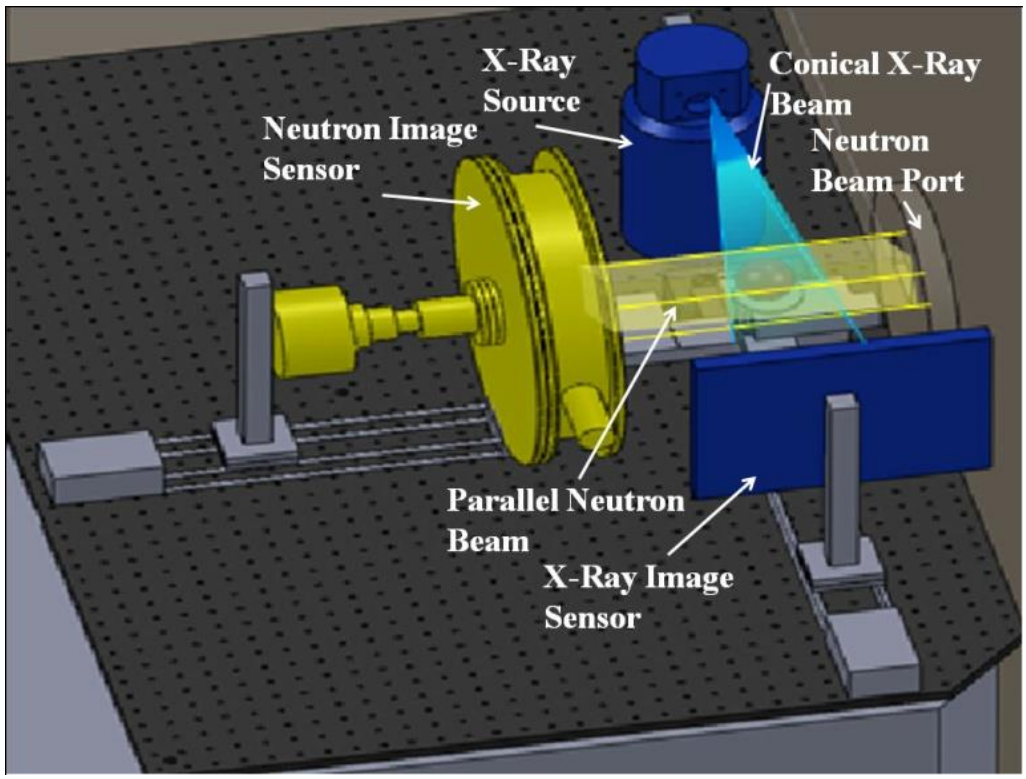


Figure 6.2. Illustration of a 3D Model for Beam Geometry Optimization of the NXCT System, Facilitating Simultaneous Imaging and Protecting the Neutron and X-ray Image Sensor from Unwanted Radiation

In the case of a highly radioactive target, the object can be manipulated through the sample positioning system and can be brought closer to the X-ray image sensor without exposing the image sensor in the center of the neutron beam (see Fig.6.2). This eventually eliminates the possibility of radiation damage to the X-ray image sensor from neutrons and facilitates the high resolution X-ray imaging by placing the object very close to the image sensor. To verify possible neutron exposure and to investigate the possibility of radiation damage to the X-ray detector, few gold foils were placed on the X-ray detector as well as on X-ray tube and neutron imaging experiments were performed at different timing intervals. Later, gold foils were counted on the high purity

germanium (HPGe) detector for neutron activation. The gold foils did not provide any counts on HPGe detector. Hence, it confirms that present beam geometries are well optimized and does not pose any neutron damage to the X-ray detector.

The performance evaluation of the NXCT system was performed in terms of image uniformity, linearity and spatial resolution. Additionally, the correlation between the applied beam intensity, the resulting image quality, and the system sensitivity was investigated. The combined neutron/X-ray digital imaging system was evaluated in terms of performance parameters. The MTF of the X-ray imaging module as well as for the neutron imaging module was calculated using the Edge method. In X-ray imaging module, the spatial frequency at 10% of the MTF was found to be 8 lp/mm, which is in agreement with the value of 8.5 lp/mm determined from the square wave response method. The MTF value between 8 and 8.5 lp/mm at 10% of spatial frequency suggests that spatial resolution of the X-ray imaging module is between 58.8 and 62.5 μm. The MTF value of 8 lp/mm at 10% of spatial frequency is in agreement with the published literature from manufacturer's specification document [70] and also with a similar measurement performed by Yagi et al. [71]. The detective quantum efficiency of the X-ray imaging module was found to be 0.53. The DQE of the X-ray module normally ranges between 0.1 – 0.7 [45-57]. Furthermore, the NPS spectrum for the neutron imaging module was also evaluated in a similar way as the X-ray imaging module. In order to improve the image quality of the neutron imaging module, a pin-hole mask phantom was used to correct the geometrical non-linearity of the delay line anode readout. The non-linearity correction of the delay line anode readout has been shown through the corrected images of perforated cadmium strip and electroformed phantom. In

neutron imaging module, the spatial frequency at 10% of the MTF was found at least to be 4.3 lp/mm. The MTF value of 4.3 lp/mm at 10% of spatial frequency suggests that spatial resolution of the neutron imaging module is 116.3 μm. The detective quantum efficiency of the neutron imaging module was found to be 2.5 x $10^{-4}$ which is in agreement with the value reported by Lewandowski et al. The MTF value is comparable to other research group measurements where MTF values lies between 85 -200 μm for high resolution neutron imaging [61-63, 72]. Certainly, as described in earlier sections physical and geometrical characteristics are deciding factor for such values.

The real-time neutron/X-ray imaging (radiography/tomography) applications with significant image clarity have been shown which confirms that system is well optimized in terms of beam diagnostics and executable operations. To date, there are no special techniques that have been employed to register these images. Therefore, reported images seem to shift or change between the modalities. However, an image registration technique can be employed in the near future. It is worth to mention that NXCT sample positioning system is numerically controlled with high degree of accuracy which can be utilized to position the images for corresponding detectors. This research presents significant contribution to science especially towards design, development and characterization of advanced radiation imaging system. The described design criterions and procedures can effectively be utilized to design and develop advanced combined computed tomography system. The construction and implementation of the NXCT imaging system at Missouri University of Science and Technology and the resulting imaging method is the first such method to be developed. This method will provide various benefits across multiple disciplines, particularly in non-destructive evaluation and nuclear engineering. It has been

shown that fusion of neutron and X-ray images provides greater image clarity and usefulness. This new method holds potential to become the industry standard in non-destructive evaluation and testing. The many uses of the NXCT system are still being determined and will allow for improved research in practically all engineering disciplines.

APPENDIX A.

NXCT Drawings, Schematics and Facility Layout.

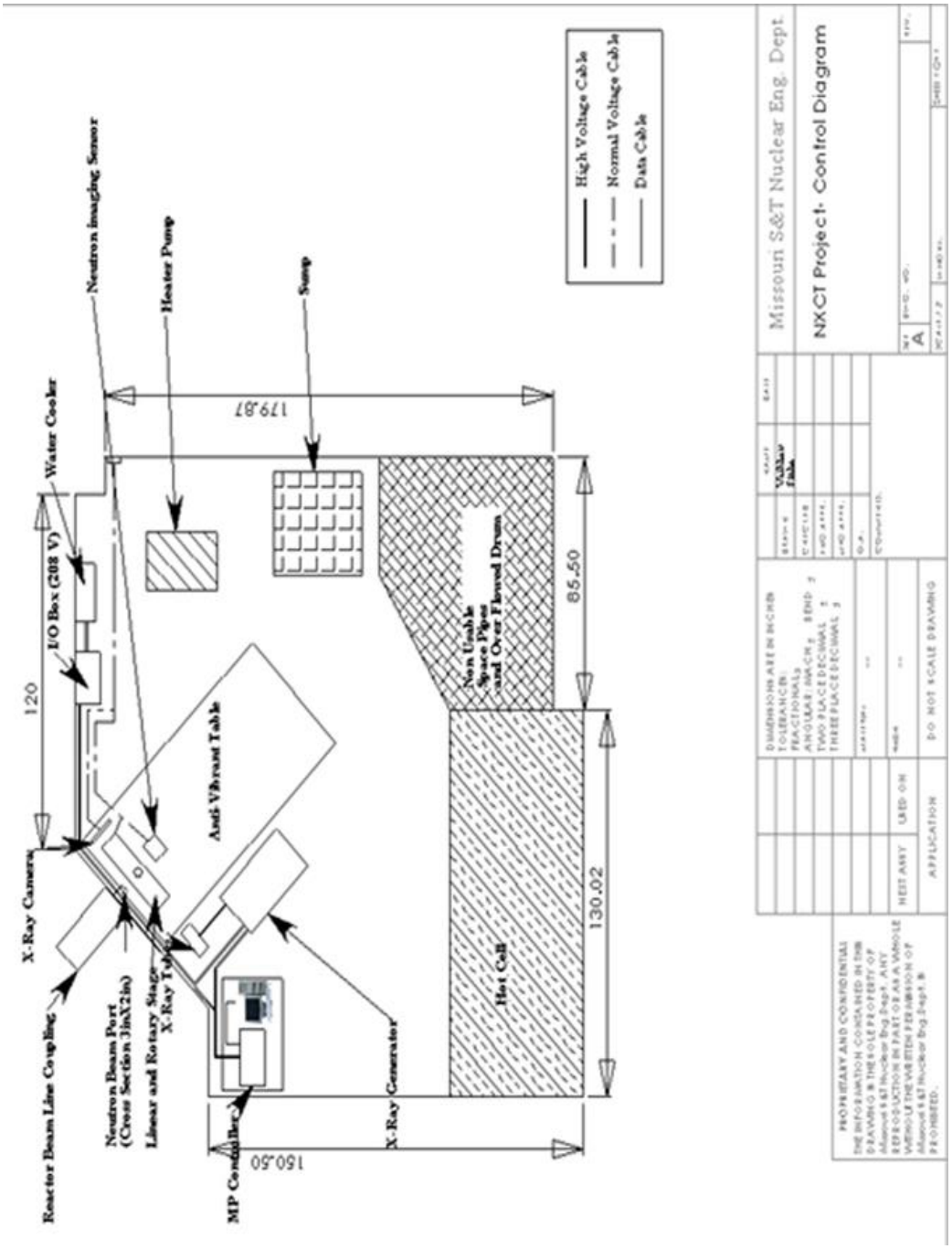


Figure A.1. NXCT Facility Layout at MSTR

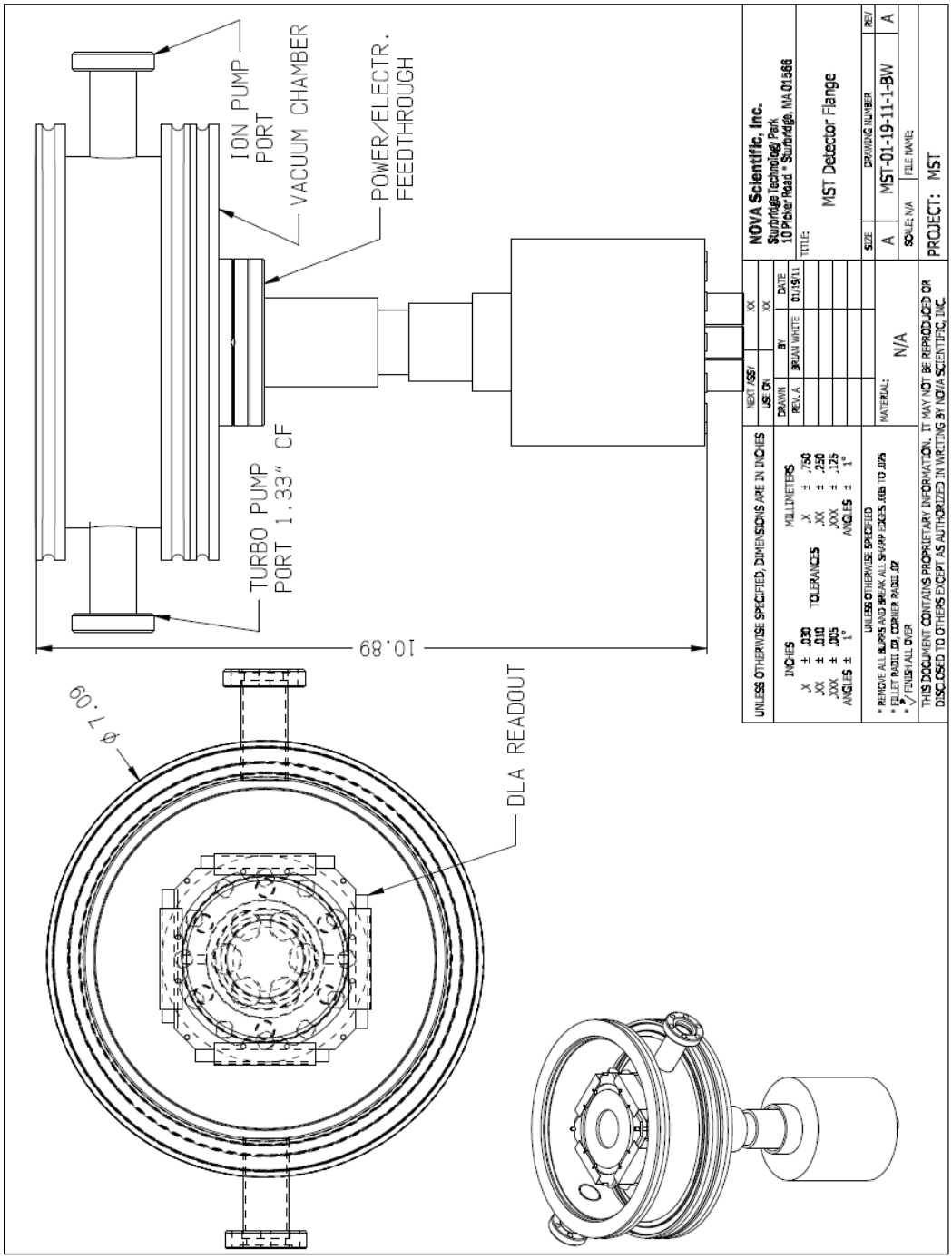


Figure A.2. Drawing of MCP Base Neutron Detector Flange

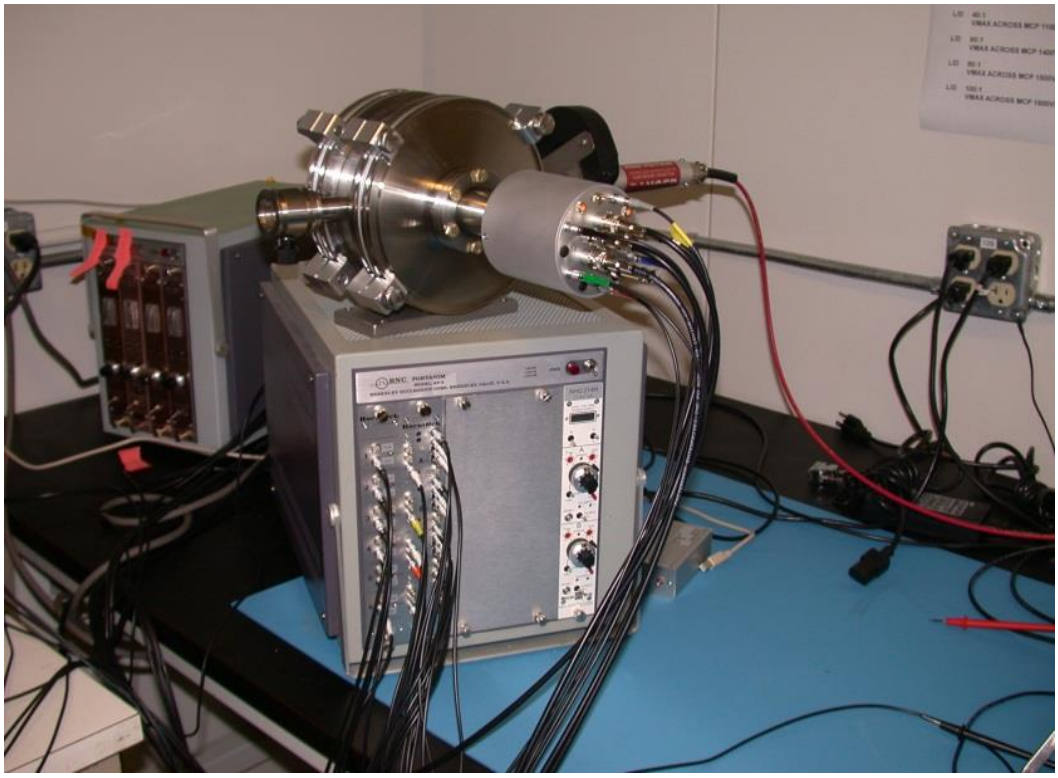

Figure A.3. Photograph of MCP Based Neutron Detector with CFD Electronics

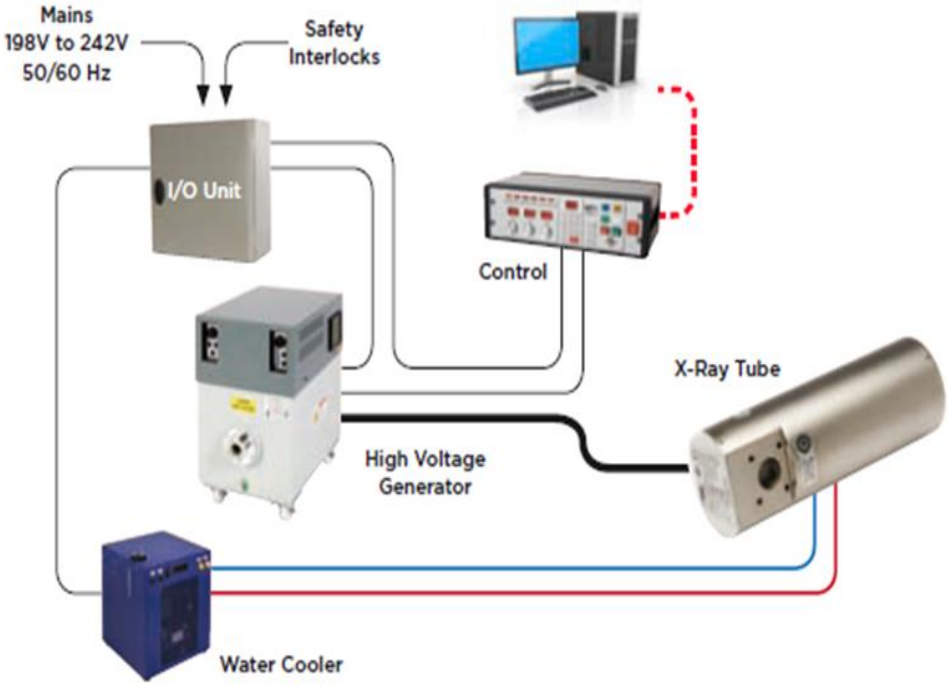


Figure A.4. Schematics of X-ray Generator System


Figure A.5. Radiation Safety Alarm and Direct Disconnect Switch

## BIBLIOGRAPHY

[1] Belgya T., Kis Z., Szentmiklósi Z., Kasztovszky Z., Kudejova P., Schulze R., Materna T., Festa G., Caroppi P.A., First elemental imaging experiments on a combined PGAI and NT setup at the Budapest Research Reactor,Journal of Radioanalytical and Nuclear Chemistry, July 2008,Doi: 10.1007/s10967-008-1605-7, pp. 751–754.

[2] Belgya T., Kis Z., Szentmiklósi L., Kasztovszky Z., Festa G., Andreanelli L., DePascale M.P., Pietropaolo A., Kudejova P., Schulze R., Materna T., A new PGAI-NT setup at the NIPS facility of the Budapest Research Reactor, Journal of Radioanalytical and Nuclear Chemistry, July 2008, Doi: 10.1007/s10967-008-1510-0, pp. 713–718.

[3] Szentmiklósi Z., Belgya T., Revay Z., Kis Z., Upgrade of the prompt gamma activation analysis and the neutron-induced prompt gamma spectroscopy facilities at the Budapest research reactor, Journal of Radioanalytical and Nuclear Chemistry, August 2010, Doi: 10.1007/s10967-010-0765-4, pp. 501-505.

[4] Strobl M., Manke I., Kardjilov N., Hilger A., Dawson M., Banhart J., Advances in neutron radiography and tomography, Journal of Physics D: Applied Physics, November 2009, Vol. 42, pp. 21.

[5] Wolbrast A. B., Physics of Radiology, Medical Physics Publishing Corporation, 2005.

[6] Triolo R., Giambona G., Celso F.L., Ruffo I., Kardjilov N., Hilger A., Manke I., Paulke A., Combined Application of X-Ray and Neutron Imaging Techniques to Wood Materials, Conservation Science in Cultural Heritage, 2010, DOI: 10.6092/issn.1973-9494/2322, pp. 143-158.

[7] Yasuda R., Matsubayashi M., Nakata M., Harada K., Amano H., Sasajima F., Nishi M., Horiguchi Y., Application of neutron imaging plate and neutron CT methods on nuclear fuels and materials , Nuclear Science, IEEE Transactions on, February 2005, Vol 52, pp. 313-316.

[8] Balasko M., Kuba A., Nagy A., Kiss Z., Rodek L., Ruskó L., Neutron-, gamma- and X-ray three-dimensional computer tomography at the Budapest research reactor, Nuclear Instruments and Methods in Physics Research A, 542,2005, pp. 22-27.

[9] Anderson I. S., McGreevy R. L., Bilheux H. Z., Neutron Imaging and Applications. Springer Science Business Media, LLC, 987-0-387-78692-6, 2009.

[10] http://www.science.org.au/nova/086/086key.htm. Nova Science in the News Australian Academy of Science, Acton, July 2007 (Accessed September 2011).

[11] Tsoulfanidis N., Measurement and Detection of Radiation, Taylor and Francis Group, Boca Raton, FL, U.S., 1995, pp. 153-175.

[12] Knoll G. F., Radiation Detection and Measurement, 2nd Edition, Wiley Publishers, 0-471-81504-7, 1989, pp. 50-54.

[13] Shultis K. J.,Faw R. E., Radiation Shielding. American Nuclear Society, Illinois, 2000.

[14] https://mospace.umsystem.edu/xmlui/handle/10355/29475, Strantz F., Lee H.K., Density Determination of Tristructural-Isotropic Nuclear Fuel using Multiple Projection X-ray Radiography, Missouri University of Science and Technology, Rolla, 2011 (Accessed September 2012).

[15] Lamarsh J., Baratta A., Introduction to Nuclear Engineering, 3rd Edition. Prentice Hall, New Jersey, 2001.

[16] http://scholarsmine.mst.edu, Characterization of the Neutron Flux Energy Spectrum at the Missouri University of Science and Technology Research Reactor (MSTR) Missouri University of Science & Technology, Rolla, 2010 (Accessed 13 August 2010).

[17] Sinha V., Avachat A.V., Lee H. K., Design and Development of a Neutron/X-Ray Combined Computed Tomography System at Missouri S&T, Journal of Radioanalytical and Nuclear Chemistry, August 2012, Doi: 10.1007/s10967-012-2062-x, pp. 799-806.

[18] Sinha V., Srivastava A., Lee H. K., Liu X., Performance Evaluation of a Combined Neutron and X-ray Digital Imaging System, Proc. SPIE 8694, Nondestructive Characterization for Composite Materials, Aerospace Engineering, Civil Infrastructure, and Homeland Security, April 2013, doi:10.1117/12.2009931.

[19] Sinha V., Srivastava A., Lee H. K., Liu X., Feasibility studies on explosive detection and homeland security applications using a neutron and x-ray combined computed tomography system, Proc. SPIE 8710, Chemical, Biological, Radiological, Nuclear, and Explosives (CBRNE) Sensing XIV, May 2013, doi:10.1117/12.2017988.

[20] Cutforth D.C., Neutron Sources for Radiography and Gaging, Practical Applications of Neutron Radiography and Gaging, American Society for Testing and Materials, STP 586, 1976, pp. 20-34

[21] Kobayashi H., Beam Formation and Characterization for Neutron Radiography, Nondestructive Testing and Evaluation, April 2007, Vol. 16, pp. 121-129.

[22] Mildner D. F. R., Arif M., Stone C. A., Crawford R. K., Neutron Transmission of Single- Crystal Sapphire Filters, Journal of Applied Crystallography, June 1993, Vol. 26, pp. 438-447.

[23] Stamatelatos I. E., Sapphire Filter Thickness Optimization in Neutron Scattering Instruments, Review of Scientific Instruments, Vol 71, January 2000, pp. 70-73.

[24] Barton J. P., Filters for Thermal Neutron Radiography, Nondestructive Testing and Evaluation, Vol. 16, June 2000, pp. 95-110.

[25] http://enterprise2.astm.org/DOWNLOAD/E748.143144-1.pdf, Standard Practices for Thermal Neutron Radiography of Materials, ASTM International, 2008 (Accessed 10 December 2011).

[26] http://enterprise2.astm.org/DOWNLOAD/E2023.143144-1.pdf, Standard Practice for Fabrication of Neutron Radiographic Sensitivity Indicators, ASTM International, 2010 (Accessed 10 December 2011).

[27] http://enterprise2.astm.org/DOWNLOAD/E545.143144-1.pdf, Standard Test Method for Determining Image Quality in Direct Thermal Neutron Radiographic Examination, ASTM International, 2010 (Accessed 10 February 2012).

[28] http://enterprise1.astm.org/DOWNLOAD/E803.143144-1.pdf, Standard Test Method for Determining the L/D Ratio of Neutron Radiography Beams, ASTM International, 2008 (Accessed10 January 2012).

[29] Dove E.L, Notes on Computerized Tomography, Physics of Medical Imaging.

[30] http://www.mathworks.com/products/matlab/, Matlab, MathWorks, 2010 (Accessed June 2011).

[31] Vontobel P., Lehmann E., Carlson W.D., Comparison of X-ray and neutron tomography investigations of geological materials, IEEE Transactions on Nuclear Science, February 2005, Vol. 52, pp. 338-341.

[32] http://www.woodculther.com/wp-content/uploads/2010/10/COST-IE0601-2010-Izmir_Mannes.pdf, Neutron vs. X-ray computed tomography: comparative study on the example of a violin Interaction between Wood Science and Conservation of Cultural Heritage, Turkey, 2010. (Accessed 7 December 2011).

[33] Poludniowski G., Landry G., DeBlois F., Evans P.M., Verhaegen F., SpekCalc: a program to calculate photon spectra from tungsten anode x-ray tubes,Physics in Medicine and Biology, October 2009, Vol. 54, Doi:10.1088/0031-9155/54/19/N01, pp. N433-N438.

[34] Tremsin A.S., Feller W.B., Downing R.G., Efficiency optimization of microchannel plate (MCP) neutron imaging detectors. I. Square channels with 10B doping, Nuclear Instruments and Methods in Physics Research A, 539, pp. 278-311.

[35] http://rtc.jbtp.or.kr/RITHome/Sub02_01_02, Flat Panel Detector, Radiation Imaging Technology Center, JBTB, Korea, 2002 (Accessed 12 January 2011).

[36] http://physics.nist.gov/PhysRefData/XrayMassCoef/tab4.html, X-Ray Mass Attenuation Coefficients, National Institute of Standards and Technology, USA, 2012 (Accessed 12 January 2012).

[37] http://www.nndc.bnl.gov/exfor/exfor00.htm, Experimental Nuclear Reaction Data (EXFOR / CSISRS), Brookhaven National Lab, New York, 2011 (Accessed 14 Sept 2012).

[38] Casalta S., Daquino G. G., Metten L., Oudaertaand J., Van de Sandea A., Digital Image Analysis of X-ray and Neutron Radiography for the Inspection and the Monitoring of Nuclear Materials, NDT & E International, July 2003, Vol. 36(5), pp. 349-355.

[39] Dinca D., Schubert J. R., Callerame J., X-ray backscatter imaging, Proc. SPIE 6945, doi:10.1117/12.773334, April 2008.

[40] Glockmann W., Herwig T., X-ray scanner for detecting plastic articles, U.S. Patent 4 884 289, November 28, 1989.

[41] Cajipe V.B., Calderwood R.F., Clajus M., Hayakawa S., Jayaraman R., Tumer T.O., Grattan B., Yossifor O., Multi-energy x-ray imaging with linear CZT arrays and integrated electronics, IEEE RTSD conference record, Rome, 2004.

[42] Kotowski A.F., X-ray line scan system for use in baggage inspection, U.S. Patent 4 366 382, December 28, 1982.

[43] Tybinkowski A.P., Swain R., Cargo container tomography scanner system, U.S. Patent 7 062 011 B1, June 13, 2006.

[44] Kravis S.D., X-ray inspection system detecting explosives and other contraband, U.S. Patent 7 092 485 B2, August 15, 2006.

[45] Samei E., Flynn M. J., Reimann D. A., A method for measuring the presampled MTF of digital radiographic systems using an edge test device, Medical Physics, January 1998 , Vol. 25 (1), pp. 102-113.

[46] Judy P.F., The line spread function and modulation transfer function of a computed tomographic scanner, Medical Physics, 1976, Vol. 3(4), pp. 233-236.

[47] Fujita H., Tsai D.Y., Itoh T., Doi K., Morishita J., Ueda K., Ohtsuka A., A simple method for determining the modulation transfer function in digital radiography, IEEE Transactions on Medical Imaging, March 1992 , Vol. 11, pp. 34–39.

[48] Du L. Y., Umoh J., Nikolov H. N., Pollmann S. I., Lee T. Y., Holdsworth D. W., A quality assurance phantom for the performance evaluation of volumetric micro-CT systems , Physics in Medicine and Biology, December 2007, Vol. 52, pp. 7087-7108.

[49] Kawashita I., Maeda K., Arimura H., Morikawa K., Ishida T., Development of an automated method for evaluation of sharpness of digital radiographs using edge method, Proc. SPIE 4320, June 2001, pp. 331-338.

[50] Granfors P.R., Aufrichtig R., Performance of a 41X41-cm2 amorphous silicon flat panel x-ray detector for radiographic imaging applications, Medical Physics, June 2000, Vol. 27(6), pp. 1324-1331.

[51] Baker S. A., King N. S. P., Lewis W., Lutz S. S., Morgan D. V., Schaefer T., Wilke M. D., Performance of image intensifiers in radiographic systems, Proc. SPIE 3968, February 2000, pp. 39-46.

[52] Zhang D., Li X., Liu B., Objective characterization of GE Discovery CT750 HD scanner: Gemstone spectral imaging mode, Medical Physics, February 2011, Vol. 38, pp. 1178–1188.

[53] Rossmann K., Measurement of the modulation transfer function of radiographic systems containing fluorescent screens, Physics in Medicine and Biology, March 1964, Vol. 9, pp. 551–557.

[54] Hanson K. M., A simplified method of estimating noise power spectra, Proc. SPIE 3336, July 1998, pp. 243-250.

[55] Giger M.L., Doi K., Metz C.E., Investigation of basic imaging properties in digital radiography.2. Noise Wiener spectrum, Medical Physics, December 1984, Vol. 11, pp. 797–805.

[56] Dobbins J.T., Ergun D.L., Rutz L., Hinshaw D.A., Blume H., Clarke D.C., DQE (f) of four generations of computed radiography acquisition devices, Medical Physics, October 1995, Vol. 22, pp. 1581–1593.

[57] Boedeker K.L., McNitt-Gray M.F., Application of the noise power spectrum in modern diagnostic MDCT: part II. Noise power spectra and signal to noise, Physics in Medicine and Biology, July 2007, Vol. 52, pp. 4047-4061.

[58] http://www.oegfzp.at/fileadmin/papers/148_Sikakana.pdf, Sikakana I., 18th World Conference on Nondestructive Testing, Nondestructive Testing, 16 April 2012 (Accessed 07 December 2012).

[59] Tremsin A. S., McPhate J. B., Vallerga J. V., Siegmund O. H. W., Feller W. B., Lehmann E., Detection efficiency, spatial and timing resolution of thermal and cold neutron counting MCP detectors, Nuclear Instruments and Methods in Physics Research A, 604, June 2009, pp. 140–143.

[60] Shestakova I.V., Tipnis S.V., Gaysinskiy V. B., Antal J. J., Bobek L., Nagarkar V. V., A New Sensor for Thermal Neutron Imaging, IEEE Transactions on Nuclear Science, August 2005. Vol. 52, pp. 1109 - 1113.

[61] Vallerga J., McPhate J., Tremsin A., Siegmund O., High-resolution UV, alpha and neutron imaging with the Timepix CMOS readout, Nuclear Instruments and Methods in Physics Research A, 591, 2008, pp. 151–154.

[62] Lewandowski R., Cao L., Turkoglu D., Noise evaluation of a digital neutron imaging device, Nuclear Instruments and Methods in Physics Research A, 674, May 2012, pp. 46–50.

[63] Turkoglu D., Cao L., Lewandowski R., A low-cost neutron radiography device, Physics Procedia, 2013, Vol. 43, pp. 54-65.

[64] Padgett R., Kotre C. J., Development and application of programs to measure modulation transfer function, noise power spectrum and detective quantum efficiency, Radiation Protection Dosimetry, February 2005 , Vol. 117(1-3), pp. 283-287.

[65] http://www.princeton.edu/~aglaser/lecture2007_detection.pdf, Glaser A., Detection of Special Nuclear Materials, Princeton University, 16 April 2007 (Accessed 31 January 2013).

[66] Slaughter D. R., Accatino M. R., Bernstein A., Church J. A., Descalle M. A.,Gosnell T. B., Hall J. M., Loshak A., Manatt D. R., Mauger G. J., Moore T. L.,Norman E. B., Pohl B. A., Pruet J. A., Petersen D. C., Walling R. S., Weirup D. L.,Prussin S. G., McDowell M., Preliminary results utilizing high-energy fission product γ-rays to detect fissionable material in cargo, Nuclear Instruments and Methods in Physics Research B, 241, December 2005, pp. 777-781.

[67] Cutmore N. G., Liu Y., Tickner J. R., Development and commercialization of a fast-neutron/x-ray Cargo Scanner, IEEE RTSD conference record, November 2010, pp. 330 – 336.

[68] Pajares G., Cruz J. M., A wavelet-based image fusion tutorial, Pattern Recognition, September 2004 , Vol. 37, pp. 1855-1872.

[69] Chan C., Kim J., Feng D., Cai W., Interactive fusion and contrast enhancement for whole body PET/CT data using multi-image pixel composting, IEEE Nuclear Science Symposium Conference Record 0-7803-9921-3/05, October 2005, pp. 2618 - 2621.

[70] www.teledynedalsa.com/public/ls/datasheets/ShadoBox1024.pdf, Shad-o-Box 1024 X-Ray Camera, Rad-icon Imaging Corporation, 16 April 2007 (Accessed 31 January 2011).

[71] Yagi N., Yamamoto M., Uesugi K., Inoue K., CMOS Imaging Detectors as X-ray Detectors for Synchrotron Radiation Experiments, AIP Conference Proceedings, 705, 2003, pp. 885-888.

[72] Hussey D. S., Jacobson D. L., Arif M., Huffman P. R., Williams R. E., Cook J.C., N ew Neutron Imaging Facility at the NIST, Nuclear Instruments and Methods in Physics Research Section A, Vol. 542, June 2000, pp. 9-15.

# VITA

Vaibhav Sinha was born in Lucknow, India. In the year 2002, he received his Bachelor of Engineering degree in Mechanical Engineering with Honors from Dr. B.R Ambedkar University, Agra, India. He gained corporate experience as a Graduate Engineer Trainee at Government of India Enterprises, Panki Thermal Power Station and Hindustan Aeronautics Limited. He graduated with a Master of Science degree in Nuclear Applications from Aachen University of Applied Sciences, Aachen, Germany in the year 2006. He performed his research work with Department of Safety and Radiation Protection at Research Center Juelich, Germany for Design and Construction of Children Calibration Phantoms for Whole Body Counters. He has also performed research at Idaho Accelerator Center for radioisotope production of Copper-67 using a Linear Electron Accelerator. He will receive his PhD degree in Nuclear Engineering from Missouri University of Science and Technology in December 2013. His dissertation establishes a novel neutron/X-ray combined computed tomography system for advanced nondestructive evaluation research. While working on his PhD, he has also contributed to different research projects at Missouri University of Science and Technology in the areas of installation and shielding design of neutron generator facility, infrastructure upgrade of radiation measurements and spectroscopy laboratory. He has also worked as a Teaching Assistant for nuclear engineering courses in Applied Health Physics, Reactor Physics and Radiation Measurement & Spectroscopy Laboratory at Missouri University of Science & Technology. His research resulted in 3 peer-reviewed publications, and also received two awards from Council of Ionizing Radiation Measurement and Standards.